Skolkovo Institute of Science and Technology

LOCATION AND SOURCE MECHANISMS OF INDUCED MICROSEISMIC EVENTS: A DEEP LEARNING APPROACH

Doctoral Thesis
by

DANIEL STEPHEN WAMRIEW

DOCTORAL PROGRAM IN PETROLEUM ENGINEERING

Supervisor
Professor, Dmitry Koroteev

Co-supervisor
Professor, Roman Pevzner

Moscow – 2022

© DANIEL STEPHEN WAMRIEW, 2022

I hereby declare that the work presented in this thesis was carried out by myself at Skolkovo Institute of Science and Technology, Moscow, except where due acknowledgement is made, and has not been submitted for any other degree.

Daniel Stephen Wamriew

Prof. Dmitry Koroteev

Abstract

Microseismic monitoring provides extensive and vital information about the subsurface formation, including rock properties, fracture sizes and networks, and fluid propagation. The technology has a wide range of applications in the oil and gas industry, including hydraulic fracture monitoring, water injection, reservoir characterization, casing integrity and carbon dioxide (CO_2) and hydrogen (H_2) storage, but it can also be utilised in other fields such as mining and geothermal resource development. The spatial distributions of the hypocenters of microseismic events allow for the estimation of the stimulated reservoir volume, whereas the source mechanisms allow for the understanding of fracture size, networks, and orientations. During microseismic monitoring, large volumes of data are recorded due to the often large number of sensors deployed, making it difficult to process and interpret the data in real-time or semi-real-time using conventional routines.

This thesis proposes cutting-edge technologies for the acquisition, processing, and interpretation of microseismic data. In addition to 3-C geophones, fiber optic distributed acoustic sensing (DAS) is used for downhole data acquisition, while Deep Learning (DL) is used for processing and interpretation of recorded microseismic data. The results show that deep neural networks are capable of learning the properties of seismic waveforms and can detect and locate microseismic events as well as invert for the velocity model and source mechanisms from microseismic data. All the procedures can be carried out simultaneously and in real-time. The integration of DL to the data acquisition process will fast-track the field decision-making process, enabling optimisation of reservoir operations and production.

Fiber optic cables are inexpensive, resistant to high pressure, durable, and can be used in any well, regardless of its geometry. DAS provides high-resolution imaging of the subsurface both in space and time. Deep learning offers a streamlined workflow for processing and interpreting microseismic data and provides accurate detection and inversion results in real-time. It is computationally efficient and takes advantage of the massive amounts of data that stream in from DAS equipment.

Publications

Parts of this thesis have been published in the following journals and conference proceedings:

Articles

1. Daniel Wamriew, Desmond Batsa Dorhjie, Daniil Bogoedov, Roman Pevzner, Evgenii Maltsev, Marwan Charara, Dimitri Pissarenko, and Dmitry Koroteev. Microseismic monitoring and analysis using cutting-edge technology: A key enabler for reservoir characterization. *Remote Sensing*, 14(14):3417, July 2022b. doi:10.3390/rs14143417. URL `https://doi.org/10.3390/2Frs14143417`

2. Daniel Wamriew, Marwan Charara, and Dimitri Pissarenko. Joint event location and velocity model update in real-time for downhole microseismic monitoring: A deep learning approach. *Computers & Geosciences*, 158:104965, January 2022a. doi:10.1016/j.cageo.2021.104965. URL `https://doi.org/10.1016/j.cageo.2021.104965`

3. Daniel Wamriew, Roman Pevzner, Evgenii Maltsev, and Dimitri Pissarenko. Deep neural networks for detection and location of microseismic events and velocity model inversion from microseismic data acquired by distributed acoustic sensing array. *Sensors*, 21(19):6627, October 2021b. doi:10.3390/s21196627. URL `https://doi.org/10.3390/s21196627`

Conferences

1. Daniel Wamriew, Evgenii Maltsev, Roman Pevzner, and Dimitri Pissarenko. Deep neural networks for inversion of borehole microseismic data recorded by DAS. In *Sixth EAGE Borehole Geophysics Workshop*. European Association of Geoscientists & Engineers, 2021a. doi:10.3997/2214-4609.2021613016. URL `https://doi.org/10.3997/2214-4609.2021613016`

2. Daniel Wamriew, Marwan Charara, and Evgenii Maltsev. Deep neural network for real-time location and moment tensor inversion of borehole micro-

seismic events induced by hydraulic fracturing. In *Day 3 Wed, October 28, 2020*. SPE, October 2020. doi:10.2118/201925-ms. URL https://doi.org/10.2118/201925-ms

To Polina and Leo,
my rib and my flesh!

Acknowledgments

During my undergraduate years, my friends and I would always remind each other: *"Degree ni Harambee"*. Loosely put - an academic degree is all about cooperation. I couldn't agree more, and this thesis is the result of many huge such *Harambees!*

I would like to thank my team of scientific advisors who provided me with a conducive research environment and without whom this work would have not been possible:

Prof. Roman Pevzner who despite the 7 hours time difference between Moscow and Perth, always created time for me, provided counsel and shared with me his invaluable expertise.

Dr. Marwan Charara, for giving me the opportunity to join Skoltech and challenging me to take up research in microseismics. It is at Skoltech that I met the most brilliant brains I've ever interacted with. His humor, inspirational and motivational talks during our team meetings brought a good balance between *normal life* and *PhD life*.

Prof. Dimitri Pissarenko, for very insightful discussions on my research topic, and encouraging me to try out new ideas and pointing me to emerging fields.

Prof. Dmitry Koroteev who has been very kind and supportive, and was always available whenever I needed help. Thank you!

I would also like to express my gratitude to Prof. Sergey Stanchits, a member of my individual doctoral committee, for his advice and support all the four years of my research. Natalia Kiani for super coordination with Education Office; always making sure we had the right information as far as Skoltech policy is concerned. Dmitry Voloskov, who provided me with some of the out-of-the-box ideas. Dr. Evgenii Maltsev, who was always available whenever I needed help, even at weird times to call someone like midnight! But he still picked my calls and made sure my connection to the GPU was intact. Dr. Oleg Rogozin, whose brilliance with computers is at a different level, but most of all, whose enthusiasm in helping is so infectious.

I would like to thank my family for supporting me in thoughts, words and deeds. To Polina, for her kind words of encouragement, for believing in me and for bearing with my absence when I had to work long hours to beat deadlines. Her patience is over the moon. To Leo, for being a constant well of inspiration. To my parents, brothers and sisters, for standing with me all these years.

And finally, I thank the Almighty God for this far He's led me. His love endures forever!

Contents

List of Figures

List of Tables

"the secret of getting ahead is getting started."

Mark Twain

Chapter 1

Introduction

Human activities have in the past decades contributed to natural disasters such as earthquakes, floods, and wildfires [Fengqing et al., 2005, Diaz, 2007, Lim et al., 2014]. In the oil and gas industry, the drive to exploit fossil fuel deep within the earth's crust through the injection of agents to increase oil recovery has been reported to have contributed significantly to induced seismicity[Afra and Tarrahi, 2016]. The exploitation of the subsurface was intensified during the shale boom. This boom is characterized by the drilling of horizontal wells and hydraulic fracturing [Molenaar et al., 2012]. Recent calls for a global energy transition from fossil fuels to less CO_2 emitting sources have also led to even more subsurface activities such as geological hydrogen and methane storage and CO_2 sequestration and hence even more risks of induced seismicity due to the so-called energy transition. With the idea that similar activities in the past have led to the triggering of seismic events, there are fears of the long term effects of all these subsurface activities [Foulger et al., 2018]. Similarly, with advancements in technology, surface activities such as mega constructions and industrialization have increased significantly. These developments cause continuous changes, and interference with the geological structures which could lead to microseismic events, including earthquakes, when not detected early.

Induced seismicity, therefore, as the name suggests, is caused by human activities such as hydrocarbon exploitation, geothermal energy production, mining, and reservoir impoundment that result in the release of low-magnitude seismic energy (microseismic) due to changes in the stress distribution of the subsurface as a result of these operations. Figure 1-1 illustrates a schematic representation of primary sources of induced seismicity.

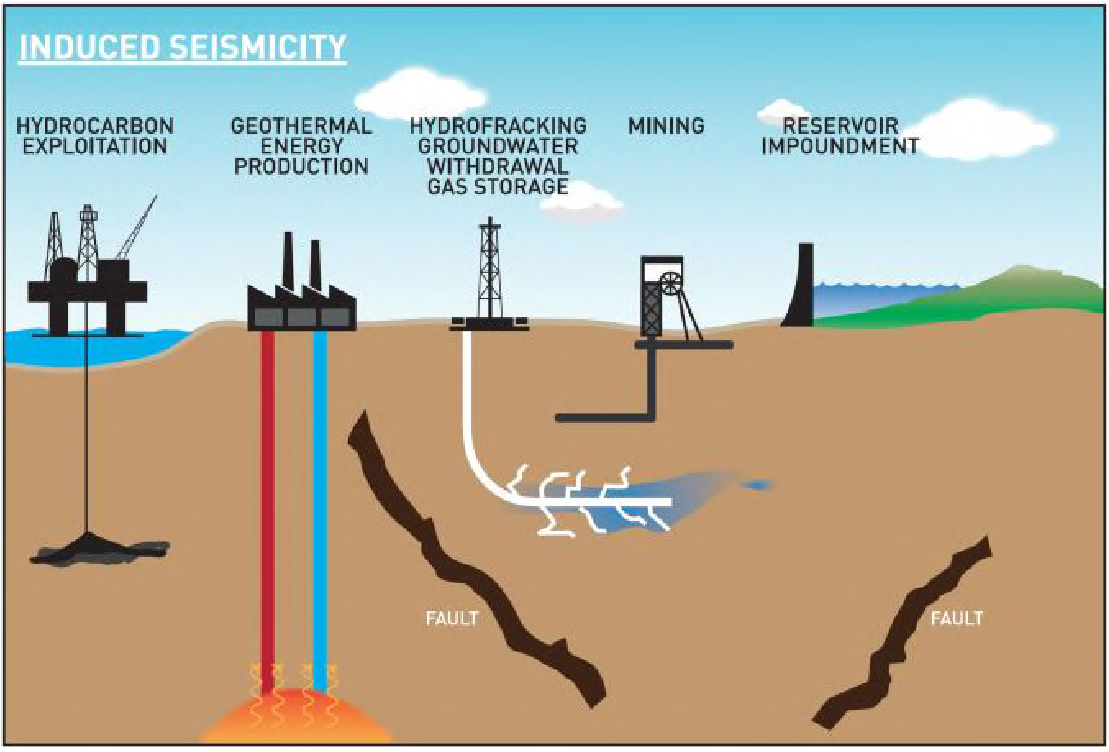

Figure 1-1: Primary causes of induced seismicity. Hydrocarbon exploitation involves oil and/or gas extraction and re-injection of wastewater back into the formation; geothermal energy production involves extraction of steam and re-injection of cold water back into the formation; hydrofracking involves high-pressure injection of water, proppant and sand into the formation with the aim of opening and widening existing fractures. Mining involves excavation of large volumes of rocks at depth and the resulting stress redistribution can cause fracture initiation, propagation, and rock mass movement along pre-existing fracture planes. Reservoir impoundment increases stress on the rock mass which may trigger induced events. Source:[Braun et al., 2018]

Unlike global earthquakes, which are felt hundreds of kilometres away from the hypocenter, microseismic events are not felt by humans and are difficult to detect and locate due to their low moment magnitudes. Yet, their detection and location may provide useful information about how the formation is fractured, as well as warning signs of impending catastrophe. Detection, location, and source characterization of microseismic events are thus still highly relevant and intriguing areas of research.

Although microseismic monitoring is a relatively new technology, its utility in reservoir characterization has been extensively established and validated by several studies. It is an established fact that accurate detection and location of microseismic events is necessary for the tracking of active faults and fracture propagation within the reservoir. The source mechanisms of the microseismic events provide invaluable information regarding the lengths, heights, growth, complexity, and orientation of the fractures. This information is essential for the understanding of how the fractures are connected and is necessary for characterization of the reservoir and the optimization of reservoir operations.

The rapid advancement of microseismic technology necessitates the creation of cutting-edge technology for the monitoring of microseismic events and the processing of the acquired microseismic data. This thesis develops novel tools and workflows, based on deep learning, for processing microseismic data acquired by conventional geophones or fiber-optic distributed acoustic sensors. The developed tools can be integrated with the field monitoring equipment for the real-time detection, location, and inversion of the source mechanisms of microseismic events as well as velocity model update. The novelty in the approach is that, for the first time, to the best of my knowledge, the four tasks of detection and location of microseismic events, velocity model update and inversion of source mechanisms of the microseismic events can be carried out simultaneously and in real-time. This will expedite field decision-making processes for the optimization of reservoir operations.

1.1 Aim

The main aim of this thesis is to develop algorithms and workflows for analysis of passive seismic data for induced seismicity using deep learning approaches. This will in turn reduce the costs of reservoir monitoring as well as help in optimization of reservoir stimulation process. The use of deep learning will facilitate the automation of reservoir monitoring and make it possible to perform joint inversions of microseismic events locations, velocity model update and estimation of focal mechanisms in real-/semi-real-time. In addition, the algorithms developed in this study can be applied, with great benefit, to other areas such as carbon dioxide sequestration. And to the scientific community, this work develops the knowledge of the application of

DAS and deep learning for the detection, location and source characterization of induced seismic events.

1.2 Objectives

The specific tasks carried out in order to fulfill the broad aim of this thesis include:

1. Generation of synthetic microseismic datasets for training and validating deep learning algorithms. This was achieved through seismic forward modelling using dynamic ray-tracing.

2. Development of data analysis algorithms for microseismic events detection, location and inversion for source parameter and velocity model based on deep learning.

3. Design, train and test deep neural network models using field and synthetic data.

4. Apply the trained deep neural network models to detect and locate hypocenters of the microseismic events in real-time.

5. Apply the trained deep neural network models to update the velocity model in real-time.

6. Perform full moment tensor inversion of the events using the trained deep neural networks in order to determine the source mechanisms of the located microseismic events.

1.3 Thesis Structure

Chapter 1 introduces the motivation of this thesis and defines the aim and objectives of this thesis.

Chapter 2 looks at the various related studies that have been conducted by other researchers in the field of microseismic monitoring. We draw attention to two revolutionary technologies that are changing the landscape of microseismic monitoring: Fiber-optic Distributed Acoustic Sensing and deep learning.

Chapter 3 presents theory behind microseismic monitoring with regards to detection, location and source mechanisms estimation. Basic theoretical descriptions of distributed acoustic sensing (DAS) and deep learning approaches are also given.

Chapter 4 presents comprehensive description of the design and implementation of the deep learning approach to processing microseismic data. Neural network architectures for different approaches are provided. Results for both synthetic and field studies are presented, analysed and discussed.

Chapter 5 summarises the findings of this thesis and draws conclusions.

"if I have seen further it is by standing on the shoulders of Giants."

Isaac Newton, 1675

Chapter 2

Background

2.1 Induced Seismic Events

In general, spatial and temporal earthquakes are modulated by natural activities such as the changes in tectonic stress, the movement of fluids in the subsurface, the rise and fall of tides, and pressure and temperature changes in atmospheric conditions. Based on observation of other terrestrial bodies, these events could lead to natural occurrences such as quakes without the interference of human activities [Garcia et al., 2005]. Regardless, several surveys are pointing to the fact that the rise in human activities through industrialization has contributed directly to the occurrences of induced seismic events [Gupta, 2002, Klose, 2012, Lippmann-Pipke et al., 2011, Emanov et al., 2014]. Seismic events believed to be induced by human activities are mainly in construction, mining, hydrocarbon extraction, hydraulic fracturing, and wastewater injection. Currently, concerns are growing about possible induced seismic events from CO_2 sequestration in geological formations. Foulger et al. [2018] presented a comprehensive review and database on earthquakes which were reported to have been induced by human activities. These activities were classified into Surface operations, subsurface extractions, subsurface injections and explosions.Figure 2-1 presents a summary by Foulger et al. [2018] on the occurrences of induced seismic activities across different sectors.

The study also gives a comparison of the maximum magnitude of the induced seismic events to the different suspected human inducing activities (Figure 2-2.

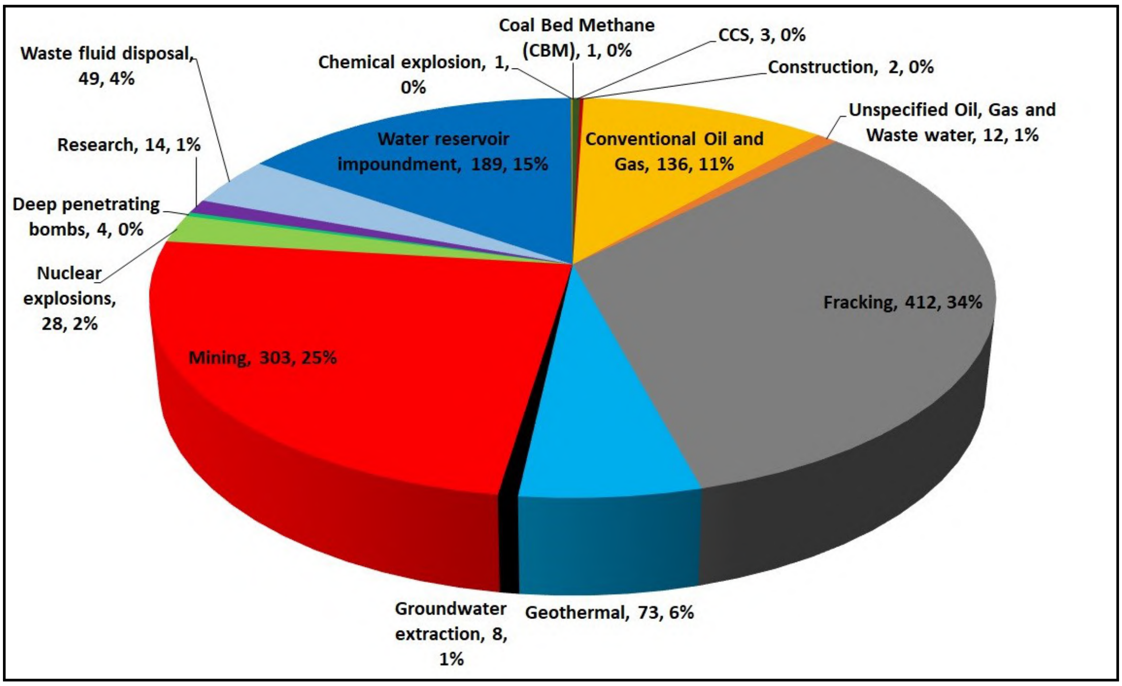

Figure 2-1: Courses of Induced seismicity by proportion. Hydraulic fracturing and mining are cited to have contributed to the most induced seismic events at 34% and 25% respectively. Source: [Foulger et al., 2018]

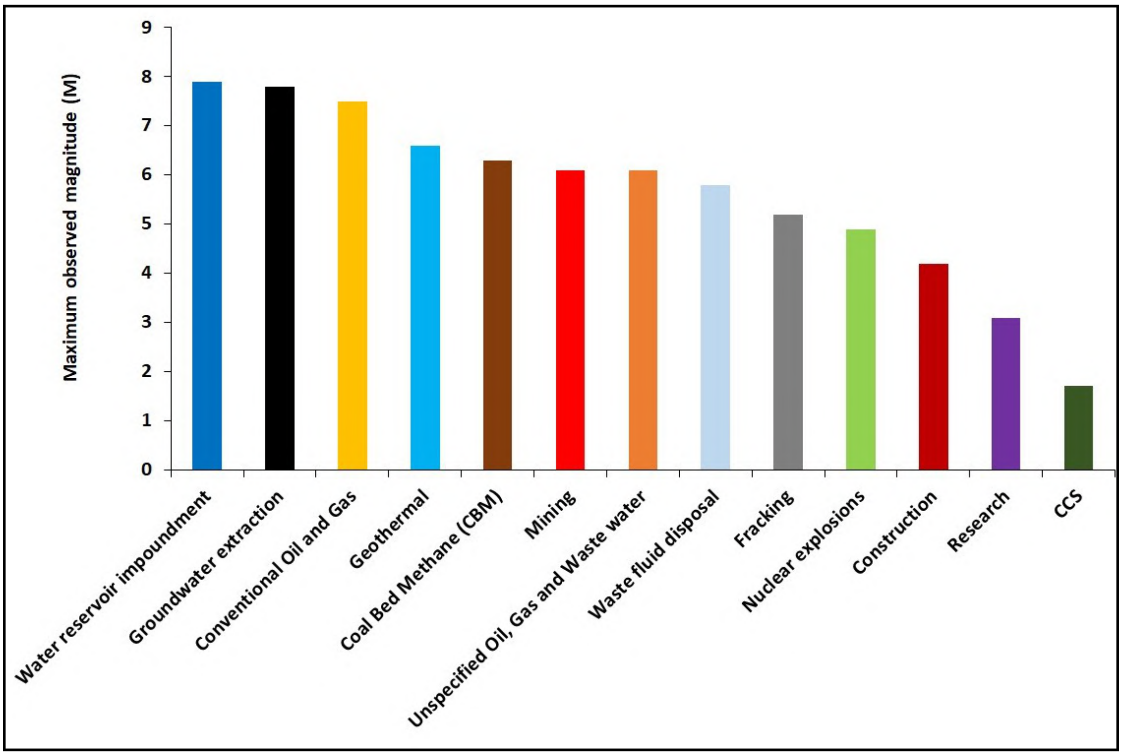

Figure 2-2: Maximum observed magnitudes of induced seismicity by different anthropogenic sources. Source: [Foulger et al., 2018]

Perhaps the most difficult parameter to quantify is the relationship between injected fluid volumes and the magnitude of the corresponding induced seismic events. A widely accepted relation is provided by McGarr [2014] in which he proposed a positive linear relationship between the two quantities, and provided a theoretical upper-bound limit for predicting the magnitude of induced seismicity with respect to injected fluid volume. Although, widely accepted, this theoretical relation does not apply to all cases as there are some exceptions. Figure 2-3 shows the relationship between between the magnitude of observed induced seismicity and the volume of injected fluids.

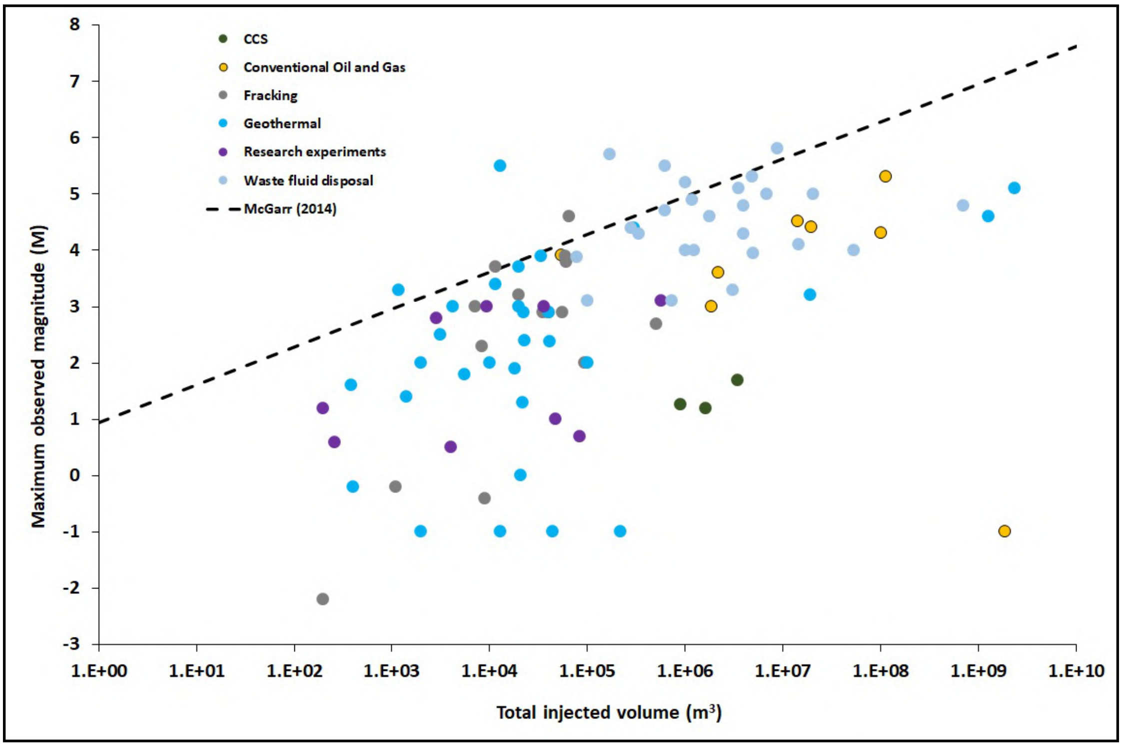

Figure 2-3: Maximum observed magnitudes versus total volume of injected fluids for sixty-nine induced seismic events. The dotted line indicates the upper-limit of the magnitudes based on theoretical consideration by McGarr [2014]. This theoretical consideration holds for many cases, although there are certain outliers which it does not account for. Source: [Foulger et al., 2018]

The characteristics of the most frequent induced seismic activities are related to fluid and geological interactions. On the other hand, one could argue that the counts of such activities as water dams and oil and gas have been taking place for a long time compared to CCS and hydraulic fracturing. The frequency of the occurrences of such activities highlights the importance of continuous monitoring of microseismic and seismic activities.

The surface operation such as water impounded behind a dam was reported by Gupta [2002] to be the direct cause of a series of earthquakes up to M_s 6.3. Similar causes of induced earthquakes are related to the addition or building of mass, including the erection of tall buildings [Liu et al., 2015] and coastal land gain [Klose, 2012]. In contrast, the inverse of adding of mass, which is the removing of mass, has also been reported to have induced seismic activities [Emanov et al., 2014]. Similarly, surface extraction activities such as groundwater extraction [Amos et al., 2014, Klose, 2007, González et al., 2012] , mining [Li et al., 2007, Dreger et al., 2008, Lippmann-Pipke et al., 2011] and the construction of tunnels [Husen et al., 2011] have also been reported to induce seismic events. Foulger et al. [2018] reported that one of the most prominent locations of large scale induced mining is related to the Witwatersrand Basin in South Africa. The induced seismic activity in this area is directly related to the large extraction of gold and platinum.

Hydrocarbon extractions are no different to ore mining-induced seismic events. However, the review by Foulger et al. [2018] pointed out that induced earthquakes from hydrocarbon extraction due to reservoir compaction are few compared to other human activities. This is partly due to replacing the extracted fluid with water from bottom aquifers or the simultaneous injection of recovery fluids into the reservoir to displace hydrocarbons. One of the earthquakes believed to have been triggered by hydrocarbon extractions was reported by Calio et al. [2012]. It involved the extraction of CH_4 at a pressure greater than 10 MPa. The exact process that induced the seismic event is difficult to characterize because different processes happen simultaneously in such hydrocarbon extraction fields. Among them is the fluid injection into the subsurface, the extraction of fluid, the drilling of new wells and surface mass reduction. Suckale [2009] presented other seismic activities induced by oil and gas operations. Also, Gee et al. [2016] reported induced seismic activities due to differential compaction from gas fields. Changes in reservoir pressure due to fluid migration induced by oil withdrawal were reported by Nicholson and Wesson [1992]. In contrast to the idea that oil and gas operation could lead to significant seismic activities, [Foulger et al., 2018] reported only two instances of induced earthquakes caused by hydrocarbon extraction in the Middle East. In this region, vast volumes of hydrocarbon extraction have taken place for decades.

Mainly in extracting liquid hydrocarbons, other fluids are injected into the reservoir. Other inductions of earthquakes due to such injections have been reported by [Ellsworth, 2013]. Among them are hydraulic fracturing, CO_2 storage, geological hydrogen storage, toxic waste disposal and enhanced oil recovery methods. For long-term energy security, various economies worldwide have implemented underground storage of hydrocarbons. One of the earliest reported seismic incidents related to underground storage of hydrocarbon was recorded in Uzbekistan [Simpson and Leith, 1985]. Similar occurrences of induced seismic activities were reported in Spain when a depleted reservoir was designated to store volumes of natural gas. Again, it was reported that earthquakes were triggered after the commencement of the project.

Due to the increase in global warming, there is a whole range of methods to reduce the warming of the planet. Some of these proposals include the role of hydrogen as a fuel molecule and the storage of carbon dioxide (CO_2) in geological formations. While most of these proposals are welcomed by some environmentalists, others have criticized these recommendations based on previous induced seismic activities due to the injection of fluids into geological formations.

Hydraulic fracturing has also been at the centre of this debate. With the depletion of conventional hydrocarbon reservoirs, shales and tight formations have been the sources to complement the growing energy demand. Hydraulic fracturing involves the injection of fluids under high pressure to generate cracks or open up existing cracks in the oil and gas-bearing zones [Smith and Montgomery, 2015]. This is to increase the formations' permeability and enhance the free flow of hydrocarbons to the production well. [Foulger et al., 2018] indicated that about 21 earthquakes induced as a result of fracturing had been reported. One of those is the series of earthquakes reported in England after the commencement of a multistage hydraulic fracturing of the shale formation. The process was suspended after a series of 52 earthquakes between 2.0 to 2.3 magnitudes were recorded.

2.2 Reservoir Characterization

Reservoir characterisation is an essential part of an efficient exploration, development and exploitation of a reservoir. The optimal characterisation of a reservoir requires a multi-disciplinary analysis in the field of geology, petrophysics, geophysics, geostatistics and reservoir engineering [Cooke et al., 1999, Tonn, 2002, Lucia et al., 2003, Sena et al., 2011, Yu et al., 2011, López, 2017, Hadavand et al., 2018, Ma, 2019, Sharaf and Sheikha, 2021]. Across these disciplines, the five main methods employed in reservoir characterisation are data reconciliation, mapping, volumetrics, analysis of production data, and material balance [Baker et al., 2015]. While some methods are peculiar to some disciples, there is always a necessity to develop an optimal reservoir model with an interdisciplinary correlation of results. It is undoubtedly challenging to effectively connect all the various disciplines in reservoir characterisation, especially for unconventional reservoirs. Regardless, there have been significant improvements in the different models for the adequate characterisation of reservoirs [Haldorsen and Damsleth, 1993, Jia et al., 2012]. The global energy demand is projected to increase. To meet the increasing energy demand requires new technologies to exploit unconventional reserves. Similarly, calls for climate actions such as carbon geo-sequestration, hydrogen generation and geological hydrogen storage will require improvement in reservoir characterisation methods [Ozarslan, 2012, Simon et al., 2015, Osman et al., 2021].

Seismology remains one of the most relevant instruments in reservoir characterisation. The importance of seismology in reservoir characterisation is extensively covered in literature [Huang et al., 1997, Ullo, 1997, Jia and Cheng, 2010, Eidsvik et al., 2004, Aminzadeh, 2021]. Similarly, the application of microseismic monitoring is well documented in literature [Eisner et al., 2011]. Microseismic monitoring can pinpoint the periodic alterations in a reservoir as a result of physical, mechanical, and chemical changes that take place in the reservoir. Microseismic recordings provides information on source locations, time of occurrence, and the mechanisms that induced the seismic event. This information is then interpreted to predict the status and changes in the reservoir [Maxwell et al., 2010]. The advantage of microseismic method in reservoir characterisation is that it presents time-based information on mechanisms occurring in real-time. Microseismic information can be obtained either by a downhole or surface monitoring array. Literature shows that depending on the location and measurements made, any of the two methods of microseismic monitoring could be effective.

A study by Eisner et al. [2010] compared the event location solutions for downhole and surface arrays. The study presented a likelihood location theory effective for both methods of measuring induced seismic activities and concluded that both methods have similar uncertainties relative to a velocity model. Furthermore, ŚSwiech and Wandycz [2015] investigated the best method of microseismic data acquisition in polish geological conditions. The study concluded that downhole microseismic monitoring was the better of the two methods. Diller and Gardner [2011] emphasised a significant difference between the spacial location of events by the two microseismic methods despite accurate positioning shots for both methods. Microseismic data acquisition is mostly overwhelmed with large data sets that are hard to analyse in real and semi real-time [Wamriew et al., 2022a]. Therefore, machine learning methods are applied in various studies to overcome the challenge of the huge volume of data to process [Afra and Tarrahi, 2016, Qu et al., 2020, Raheem et al., 2021].

2.2.1 Microseismology in reservoir characterisation

Microseismology has been applied in different stages of reservoir exploitation. While many researches in the past implemented new methods of traditional microseismic data processing, new researchers are more focused on the implementation of artificial intelligence algorithms to provide faster and real-time data processing [Qu et al., 2020, Li et al., 2022a, LI, 2018, Aminzadeh, 2021, Rezaei et al., 2021, Raheem et al., 2021, Anifowose et al., 2019]. This section presents a summary of the application of microseismic monitoring and analysis to different oil geological operations that require reservoir characterisation.

The estimation of the petrophysical properties of reservoirs is integral to reserve and resource estimation. It provides insight into the best recovery mechanism to exploit a given formation effectively. While petrophysical measurements from well logs are adequate to estimate the reservoir properties, the correlation with seismic data better validates the measured properties and minimises errors Raheem et al. [2021]. Although seismic acquisition methods are well developed, artificial intelligence algorithms could enhance the effectiveness of validating and correlating seismic data with petrophysical properties for reservoir estimations. The prediction of reservoir porosity from microseismic data was investigated by Raheem et al. [2021]. The study compared different machine learning approaches. A novel method by García et al. [2019] showed that the introduction of artificial intelligence (AI) could widely exploit the uncertainty reduction in the spacial estimation of rock properties. The studies utilised a forward modelling method coupled with neural networks and genetic algorithms to characterise and identify the patterns between seismic traces of stack volumes and petrophysical rock properties. García et al. [2019] emphasised that accurate correlations could be obtained if errors are minimised during the structural seismic interpretation process and ensuring a structural complexity while modelling. The results produced a three-dimensional distribution of petrophysical properties like permeability, porosity and mineral volumes.

Furthermore, to implement an Enhanced Oil Recovery approach for a reservoir, a screening process is done to determine the suitable method to implement [Taber et al., 1997]. Screen criteria are based on reservoir petrophysical properties and fluid characteristics. It is evident that the petrophysical properties and fluid-rock flow mechanisms change over time as various reservoir intervention methods are implemented over the life of a given reservoir. Therefore, the availability of continuous microseismic data helps understand the geomechanical and petrophysical changes in the reservoir. Real-time data and analysis of such petrophysical changes could contribute to the initial screening process of feasible enhanced oil recovery methods. In addition, the inclusion of continuous changes in petrophysical properties based on microseismic events in reservoir modelling tools could increase the accuracy of reservoir model predictions. Afra and Tarrahi [2016] demonstrated that the implementation of EOR screening algorithms offers an underlying physical process taking place in the reservoir. Interestingly, scientists had ideas in the 1980s about implementing induced seismic vibration methods to increase the oil recovery of reservoirs. A considerable volume of scientific investigation has been carried out to access this methodology of enhanced oil recovery [Kuznetsov et al., 2002]. From analysis, this method was reported to increase relative permeability, decrease water cut, and increase the wells' production effectively. However, implementing such induced seismic EOR will require active and real-time data processing to detect any catastrophic earthquakes that might arise due to this EOR method. Microseismic monitoring have been utilised to monitor the reservoir changes during a SAGD enhanced oil recovery method [Maxwell et al., 2009]. The study presented that, microseismic detection coupled with tiltmeters showed that the injected steam was not equally distributed in the reservoir.

The "S" in CCUS (carbon capture utilisation and storage) is a vital component of the attainment of global climate goals [Were et al., 2019, Liu et al., 2021, Shaw and Mukherjee, 2022]. Simultaneously, the drive for accelerating carbon capture technologies is advancing quickly, with an estimated 980 $MtCO_2$/year of direct air capture of carbon by the end 2050 [IEA, 2021]. Despite the increase in CO_2 utilisation market, there remains a scenario of the vast excess of carbon that needs to be stored. Currently, storage in geological formations is at the forefront of storage mechanism [Harbert et al., 2020]. In addition, there are several experimental, R&D, pilot and commercial storage sites opened in the past several years. While the techniques of injecting CO_2 into geological formations are well advanced, the assurance of the safety of the storage sites for many years to come remains an unanswered question. Storage of CO_2 presents potential changes in the physical, chemical and mechanical state of geological formations and in-situ reservoir brine. Numerous researches in the past have looked into the potential and mechanism of CO_2 storage in geological formations [Pearce et al., 2021, Ajayi et al., 2019, Kelemen et al., 2019, Ringrose and Meckel, 2019, Bhanja et al., 2018, Rae et al., 2018, Pan et al., 2018].

Studies by Pearce et al. [2021] investigated the mineral changes in oil geological mediums due to CO_2 storage. The studies showed that CO_2 injection could alter the mineral composition of feldspar to kaolinite or illite and chlorite to siderite. Investigation by Williams-Stroud et al. [2020] indicated that such changes could result in microseismic events. Furthermore, injection of CO_2 into geological formations could result in pressure changes depending on the PVT conditions of the reservoir [Simmenes et al., 2013, Zoback and Gorelick, 2015]. CO_2 is injected at a supercritical state at a pressure of about 7.4 MPa and a temperature above 30^{o}C. This is expected to give CO_2 a higher density than the in situ fluid; however, this is not usually the case. Hence, there is a need for highly impermeable cap rock that prevents the migration of CO_2 to the upper layers of the formation [Shchipanov et al., 2022]. In addition, the build-up of CO_2 in the geological formations could result in a high-pressure build-up that could fracture cap rocks and formations as well as open up existing faults.

The uncertainties surrounding CO_2 storage warrant the implementation of monitoring techniques to track the viability of the process for the long term. From literature, various methods have been applied, including electrical resistance tomographic monitoring, Time-lapse gravity, Time-lapse seismic, microseismic monitoring, 4D seismic, 3D seismic, cross-well seismic tomography, satellite InSAR monitoring and CO_2 tracers. The pros and cons of the various techniques of monitoring CO_2 were investigated. Oye et al. [2013] presented research on the microseismic event recording in a CO_2 storage site. The microseismic events were recorded downhole, and the S-P phase arrival times were computed using a 3-D Eikonal solver. The results showed the occurrence of microseismic events in clusters within a limited spacial area which was attributed to CO_2 injection. Chen and Huang [2020] presented a workflow for determining the optimal surface seismic network for monitoring CO_2 storage sites. Chen and Huang [2020] recommended that, for the accurate estimation of microseismic events, three-component seismic stations are recommended over the one-component seismic station. Work by Shokouhi et al. [2021] emphasised the shortcoming of applying only reservoir simulation models for efficient storage of CO_2 in porous media. The work by Shokouhi et al. [2021] utilised a Multilayer Perceptron (MLP) and Long Short-Term Memory (LSTM) which are both data-driven and physics informed. The results show that physics-informed deep learning models with flow equations in their loss functions deliver better results.

Underground hydrogen storage has become a relevant topic in recent times due to the global demand for energy transition from fossil fuels to low carbon-based energy [Singh, 2022]. This is similar to the need for carbon sequestration and storage facilities. While hydrogen could be produced from any source, it could serve as a complementary to much renewable energy that could not be readily available in certain climates or seasons during some time of the year [Midilli et al., 2005]. One of the proposed storage for hydrogen for future use is the storage in geological formations [Tarkowski, 2019, Lemieux et al., 2020]. While this technology continues to advance, there are reports of the massive loss in the quantity of hydrogen in injected formations due to gas absorption and gas leakage[Berta et al., 2018, Muhammed et al., 2022]. The chemical and physical interaction of hydrogen the geological formation needs also to be analysed. In addition, the potential induction of microseismic events due to hydrogen storage also requires real-time monitoring. Especially with the idea of hydrogen being a readily available energy source, storage sites could be located in close proximity to residential areas, which amplifies the need for continuous monitoring of changes in such underground storage facilities. A review by Heinemann et al. [2013] emphasised the importance of ensuring the safety of underground storage of hydrogen.

Finally, at the end of a life cycle of a well, a well abandonment and decommissioning operation is implemented to isolate the to prevent further inflow on hydrocarbons or the migration of hydrocarbons upward which could contaminate the upper layer water bearing zones. While the techniques implored in well plugging and abandonment are well advanced, the longevity of the integrity of the well is difficult to predict. Hence in most cases, there is the need for continuous monitoring of wellbore integrity. The application of microseismic method is monitoring wellbore integrity through out the life cycle of a well have been studied by many researchers [Maxwell and Urbancic, 2001, Ajayi et al., 2011].

2.3 Distributed acoustic sensing

2.3.1 Brief History

One of the earliest mentions of acoustic sensing was reported by Bucaro et al. [1977]. The invention was a fibre optic cable with two sets of fibre bundles. One set was used to induce signals, while the other set was used to receive and detect signals [Kimbell, 2013]. The advances in the improvement of the first proposed fibre optic cannot only be accredited to the development of suitable sensing components but also the revolution in the communications components such as the fibre amplifiers, semiconductors for sources and detectors, couplers, splitters and other devices [Culshaw and Kersey, 2008]. Over time, acoustic sensing techniques have gained massive popularity in various fields, including oil and gas field monitoring, underwater sensing, atmospherics systems sensing, etc. In general, the innovation in acoustic sensing has been used to study the earth, the oceans and atmospheric conditions.

The advances in fibre-optic sensors could be reduced to two main categories: sensor technology and communication technology. Culshaw and Kersey [2008] presented a comprehensive analysis of the early contributors to the improvements of fibre optics sensing technology. From the work of Culshaw and Kersey [2008] the significant contributors are the Daul Path Interferometers, Faraday Rotation, Fiber Bragg Grating, Distributed Measurements and Spectroscopy. The innovations in the Dual-path interferometers were partly due to the effective measuring capabilities in the changes in the differential delay between a reference and a signal arm. On the other hand, Faraday Rotation describes that the rotation of light in its plane depends on the value of the magnetic field component when propagating through solids. The Faraday Rotation is believed to be straightforward in theory and simple in practical implementation. The improvements in the understanding of spectroscopy consequently gave rise to the developments in Fiber-optic-based spectroscopy. Currently, there are new component technology developments and applications, and the upgrades are expected to continue to be on the upward trend [Shinohara et al., 2022, Fernández-Ruiz et al., 2022].

The older generations of technology based on the variation of Rayleigh backscattering (RBS) intensity, like the distributed vibration sensor (DVS), were only triggered by the existence of vibration in the medium. However, the amplitude and the phase were misrepresented. On the other hand, new technologies of the RBS, like the DAS, can represent the amplitude, frequency, and phase information correctly.

One of the crucial advantages of the DAS system is the ability to represent the waveform in high definition; hence numerous parameters could easily be accurately quantified via sophisticated data processing methods. Another benefit that fiber-optic DAS brings to geophysical data acquisition is deployment flexibility, especially in downhole acquisition. Unlike the conventional geophones and accelerometers which are often clamped on the wireline, the fiber-optic DAS cable can be loosely lowered down the borehole, i.e slickline deployment [Hartog et al., 2004, Parker et al., 2014], attached to the tubing with hard clamps [Daley et al., 2013, Mateeva et al., 2013], or clamped and cemented behind the casing i.e permanent deployment [Mateeva et al., 2014, Reinsch et al., 2015, Shulakova et al., 2022] as shown in Figure 2-4. Cementing the cable on the wellbore provides adequate coupling with

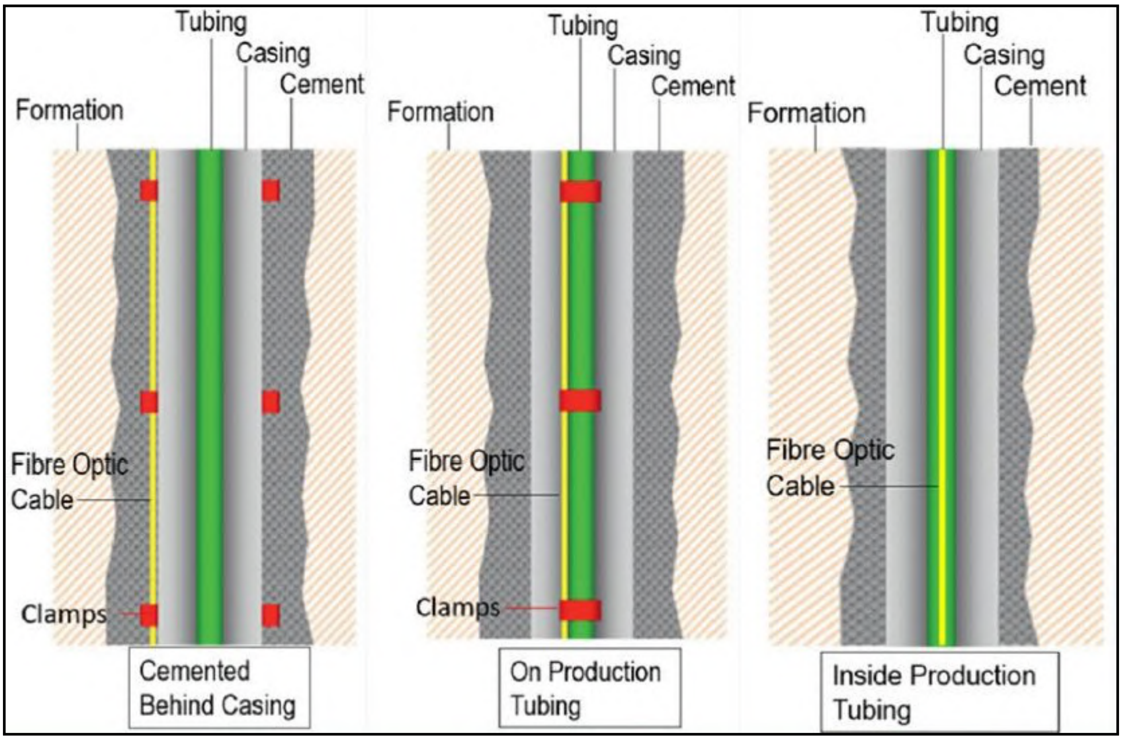

Figure 2-4: Fibre optic cable coupling options in a borehole survey. Modified from Fenta et al. [2021]

the formation that improves detection sensitivity and accuracy leading to high SNR data. As a result, the latter deployment strategy is more effective for microseismic or passive seismic monitoring as the data can be acquired without interrupting field operations.

2.3.2 Applications and Recent Progress of the DAS system

DAS uses an ordinary or engineered fiber-optic cable for seismic monitoring. In its deployment, an Interrogation Unit (IU) is attached at the end of the fiber-optic cable near or on the surface. The IU measures deformations (contractions or extensions) along the fiber-optic cable caused by propagating seismic waves. This sort of measurement is known as Distributed Acoustic Sensing. "Distributed" because any part of the fiber cable can be deformed and logged for seismic information.

DAS measurements are straightforward in concept. A laser pulse is sent down the fiber cable by the IU. As the pulse propagates through the cable, portions of it undergo Rayleigh back-scattering due to the minute heterogeneities in the cable [Hartog, 2017]. When a seismic wave interacts with the cable, deforming it, it causes changes in the patterns of the back-scattered light, which is then converted into seismic data. The time it takes the back-scattered pulse to travel back to the IU allows for an accurate location of the point of deformation. Due to the fast speed of light, the entire length of the fiber-optic cable can be interrogated with laser pulses at frequencies far greater than those of seismic waves. Depending on the length of the borehole, the interrogation frequencies typically range from 10 to 100 KHz, with higher frequencies known to produce higher SNRs due to redundancy. Nonetheless, the length of the borehole restricts the highest permissible frequency.

The implementation of DAS in various science and engineering sectors has been increasing over the last few decades. Some authors have classified the application of the DAS system into event detection and the replacement of traditional strain sensors. Others have classified the application of DAS systems based on the size of the structure: Long length structures, Stationary composite structures and Moving structures [Stajanca et al., 2018, Hussels et al., 2019, Tejedor et al., 2021]. The long structures include highways, long bridges and railways, the vast fixed structure includes geological formations, wellbores, and oil and gas platforms, and the moving structures include aeroplanes, wind turbines, etc. We discuss the application of different DAS based reflectometers in these subcategories.

Long structures and pipelines, and railways are vital in the transport of energy, goods and people across the world. However, their structure cover long distances, primarily via inaccessible territories and harsh conditions. Stajanca et al. [2018] investigated the reliability of using DAS to detect the pinhole leakage in gas pipelines. His work employed direct fiber wrapping around the pipeline, and weak leak-induced vibrations along the pipeline were detected. The study concluded that the presented approach could detect leaks on short- to medium-length gas pipelines well below 1% of the pipeline flow. Similarly, Hussels et al. [2019] concluded from his work that fibre-optic distributed acoustic sensing coupled with a suitable application geometry of optical fibre sensor provides the ability to track the propagation of acoustic waves in the pipeline, which were in good agreement with theoretical derivations. Yatseev et al. [2020] presented a study based on an optical frequency domain reflectometry (OFDR) method to measure the absolute deformation in cables. The survey by Yatseev et al. [2020] showed that by using 110 ns pulses, the deformation in the cable could be detected with 0.16 μm at a 10 Hz repetition rate. Furthermore, leaks caused by deformation in a structure of different shapes were studied by Yang et al. [2021]. Depending on the shape of the hole that caused the leak, the acoustic effects were different. Circular holes then have a steep start and decrease over time, while the square-shaped holes have a maximum signal of 0.1 ms and begin to attenuate.

Furthermore, the application of DAS for the structural health of bridges and the load changes have been reported in literature. For example, Liehr et al. [2019] demonstrated how a DAS based approach to wavelength-scanning coherent optical time-domain reflectometry (WS-COTDR) could be used to monitor the structural health of bridges which concluded that the reference measurement-based WS-COTDR is advantageous in resuming interrupted measurements at any time. In general, the DAS system is suitable for completing complex tasks like measuring the percentage of each fluid phase in a multiphase flow in pipelines. The railway industry has similarly improved structural monitoring techniques by utilizing DAS. Kowarik et al. [2020]demonstrated that distributive fibre optic sensing could determine the position, velocity and bogie cluster during the movement of trains. Hubbard et al. [2021] employed the OFDR and ϕ-OTDR dynamic distributed fibre optic sensing technologies to monitor the dynamic strain of several wind turbines (over 10 km) by a single fibre optic cable. The comparison of the result of both methods is with 5%

relative accuracy. However, the ϕ-OTDR is much more capable of measuring more minor changes in natural frequencies caused by structural damage.

The DAS system has been mounted on aircraft to track physical movements and fluid movies along with the aircraft. This has been used to coordinate the direction of the aircraft along tracks in airports and also measure the structural health of multiple components of aircrafts [Chen et al., 2020, Cai et al., 2021].

DAS is the frontier of microseismic monitoring. Natural events of microseismic activities in the subsurface have been reported in the literature. Furthermore, microseismic events are induced due to continuous human interaction with the subsurface through activities such as construction and drilling for fossil fuel [Huang et al., 1997, Ullo, 1997, Eidsvik et al., 2004, Jia and Cheng, 2010, Eisner et al., 2011, Aminzadeh, 2021]. Therefore, microseismic monitoring is implemented to detect any change in subsurface activities over a period of time. These changes could be physical, mechanical or chemical interactions. The recording made by the microseismic detection device provides a sense of the time and location of the microseismic event. Also, it could be interpreted to predict the extent, status and future changes that could occur [Maxwell et al., 2010]. From literature, it is evident that the DAS system has been employed not only for the detection of microseismic activities that could lead to earthquakes and natural catastrophes but also the DAS system has been employed mainly in the oil and gas industry for the reservoir characterization right from the onset of exploration till the end of the field. Some of the significant processes where DAS microseismic monitoring has been utilized include the detection and location of oil and gas deposits, detection of seal and caprock integrity, the detection of wellbore trajectory for drilling, the monitoring of wellbore integrity, the detection of petrophysical properties of a reservoir, the detection of the extent of hydraulic fracturing, the estimation of the effectiveness of an enhanced oil recovery method. The microseismic method is advantageous in subsurface characterization due to the features of presenting time-based information in real-time. In the oil and gas industry, the microseismic events could be recorded by either placing the receivers downhole in a well or on the surface. Both methods have been reported to be effective [Eisner et al., 2011]. DAS data have been implemented for Enhanced Oil recovery screening

[Afra and Tarrahi, 2016]. Similarly, the potential of the SAGD enhanced recovery method was estimated by microseismic monitoring [Maxwell et al., 2009]. Molenaar et al. [2012] is believed to have reported the first application of DAS in monitoring and diagnostics of hydraulic fracturing. The present real-time monitoring of the dynamic process of hydraulic fracturing. The DAS system's broad frequency characteristic helped distinguish between different active perforation clusters. The DAS system replaced the DTS system due to the limitation of the DTS systems to provide quantitative estimations of the injection fluid volumes [Molenaar et al., 2012].

The DAS technology has successfully complemented traditional sensing methods across multiple sectors and industries. The features that make the DAS system advantageous are discussed in subsection 3.4.2.

2.3.3 DAS in reservoir characterisation

For a long time, three-dimensional Vertical Seismic Profiling (3D-VSP) has been considered appealing for imaging complex subsurface structures, both in exploration and time-lapse monitoring for the characterization of reservoirs. However, the associated costs and complexity of installing geophone arrays in a well, as well as the scarcity of available wells, have hampered the widespread deployment of 3D-VSP [Mateeva et al., 2014]. These challenges can essentially be reduced by the use of the novel DAS technology.

The first demonstration of the capability of use of DAS for VSP acquisition was by Mestayer et al. [2011]. There has since been tremendous progress in the development and testing of DAS technology that has resulted in its almost unrivalled acceptance for a wide range of field seismic measurements. In relation to reservoir characterization, DAS has been applied to microseismic monitoring and analysis [Walter et al., 2020, Hudson et al., 2021, Lellouch et al., 2022], hydraulic fracture monitoring [Liu et al., 2020, Ichikawa et al., 2021], as well as in flow and production monitoring [van der Horst et al., 2013, Finfer et al., 2014, Naldrett et al., 2018].

Traditional detection algorithms were applied to DAS in the early stages, but they were largely ineffective. According to Hull et al. [2017], only 31 DAS events were discovered when monitoring hydraulic stimulation, compared to 785 events on the traditional geophones. In addition, Webster et al. [2016] quantifies DAS-based events detection to be a paltry 10 percent of the geophone-based. Furthermore, Molteni et al. [2017] demonstrates that DAS is only capable of detecting events of greater magnitude. On the other hand, the waveform characteristics of microseismic events recorded on DAS were interesting, displaying modes of transformation as well as reflections and scattering. Despite these limitations of event detection capabilities, several attempts have been made to locate the events [Wamriew et al., 2022b, 2021b, Hull et al., 2017, Karrenbach et al., 2017, Molteni et al., 2017, Webster et al., 2016]. However, while the advantages of DAS-based location, which primarily consist in positioning an event along the fiber axis, became apparent, the symmetry problem that arises from recording on a single fiber severely curtailed the ability to extract unambiguous event locations from recorded waveforms. A beamforming approach for event detection and location without azimuthal information was demonstrated by Lellouch et al. [2020] using a single vertical fiber. The detection capabilities of DAS were approximately 30% of those of traditional geophones, suggesting a considerable improvement as compared to the use of conventional detection approaches [Mondanos and Coleman, 2019]. After trace-by-trace picking, Karrenbach et al. [2019] demonstrate that DAS recordings can be used for travel-time minimization in unconventional reservoirs where horizontal DAS fibers are deployed. This is based on a known velocity structure and has been demonstrated by Verdon et al. [2020]. In spite of the cylindrical symmetry problem of single vertical fiber-optic DAS measurements, it is possible quantify reasonable uncertainty in the DAS measurements by use of complementary production logs. Arrivals in the deviated and vertical regions of the well can be detected for particular events, allowing many previously degenerate planes to be resolved. In addition, Verdon et al. [2020] employed deviating well recordings to estimate event location without the necessity for individual channel selection. Instead, they used the DAS records to measure numerous geometrical characteristics and localized the events using a constant background model. In terms of observed events, they found that downhole DAS surpassed a surface recording array, which is routinely employed for microseismic monitoring [Eisner et al., 2010], by nearly an order of magnitude.

2.4 Deep Learning

Deep learning [LeCun et al., 2015] is a branch of machine learning that has gained traction in the field of seismic data processing, analysis, and interpretation due to its computational efficiency, adaptability, and inherent ability to extract high-level features from recorded seismic waveforms with little to no manual engineering. Developed for pattern recognition in computer vision, deep learning models have high-level feature extraction mechanisms that enable them to transform raw data into a subset of feature vectors, allowing learning to take place. This makes them a perfect candidate for classification or regression tasks. Detection of seismic events is a classical example of a classification task, while inversion to locate the origin of the seismic energy can be considered a multidimensional regression problem. The most popular deep learning architectures in seismology are recurrent neural networks (RNNs) and convolutional neural networks (CNNs). The latter is preferred for its processing speed and ability to handle large volumes of data; whilst the former's ability to recognise sequential patterns in data and use those patterns to predict the next possible scenario makes it the de facto time series analysis tool.

Because deep learning models are data-driven, they require a significant amount of data for training and validation. As a result, they are best suited to processing seismic data recorded by DAS, which collects massive amounts of data. Binder and Tura [2020] employed convolutional neural networks to automatically detect microseismic events on data acquired by DAS along a borehole during a hydraulic fracture operation. They compared the results with those from a surface geophone array and observed that, despite the low signal-to-noise ratio in the DAS data, the neural network was able to detect 167 new events that were not registered by the geophones. Huot et al. [2022b] reported a 98.6% accuracy of deep learning models trained with hyperparameters obtained by Bayesian optimisation on 7,000 manually selected microseismic DAS events. They concluded that by the application of AI, the model was able to predict more than 100,000 events, which enhanced the prediction of the Spatio-temporal fracture developments, which otherwise could not have been detected by traditional methods. Furthermore, to overcome the problem of signal-to-noise ratio that makes the data processing challenging, Qu et al. [2020] introduced a new methodology based on fixed segmentation coupled with a support vector machine (SVM) model. The proposed methodology allowed the identification of the best features and the optimal number of features required for producing accurate results. From the comparative analysis, the presented model has accurate results compared to CNN and the short-term average and long-term average ratio (STA/LTA) conventional approach. Other applications of deep learning for the detection of seismic/microseismic activities are well documented in [Hernandez et al., 2022, Shaheen et al., 2021, Mousavi et al., 2020] and [Kuyuk and Susumu, 2018].

Deep learning has also been applied to tasks other than the detection and classification of seismic activities. Wamriew et al. [2022a] demonstrated the potential of application of deep learning to the inversion of microseismic data. They showed that a CNN model was capable of locating microseismic events and reconstructing the velocity model simultaneously in real-time from seismic waveforms. Tanaka et al. [2021] employed a deep learning model to perform moment tensor inversion of acoustic emissions during a hydraulic fracturing experiment of granite rock and obtained 54 727 solutions.

Due to their computational efficiency, the models can be used in the field to process the data in real-time during its acquisition, thereby scaling down the amount of data to be stored while providing necessary information that could help optimise the field operations. Huot and Biondi [2018], Huot et al. [2022a], Wamriew et al. [2021b] emphasised that without the complete automation of microseismic data processing, large volumes of collected data could be wasted due to human processing limitations.

2.5 Conclusion

It is well established in literature that the active and real-time recording and processing of microseismic activities is very essential for the characterisation of geological

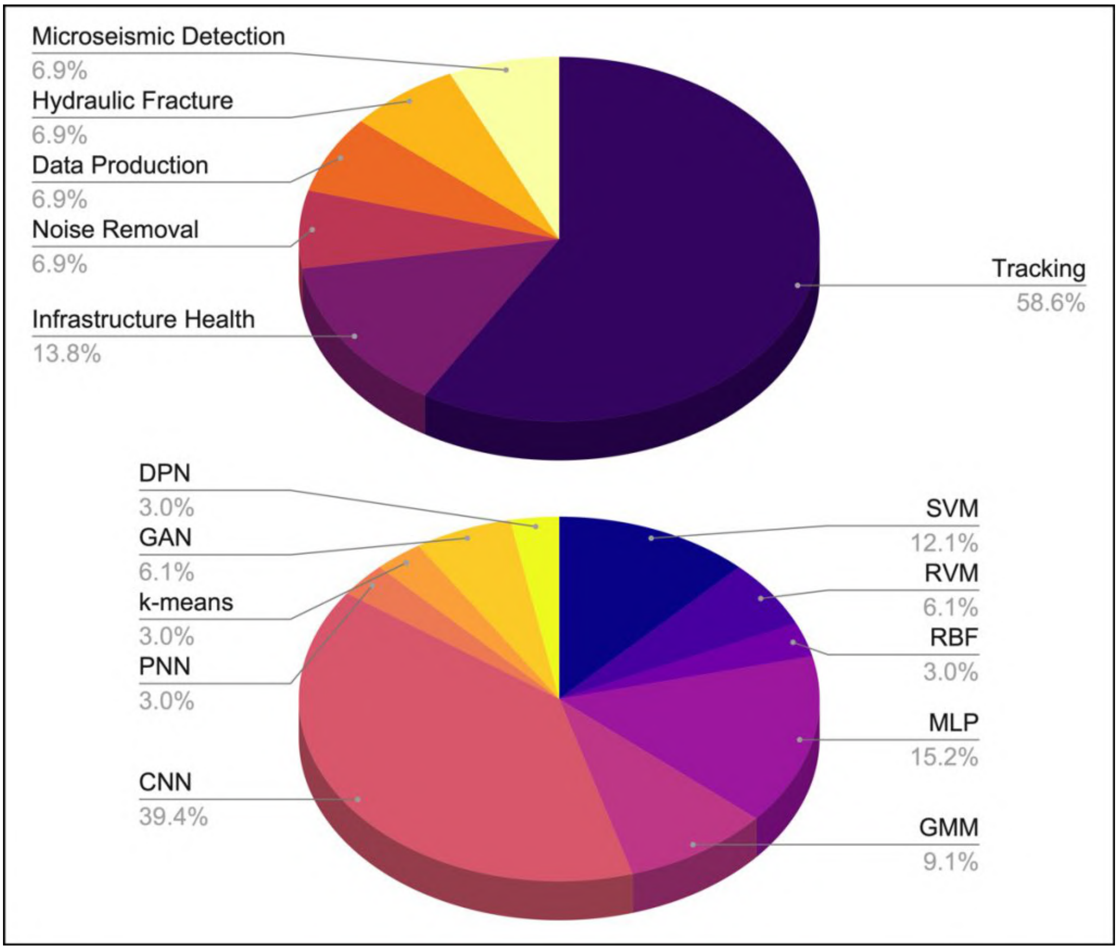

Figure 2-5: **Top:** Applications of DAS to geoscience. **Bottom:** Machine learning approaches used to process DAS data.

formations. Right from the exploration of the field to the appraisal, the development, production, enhanced and improved oil recovery methods, abandonment well monitoring or utilisation for the storage of CO_2 or H_2. Also the challenges of physical processing of huge volumes of microseismic data and the limitations imposed could be overcome by the implementation of automated artificial intelligence models, as have been developed in recent times, that could predict events and analyse geological changes in reservoirs. In this study, we demonstrate the use of two cutting-edge technologies - Distributed acoustic sensing (DAS) and Deep learning - for microseismic monitoring and analysis. Numerous studies based on DAS and artificial intelligent algorithms have increased in recent years. For the purpose of this thesis, we restrict ourselves to downhole array of DAS and convolutional neural networks. The characteristics of the DAS to provide vast volumes of data is beneficial to convolutional neural networks, which perform better with a high quantity of data. The computation and processing time of the data is also expected to increase with the development of special processors and components to decrease computational time. Due to these reasons, the application of DAS could only be at its early stage. Figure 2-5 shows a summary of applications of DAS in Geosciences and the use of machine learning in processing data recorded by DAS.

"if you can't explain it simply, you don't understand it well enough."

Albert Einstein

Chapter 3

Theory

3.1 Detection of microseismic events

During microseismic monitoring, huge volumes of data are recorded due to the large number of receivers usually deployed either downhole or on the surface. It becomes impractical or even impossible to manually process this data owing to its extensive volume but also due to the low SNR characteristic of microseismic data. Automated approaches are therefore used to process this data for arrival time picking and event detection. A good practice is usually to filter the data to improve the SNR by suppressing those frequencies that fall outside the frequency band of the source. For microseismic monitoring, the frequency bandwidth (f_b) is in the range $80Hz \leq f_b \leq 200Hz$. A low-pass filter or a band-pass filter with a minimum phase response is used at this pre-processing step. Care should however be taken to avoid *Gibbs phenomenon* which would greatly distort the arrival time picks [Maxwell, 2014].

A further step to improve SNR entails stacking of the waveform traces. Stacking helps to suppress random noise and is done by summing the traces recorded by neighbouring receivers. The SNR is boosted by a factor proportional to the number of stacked traces. The main challenge in this approach is to get the accurate time-shift of the traces corresponding to their receiver positions.

Numerous algorithms for events detection and arrival time picking have been developed over the years, but for the purpose of this thesis, we constrain ourselves to Fingerprint and Similarity Thresholding, Short-time/ long-time average and template matching, for their computational efficiencies and relevance to deep learning. Interested reader is referred to Akram and Eaton [2016] for a comprehensive theoretical review and appraisal of other event detection and arrival picking approaches and algorithms.

3.1.1 Fingerprint And Similarity Thresholding (FAST)

The FAST algorithm [Yoon et al., 2015] detects similar waveforms by combining computer-vision approaches with large-scale data processing techniques. It employs feature extraction techniques to generate waveform fingerprints containing essential outstanding features and serving as compressed waveform approximations. Locality-sensitive hashing (LSH), a commonly used approach for high-dimensional approximation nearest-neighbour search, can then be implemented to lessen the computational burden for comparing distinct pairs. As a result, FAST ranks high on general applicability, sensitivity and computational efficiency and is the most suitable for integration into deep learning event detection and location algorithms. Figure 3-1 presents a summary of workflow in the implementation of FAST algorithm.

3.1.2 Short-Time Average / Long-Time Average (STA/LTA)

The STA/LTA method [Earle and Shearer, 1994] is perhaps one of the most popular event detection and arrival picking approach used both in earthquake and microseismic event detection. It's main leverages over other methods are the fact that:

- It is has general applicability i.e, it is capable of detecting a wide range of seismic events without background knowledge of their waveform patterns or even source information.
- It is computationally efficient and can therefore be employed for event detection in real-time.

It's main drawback is it's low sensitivity and the fact that it can fail to detect events or cause false triggers in challenging cases such as overlapping events or events drowned in noise and can therefore lead to incomplete catalog. This is of

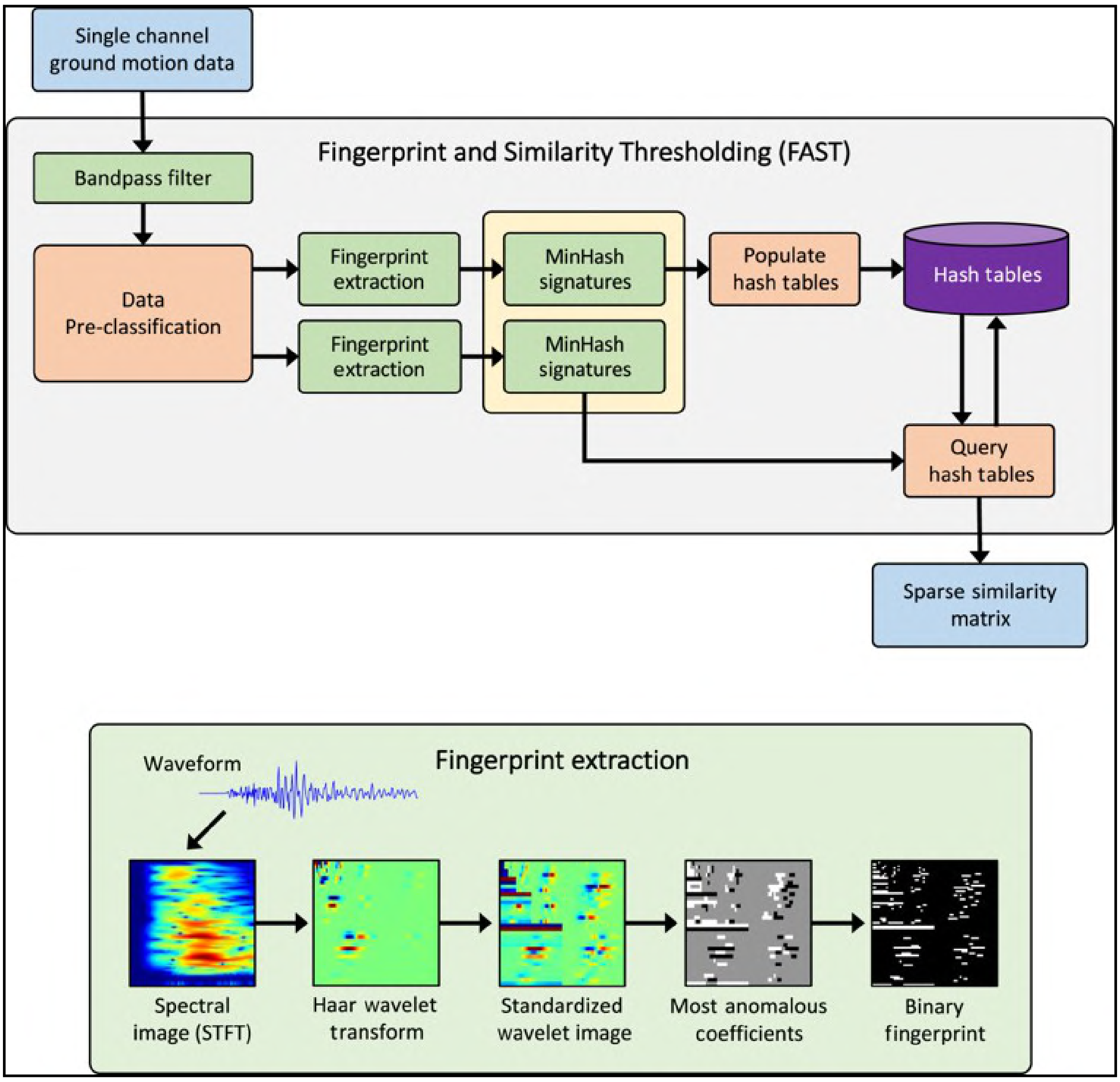

Figure 3-1: Single-station implementation of the FAST approach.**Top:** Illustration of the main workflow in the FAST algorithm. **Bottom:** Fingerprint extraction and conversion into binary format. Source: [Bergen and Beroza, 2018]

course undesirable, especially in microseismic monitoring where events usually have low SNR and there are high chances of overlapping arrivals. Nonetheless, with proper noise suppression during the pre-processing stage, the STA/LTA approach still proves handy for microseismic data.

In its implementation, the STA/LTA approach utilizes two sliding windows of distinct lengths (i.e short time and long time windows) to compute the absolute amplitude of seismic signal within each window. It then determines the average amplitudes of the signal within each window and outputs the ratios of the short term average window to the long term average window. A user defined threshold is used to compare the computed ratios and an event is detected if the computed ratio exceeds the predefined threshold. Care must be taken when selecting this detection threshold as smaller threshold values may cause false detection while larger values might miss the events altogether. A general expression for STA and LTA parameter computation can be formulated as follows:

$$\mathrm{STA}\,(i) = \frac{1}{L_s} \sum_{j=1}^{L_s} a\,(i)^2\,, \tag{3.1}$$

and

$$\mathrm{LTA}\,(i) = \frac{1}{L_l} \sum_{j=1}^{L_l} a\,(i)^2\,, \tag{3.2}$$

where L_s and L_l are the lengths of the short and long windows respectively and a is the amplitude of the signals at each data sample within the window. Oye and Roth [2003] found out that the STA window is more sensitive to rapid changes in amplitude, whilst the LTA window corresponds to the seismic trace's background noise. The energy ration (ER) of the STA/LTA values can then be calculated by dividing Equation 3.1 by Equation 3.2 as follows:

$$\mathrm{ER} = \frac{\mathrm{STA}\,(i)}{\mathrm{LTA}\,(i)} \tag{3.3}$$

The effectiveness of the STA/LTA algorithm is dependent on three parameters: L_s, L_l, and the detection threshold value. A suggestion by Akram and Eaton [2016] is to use an LTA window that is five to ten times the length of the STA window, and an STA window that is three to five times the dominant period of the source signal. The selection of an appropriate detection threshold is based on the dataset and changes with amount of noise, hence it is advisable to conduct tests on a portion of the data before making the choice of the threshold value. Figure 3-2 illustrates the STA/LTA approach.

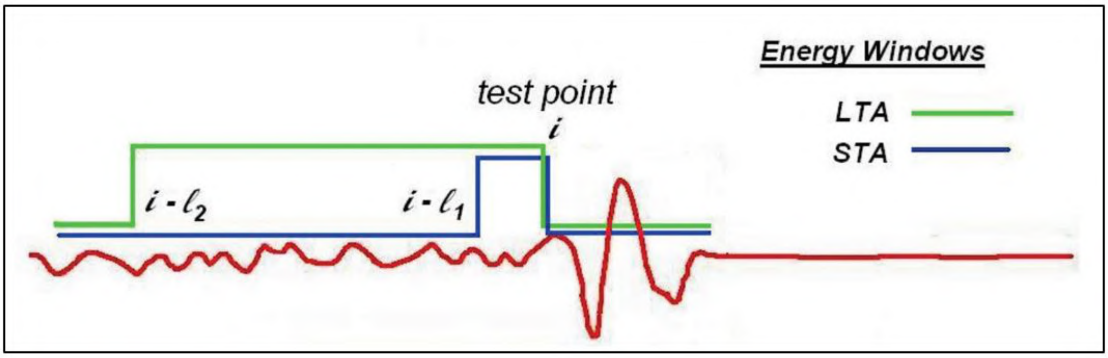

Figure 3-2: Single-station implementation of the STA/LTA approach. Red is signal, green and blue are is respectively LTA and STA energy windows. LTA should be around 5 to 10 times the length of STA, while STA should be about 3 to 5 times the dominant period [Akram and Eaton, 2016]

3.1.3 Template matching

The template matching method overcomes the low sensitivity limitation of the STA/LTA approach by taking into consideration the entire seismic waveform rather than just the sudden arrivals of P- and S-waves. It thus has high sensitivity and is suitable for detecting events even in complicated settings such as the presence of high cultural noise, overlapping arrivals and sparse receiver arrays. It uses the cross-correlation technique to determine the similarity between two waveforms regardless of their time lag. In so doing, events with similar source information to the template event (for example, location and focal mechanisms) can easily be detected. In its implementation, a cross-correlation coefficient is computed between a template event waveform and subsequent time windows of a continuous waveform. A predefined detection threshold value is set, and an event is declared if the computed correlation coefficient surpasses the threshold value [Gibbons and Ringdal, 2006]. Before cross-correlating the raw continuous waveforms with the template events, it is recommended to pre-process the waveforms using a polarization-preserving 3-C normalisation mechanism akin to the automated gain control (AGC) commonly used with reflection seismic data. This procedure calculates a normalised modulating amplitude function for all the receiver components by convolving the envelop amplitude with a chosen triangular time operator, as shown in Equation 3.4, [Eaton, 2018].

$$\mathbf{A}_M(t) = A_E * \Delta(t, t_\Delta). \tag{3.4}$$

Here, $\mathbf{A}_M$ is the modulating amplitude function, A_E is the envelope amplitude for a particular receiver, $\Delta(t, t_\Delta)$ is a triangular time operator and $*$ denotes convolution. Caffagni et al. [2016] reported that a choice of t_Δ approximately five times the duration of the source pulse had the effect of improving the detection capability of the approach to weak events without changing the polarization information of the events compared to when only the normalised cross-correlation coefficient is used. They provided an event detection workflow (Figure 3-3) based on the matched filtering template matching approach, for downhole microseismic data.

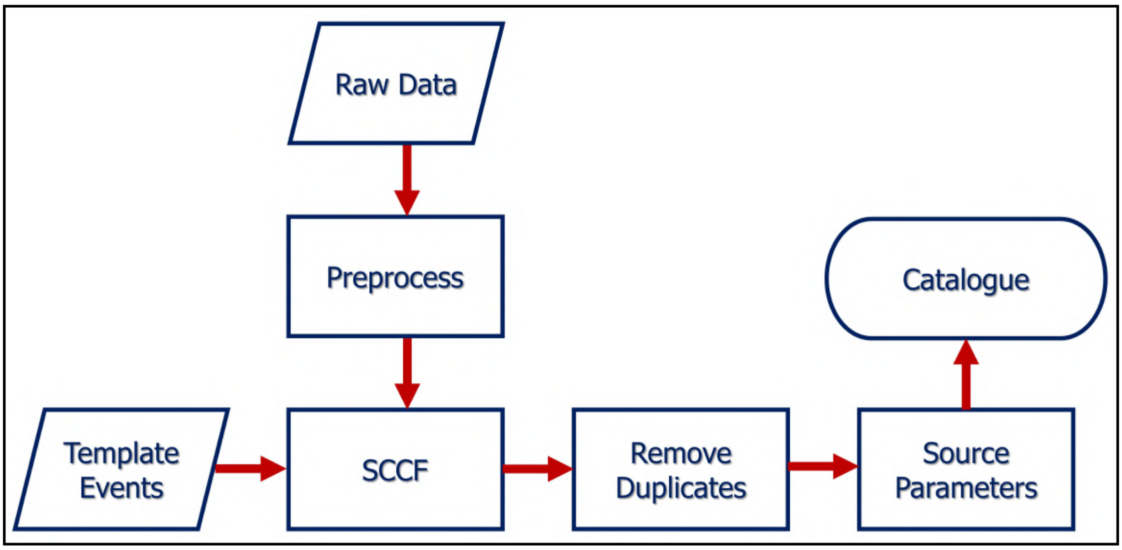

Figure 3-3: Event detection workflow using the matched filtering template matching approach for downhole microseismic data.

Following this approach, the stacked cross-correlation function (SCCF) can be calculated using Equation 3.5 as follows:

$$\text{SCCF} = \sum_{j=1}^{N_C} \sum_{k=1}^{N_R} \Psi_k^j(t), \tag{3.5}$$

where N_R and N_C are the number of receivers and receiver channels respectively and Φ_k^j is the cross-correlation coefficient between the master event and j^{th} channel of the k^{th} receiver [Eaton, 2018].

One significant drawback of the matched filtering template matching method is that it requires prior knowledge of the waveform characteristics of the template/-master event, which limits its potential utility. The templates are frequently selected by inspection of the events database or by manually picking the arrival of sudden body waves from continuous waveforms. As a result, it is neither an efficient nor a comprehensive method for detecting recurring events or events with very low SNR and unknown source information. Furthermore, the requirement for a human expert to inspect and select the template event lowers the computational efficiency of the matched filtering approach. Consequently, more generalizable variations of the template matching approach, such as the subspace detection [Harris, 2006] and the empirical subspace detection [Barrett and Beroza, 2014], have been developed that are adaptable to a wider variety of continuous waveforms and comparable non-repeating sources.

3.2 Location of microseismic events

Determination of the hypocenters of induced seismic events is one of the key enablers to reservoir characterization as the distribution of the hypocenters give a good picture of the fracture network within the reservoir.

The conventional methods for determining the hypocenter of induced microseismic events can be classified into two broad groups: travel-time inversion based approaches and migration based approaches [Li and van der Baan, 2016]. The former relies on the arrival-time picking and the back-azimuth information obtained through analysis of hodograms. As a result, it is vulnerable to mistakes related to arrival time picking and is more likely to fail in circumstances of very low SNR when either the P-wave or S-wave arrivals, or both, cannot be established, as is frequent with microseismic data. Despite this, the arrival-time-based approach is still the most commonly utilised hypocenter location method in real-time during microseismic monitoring. As a result, many studies have been carried out to improve its computational efficiency and event location accuracy.

Migration based approaches make use of the complete waveform of a detected event and therefore pay little to no attention to P- and or S-wave picks. Consequently, the approaches are suitable for use in cases when the SNR is low. These methods include, finite-difference waveform inversion technique...

Recently, machine/deep learning techniques, based on supervised learning have been applied for the detection and location of the hypocenters of microseismic events as well as velocity model reconstruction [Wamriew et al., 2021b, 2022a]. The techniques differ from the conventional approaches in the sense that they are intensively data driven and rely on the "learning" capabilities of the neural networks to perform inversion. In their implementation, the neural networks are presented with example waveforms (raw or processed) and their corresponding hypocenter and or velocity model information. The neural network therefore learns to associate the waveform patterns to the source information such as hypocenter coordinates, velocity model or even source mechanisms. The accuracy of the inversion, depend on the accuracy of the forward models used, the quality training data and how best the neural network learnt during training. The latter is further dependent on the quality of data presented to the network, the architecture of the network and its hyperparameters.

3.3 Source mechanisms of microseismic events

3.3.1 The moment tensor

Source mechanisms of microseismic events provide useful information about the properties and fracture network of the reservoir. This information is key enabler to the characterization of the reservoir. In the case of reservoir stimulation, the tracking of the events hypocenters and source mechanisms both in space and time at various stages is crucial for understanding the response of the reservoir rocks to stimulation [Eisner et al., 2010]. Du et al. [2011] emphasize the importance of extracting additional source mechanism information such as fault-plane orientation, source radius, source type, slip amount and slip direction, in addition to the event locations for a better understanding of reservoir processes.

Since microseismic data are records of motions of the earth particles as a result of release of stress energy, the quantitative description of these motions is based on the theory of linear elasticity given by Equation 3.6.

$$\rho \partial_t^2 u_i = \partial_j \sigma_{ij} + f_j, \tag{3.6}$$

where ρ is the particles mass density, u_i is the particle displacement, $\sigma_{ij} = \sigma_{ji}$ is the stress tensor and f_j is the force vector.

This theory establishes the foundation and provides the background for the discussion of modeling, processing and inversion of microseismic data.

In order to understand the source parameters of a seismic displacement at some point x from the seismic source, the solution to Equation 3.6 can be expressed as:

$$u_i\left(x,t\right) = G_{ij}\left(x,t;x_0,t_0\right) f_j\left(x_0,t_0\right), \tag{3.7}$$

where x_0 and x are the source and receiver positions respectively, t_0 and t are the corresponding source and receiver times while G_{ij} is the Green's function which gives the impulse response at the receiver position.

For a force couple separated by a distance d in the x_k direction the displacement can further be expressed as:

$$u_i\left(x,t\right) = \frac{\partial G_{ij}\left(x,t;x_0,t_0\right)}{\partial x_k} f_j\left(x_0,t_0\right) d, \tag{3.8}$$

Equation 3.8 can be written as:

$$u_i\left(x,t\right) = \frac{\partial G_{ij}\left(x,t;x_0,t_0\right)}{\partial x_k} M_{jk}\left(x_0,t_0\right), \tag{3.9}$$

where M_{jk} is the second rank moment tensor given by

$$M = M_0 \begin{bmatrix} M_{xx} & M_{xy} & M_{xz} \\ M_{yx} & M_{yy} & M_{yz} \\ M_{xy} & M_{xy} & M_{xy} \end{bmatrix}, \tag{3.10}$$

where M_0 is the scalar moment magnitude which is a measure of the strength of the earthquake induced by a fault slip as was first defined by Aki [1966] as:

$$M_0 = \mu A \overline{D}, \tag{3.11}$$

where μ is the shear modulus at the source location, A is the surface area of the ruptured fault plane and $\overline{D}$ is the average fault slip.

The moment tensor can be represented by a system of nine force couples as shown in Figure 3-4.

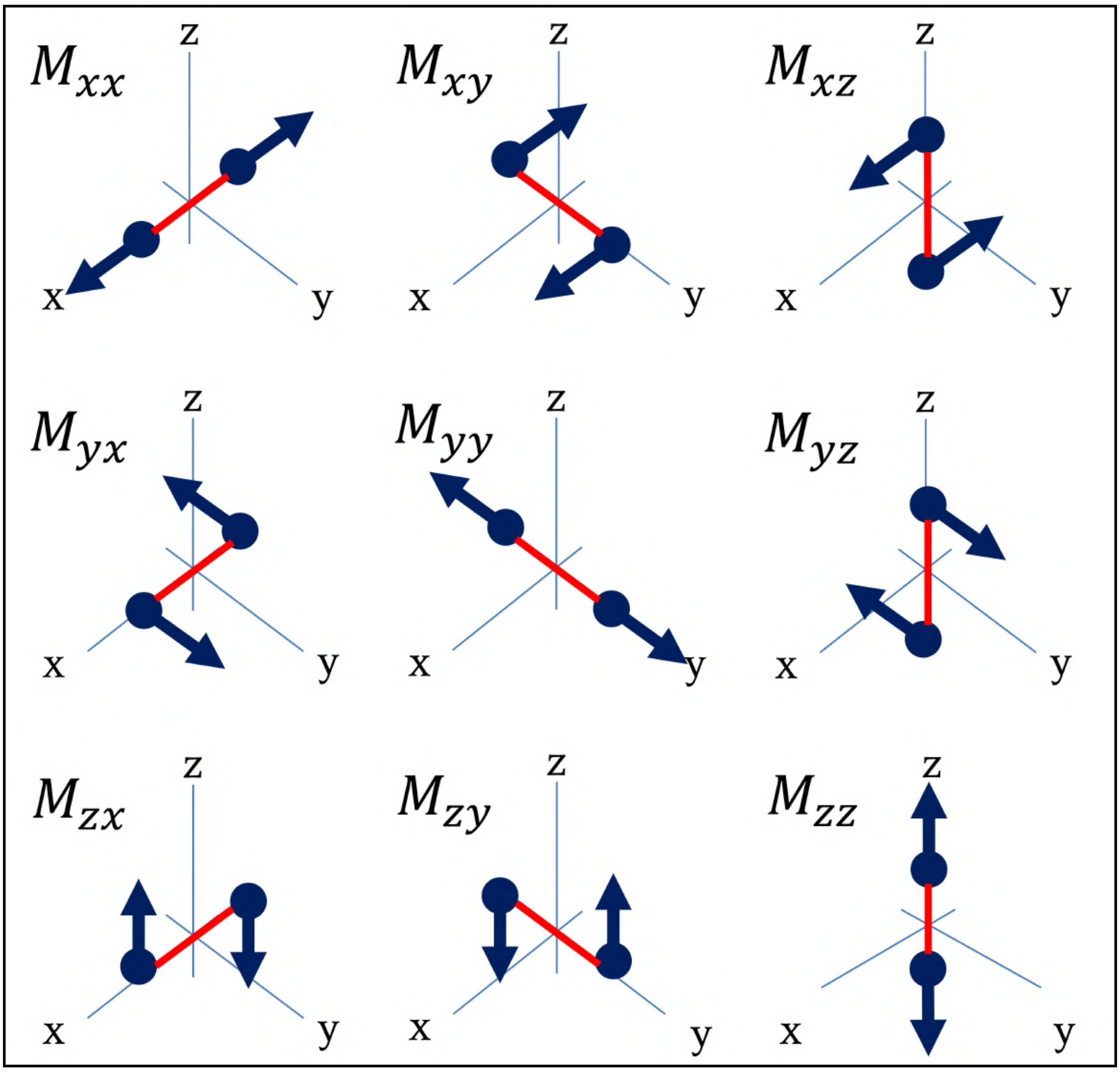

Figure 3-4: Schematic representation of the nine generalized force couples that make up the seismic moment tensor in Cartesian coordinate system. Adopted from Aki and Richards [2002]

Due to the conservation of angular momentum, only six of the tensor elements are independent in any coordinate system, and the tensor is symmetric, i.e $M_{ij} = M_{ji}$.

Any two of the independent force couples of the tensor elements can be combined to give the so-called *double-couple*.

3.3.1.1 Isotropic media

The moment tensor for a double-couple seismic source in isotropic medium can be represented as [Aki and Richards, 2002]:

$$M_{ij} = \mu u A \left(\nu_i n_j + \nu_j n_i\right), \tag{3.12}$$

where u is the slip, $\mathbf{v}$ is the slip vector and $\mathbf{n}$ is the fault normal. Due to the symmetry of the moment tensor, vectors $\mathbf{v}$ and $\mathbf{n}$ can be interchanged without affecting the displacement field. This results into a fundamental ambiguity wherein the fault plane and the orthogonal auxiliary plane cannot be uniquely resolved from the radiation pattern of a point source. Instead, two mutually orthogonal nodal planes can be determined, one of which is the true fault plane.

3.3.1.2 Anisotropic media

For a seismic source in anisotropic media, the relation between the source and the moment tensor can be expressed as [Aki and Richards, 2002]:

$$M_{ij} = c_{ijkl} D_{kl}, \tag{3.13}$$

where $\mathbf{c}$ is the tensor of elastic parameters of the rocks surrounding the fault, commonly called the stiffness tensor, and $\mathbf{D}$ is the potency tensor given by Equation 3.14,

$$D_{kl} = \frac{uA}{2} \left(\nu_i n_j + \nu_j n_i\right). \tag{3.14}$$

3.3.1.3 Moment tensor decomposition

The moment tensor can be diagonalized and decomposed into three focal mechanisms describing different rock failures at the source i.e, isotropic (ISO), double couple (DC) and compensated linear vector dipole (CLVD), as shown in Equation 3.15

[Jost and Herrmann, 1989, Lay and Wallace, 1995, Vavryčuk, 2005]:

$$\mathbf{M} = \mathbf{M}^{ISO} + \mathbf{M}^{DC} + \mathbf{M}^{CLVD} \tag{3.15}$$

Here, the diagonalized moment tensor can be written as:

$$\mathbf{M} = \begin{bmatrix} M_1 & 0 & 0 \\ 0 & M_2 & 0 \\ 0 & 0 & M_3 \end{bmatrix}, \text{where} M_1 \geq M_2 \geq M_3, \tag{3.16}$$

and the decomposed components as:

$$\mathbf{M}^{ISO} = \frac{1}{3} \begin{bmatrix} tr(M) & 0 & 0 \\ 0 & tr(M) & 0 \\ 0 & 0 & tr(M) \end{bmatrix}, \tag{3.17}$$

$$\mathbf{M}^{DC} = (1-2\epsilon) \begin{bmatrix} 0 & 0 & 0 \\ 0 & -M_3 & 0 \\ 0 & 0 & -M_3 \end{bmatrix}, \tag{3.18}$$

and

$$\mathbf{M}^{CLVD} = \epsilon \begin{bmatrix} -M_3 & 0 & 0 \\ 0 & -M_3 & 0 \\ 0 & 0 & 2M_3 \end{bmatrix}, \tag{3.19}$$

where $tr(M)$ is the trace of the moment tensor $\mathbf{M}$ given in Equation 3.16.

3.3.2 Focal Mechanism Solutions

Focal mechanism solutions, also commonly known as *Fault plane solutions*, provide graphical visualization of the moment tensor solutions in the form of *beachball* diagrams. This unique representation provides a clear visualization of the fault and the direction of slip from the fault resulting from a seismic event.

From Equation 3.12 and Equation 3.14, with the slip vector $\mathbf{v}$ and fault normal $\mathbf{n}$ on the fault surface, the minimum compressive axis ($\mathbf{t}$), the null axis ($\mathbf{b}$) and the maximum compressive axis ($\mathbf{p}$) can be expressed as [Herrmann, 1975]:

$$t = \frac{1}{\sqrt{2}}\left(n + \nu\right), \tag{3.20}$$

$$b = \left(n \times \nu\right), \tag{3.21}$$

$$p = \frac{1}{\sqrt{2}}\left(n - \nu\right). \tag{3.22}$$

The focal mechanism solutions for the six elementary moment tensors can therefore be represented as shown in Figure 3-5.

Moment tensor	Beachball	Moment tensor	Beachball
$\mathbf{M_1} = \begin{bmatrix} 0 & 1 & 0 \\ 1 & 0 & 0 \\ 0 & 0 & 0 \end{bmatrix}$	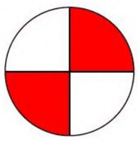	$\mathbf{M_2} = \begin{bmatrix} 1 & 0 & 0 \\ 0 & -1 & 0 \\ 0 & 0 & 0 \end{bmatrix}$	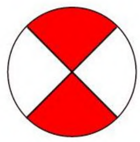
$\mathbf{M_3} = \begin{bmatrix} 0 & 0 & 0 \\ 0 & 0 & 1 \\ 0 & 1 & 0 \end{bmatrix}$	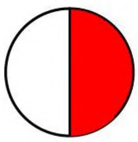	$\mathbf{M_4} = \begin{bmatrix} 0 & 0 & 1 \\ 0 & 0 & 0 \\ 1 & 0 & 0 \end{bmatrix}$	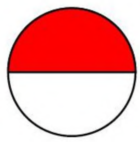
$\mathbf{M_5} = \begin{bmatrix} -1 & 0 & 0 \\ 0 & 0 & 0 \\ 0 & 0 & 1 \end{bmatrix}$	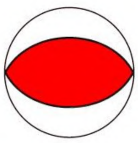	$\mathbf{M_6} = \begin{bmatrix} 1 & 0 & 0 \\ 0 & 1 & 0 \\ 0 & 0 & 1 \end{bmatrix}$	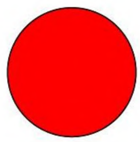

Figure 3-5: Beachball diagrams for the six elementary moment tensors.

In Figure 3-5, $\mathbf{M_1}$ and $\mathbf{M_2}$ denote pure strike-slip faults; $\mathbf{M_3}$ and $\mathbf{M_4}$ denote dip-slip faults on vertical planes; $\mathbf{M_5}$ denotes a 45° dip-slip fault; and $\mathbf{M_6}$ denotes an explosive source. As emphasised by Kikuchi and Kanamori [1991] these elementary moment tensors play a crucial role during full moment tensor inversion.

A DC source mechanism can be represented by the angles of **strike** $\phi\,(0° \leq \phi < 360°)$, **dip** $\delta\,(0° \leq \delta < 360°)$ and **rake** (slip) $\lambda\,(-180° \leq \lambda \leq 180°)$ as illustrated in Figure 3-6.

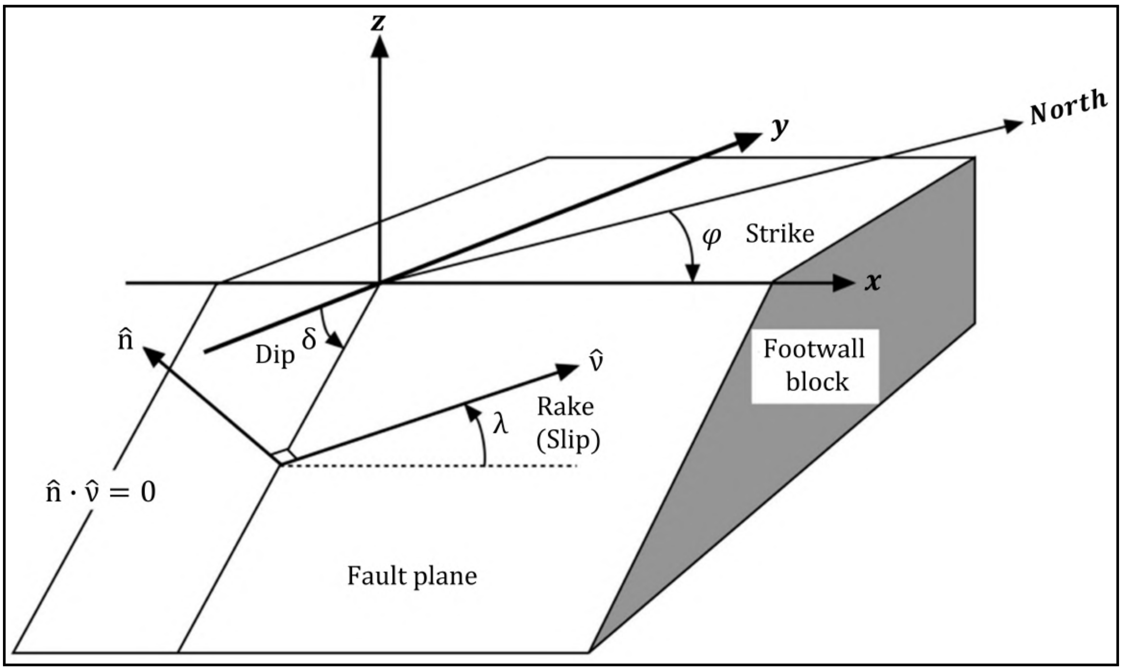

Figure 3-6: Schematic representation of fault geometry commonly used in seismic studies. The fault plane angles of strike, dip and rake are defined as shown on the diagram. Modified after Kanamori and Cipar [1974]

The relationship between these three angles and the six independent moment tensor elements can be formulated as [Aki and Richards, 2002]:

$$\begin{aligned}
M_{xx} &= -M_0\left(\sin\delta\cos\lambda\sin 2\phi + \sin 2\delta\sin\lambda\sin^2\phi\right),\\
M_{yy} &= M_0\left(\sin\delta\cos\lambda\sin 2\phi - \sin 2\delta\sin\lambda\cos^2\phi\right),\\
M_{zz} &= M_0\left(\sin 2\delta\sin\lambda\right),\\
M_{xy} &= M_0\left(\sin\delta\cos\lambda\cos 2\phi + \tfrac{1}{2}\sin 2\delta\sin\lambda\sin 2\phi\right),\\
M_{xz} &= -M_0\left(\cos\delta\cos\lambda\cos\phi + \cos 2\delta\sin\lambda\sin\phi\right),\\
M_{xy} &= -M_0\left(\cos\delta\cos\lambda\sin\phi - \cos 2\delta\sin\lambda\cos\phi\right).
\end{aligned} \tag{3.23}$$

The isotropic moment tensor component (Equation 3.17) represents an explosion or an implosion with a volume change.

The moment tensor for a CLVD (Equation 3.19), represents three force dipoles that are compensated. As the trace (sum of the elements on the main diagonal) of the tensor is zero, the isotropic component does not exist. Unlike the beachball diagrams for double-couple source mechanisms in Figure 3-6, the first motions for CLVDs look like baseballs or eyeballs (Figure 3-7).

Moment tensor	Beachball	Moment tensor	Beachball
$\mathbf{M}_1 = \begin{bmatrix} 1 & 0 & 0 \\ 0 & -2 & 0 \\ 0 & 0 & 1 \end{bmatrix}$	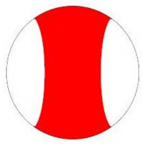	$\mathbf{M}_2 = \begin{bmatrix} -2 & 0 & 0 \\ 0 & 1 & 0 \\ 0 & 0 & 1 \end{bmatrix}$	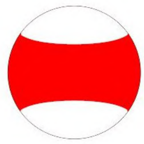
$\mathbf{M}_3 = \begin{bmatrix} 1 & 0 & 0 \\ 0 & 1 & 0 \\ 0 & 0 & -2 \end{bmatrix}$		$\mathbf{M}_4 = \begin{bmatrix} -1 & 0 & 0 \\ 0 & -1 & 0 \\ 0 & 0 & 2 \end{bmatrix}$	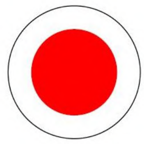

Figure 3-7: Beachball diagrams for CLVD moment tensor components.

Recent studies have documented existence of non-DC focal mechanisms in the case of hydraulic fracturing induced microseismic events [Baig and Urbancic, 2010, Eaton et al., 2014]. Another example, of non-DC source can be obtained by modeling volcanic eruptions. According to Aki and Richards [2002], the inflating magma is analoguous to opening of a crack under tension, and its moment tensor can be expressed as follows:

$$\mathbf{M} = \begin{bmatrix} \lambda & 0 & 0 \\ 0 & \lambda & 0 \\ 0 & 0 & \lambda + 2\mu \end{bmatrix}, \tag{3.24}$$

where λ and μ are Lamés parameters. Because of crack opening, the moment tensor has a positive trace ($3\lambda + 2\mu$). The moment tensor can thus be decomposed as [Stein and Wysession, 2009]:

$$\begin{bmatrix} \lambda & 0 & 0 \\ 0 & \lambda & 0 \\ 0 & 0 & \lambda + 2\mu \end{bmatrix} = \begin{bmatrix} E & 0 & 0 \\ 0 & E & 0 \\ 0 & 0 & E \end{bmatrix} + \begin{bmatrix} -\frac{2}{3}\mu & 0 & 0 \\ 0 & -\frac{2}{3}\mu & 0 \\ 0 & 0 & \frac{4}{3}\mu \end{bmatrix}, \tag{3.25}$$

where $E = \lambda + \frac{2}{3}\mu$ denotes the medium's Young's modulus. In this decomposition, the first term is the ISO component while the second term is the CLVD component. The CLVD could also result from near-simultaneous seismic events on nearby faults with different geometries e.g [Eaton, 2018, Stein and Wysession, 2009]. For instance, consider Equation 3.26 in which two DC sources with moment tensors M_0 and $2M_0$

add up to yield a CLVD.

$$\begin{bmatrix} M_0 & 0 & 0 \\ 0 & 0 & 0 \\ 0 & 0 & -M_0 \end{bmatrix} + \begin{bmatrix} 0 & 0 & 0 \\ 0 & -2M_0 & 0 \\ 0 & 0 & 2M_0 \end{bmatrix} = \begin{bmatrix} M_0 & 0 & 0 \\ 0 & -2M_0 & 0 \\ 0 & 0 & M_0 \end{bmatrix}, \tag{3.26}$$

3.3.3 Moment Tensor Inversion

Different methods for performing moment tensor inversion exist depending on the type of waves and the knowledge of the Green's functions. Suppose the Green's function is known, Equation 3.7 can be written in matrix form (Equation 3.27):

$$\mathbf{u} = \mathbf{Gm} \tag{3.27}$$

where $\mathbf{u}$ is a vector containing n samples of observed ground displacements at receivers (stations), arrival-times and azimuths; $\mathbf{G}$ is an $n \times 6$ matrix of Green's functions and $\mathbf{m}$ is a vector containing the 6 independent elements of the moment tensor. The task in Equation 3.27 is thus to compute $\mathbf{m}$ since $\mathbf{u}$ can be obtained from the recorded seismic waveforms. Equation 3.27 can thus be written in expanded form as follows:

$$\begin{bmatrix} u_1 \\ u_2 \\ \vdots \\ u_n \end{bmatrix} = \begin{bmatrix} G_11 & G_12 & G_13 & G_14 & G_15 & G_16 \\ \vdots & \vdots & \vdots & \vdots & \vdots & \vdots \\ \vdots & \vdots & \vdots & \vdots & \vdots & \vdots \\ G_n1 & G_n2 & G_n3 & G_n4 & G_n5 & G_n6 \end{bmatrix} \begin{bmatrix} m_1 \\ \vdots \\ \vdots \\ m_n \end{bmatrix}. \tag{3.28}$$

Equation 3.28 is clearly over-determined as there are more (linear) equations (n) than unknowns (six). It is therefore not possible to directly invert $\mathbf{G}$ since it is not square. A least squares inversion can therefore be performed to compute the best matching elements for $\mathbf{m}$. The problem is thus formulated as follows:

$$m = \left(G^T G\right)^{-1} G^T u. \tag{3.29}$$

Determination of the full moment tensor of microseismic events can however be a daunting task due to the usually low SNR and may consequently impose certain constraints for inversion at reservoir scale. Nonetheless, inversion techniques have been developed devoted the low-magnitude microseismic events e.g [Shutian and Eaton, 2009, Eaton, 2018], that adjustment of the arrival times and the uncertainty in the velocity model. Deep learning approaches have also been developed that do not rely on the arrival time picks but rather a consistent and accurate forward modeling as discussed in section 3.2 and section 3.5 and implemented in chapter 4.

3.4 Distributed acoustic sensing (DAS)

3.4.1 Principle of DAS Measurements

DAS employs Rayleigh backscattering (RBS) technology to measure and locate the vibrations along an optical fiber cable. Short pulses of high coherent light are transmitted along an optical fibre cable. The back-scatted signals are then detected. Vibrations in the proximity of the fiber optic cable trigger the scattering sites in the fiber. Consequently, there is a modification to the Rayleigh backscattered laser signal. The signals are then analysed as acoustic signals. The DAS is capable of measuring the amplitude, frequency and phase along the entire distance of a fibre optic cable up to approximately 100km [He and Liu, 2021]. The photoelastic effect is primary to the measuring principle of the DAS. The Photoelastic impact changes the refractive index caused by stress, where there is a linear relationship between the optical phase change and the axial strain. The DAS operates by inducing laser pulses into the fibre-optic and generates a Rayleigh scattering along with the fibre. In principle, a section of the generated Rayleigh is propagated in the opposite direction to the pulses. This is known as the Rayleigh backscattering (RBS), which is expressed mathematically as given in Equation (3.30):

$$\Delta\phi = \beta \left[1 - \frac{n^2}{2}\left(P_{12} + 2P_{11}\right)\right] \varepsilon L, \tag{3.30}$$

where β is the light propagation constant, n is the refractive index of the optical fiber, P_{12} and P_{11} are the sensors coefficients of the optical fiber, L is the fiber length, and ε is the axial strain of the fiber.

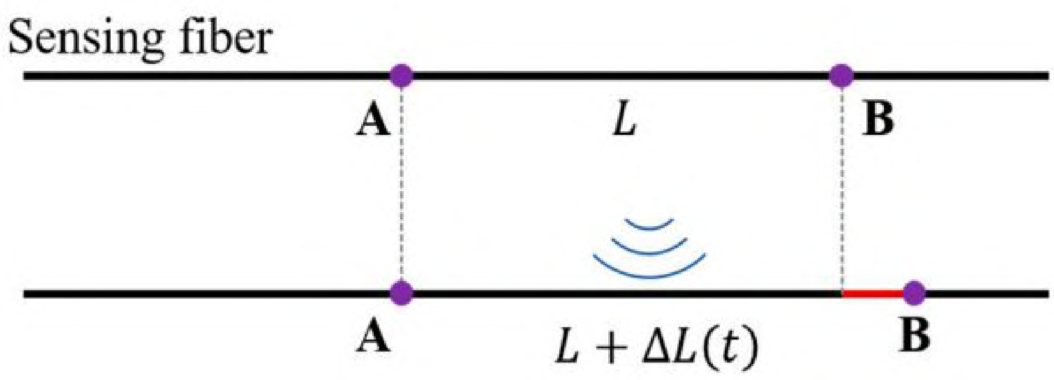

Figure 3-8: The sensing principle of the fiber-optic distributed acoustic sensing system. Source: Sun et al. [2022]

The task of a DAS is to locate the position of the Rayleigh backscattering at a given location along the fiber optic cable. The second task is to obtain vibration signals from the Rayleigh backscattering. The DAS measurement is taken by measuring the changes in the optical phase due to variation in axial strain. This measuring technique is known as the phase-sensitive optical time-domain reflectometry (ϕ - OTDR), which is part of the is the optical time-domain reflectometry (OTDR) group and the most used method currently among the reflectometers. The other reflectometers are the Optical Frequency Domain reflectometry (OFDR) and the Time-gated digital Optical Frequency domain reflectometry (TGD-OFDR). When there is a change between point A and B, the changes in the axial strain is quantitatively computed from the propagated acoustic waves as presented in Figure 3-8.

The OTDR works on the principle of the emission of short laser pulses through a lunch cable into a fibre-optic link. The phase-sensitive optical time domain reflection (ϕ - OTDR) is widely used due to the absence of nonlinear effects and the ability to distinguish via time of reflection. Some of the recent improvements in the performances of OTDR are the implementation of high extinction ratio (ExR) pulses for coherence noise reduction, the implementation of the nonlinear Kerr effect to generate high ExR pulses, the identification of pulse shapes and the employment of optical pulse coding techniques for fast denoising in the optical domain, coherent detection scheme, 3×3 coupler scheme, linear frequency sweep pulse and phase generated carrier. Problems of the OTDR such as low sensitivity of the acoustic measurement, Rayleigh scattering phase fading phenomena and noisy components of the system have been reported in literature [Kishida et al., 2021]. The Optical Frequency Domain Reflectometry (OFDR) can be divided into two subcategories. The incoherent OFDR (I-OFDR) and the coherent OFDR (C-OFDR). The incoherent involves the modulation of a continuous-wave optical carrier by constant amplitude radio frequency signal with a stepwise change in frequency over a certain frequency range [Wegmuller et al., 2000, Von der Weid et al., 1997, Huttner et al., 1998, Lee et al., 2006]. The TGD-OFDR is noted for its improved SNR and high spatial resolution. In addition, the phase variation problem, phase noise from the laser source due to environmental issues, is reduced by increasing the sweeping frequency rate [Wang et al., 2015]. Wang et al. [2015] proposed a novel method of implementation of the TGD-OFDR by both experimental and theoretical derivation. The improved method of vibration measurement based on backscattering phase extraction reported a better sensitivity when compared with other conventional methods. The minimal measurable vibration acceleration is 0.08g. Similarly, a study by Chen et al. [2017] provided a method of solving the fading noise problem in the phase-detection method utilizing fading-noise-free distributed fiber-optic vibration sensors based on TGD-OFDR. Other reported improvements based on the TGD-OFDR method include the upgrades to spatial resolution over an extended measurement range [Liu et al., 2015]. Concerning the oil industry, the DAS is reported to be the third optical fibre applied. The first two systems are the Point Sensors (PS) and the Quasi-Distribute Sensor (QDS). The Point sensors consist of just one sensor located on a fibre for the measurement of temperature and pressure. On the other hand, the Quasi-Distributed sensor had multiple spaced sensors along the fiber optic cable. Meanwhile, the Distributed Sensors can measure and transmit parameters simultaneously.

3.4.2 Advantages of DAS technology

The previous decades have relied on permanent seismic arrays, which were distributed in close populated regions of the world and along seashores to detect seismic activities. These seismic networks require a vast number of seismic stations. It is reported that a country like Japan alone has about 2000 seismic stations. Regardless of the enormous number of seismic stations, the distribution of these stations worldwide is below the required number. Also, most of these stations are located on land. Hence, there is no significant ocean coverage, which presents a biased geospatial sampling of global seismic activities. Furthermore, the maintenance of such stations is very high, which makes it difficult for developing countries to prioritize and invest in such technologies.

The DAS system presents a solution to the problems associated with the traditional system. The conventional monitoring devices require distributing monitoring systems a few kilometres apart in specific areas to detect a single seismic event. On the other hand, the DAS system only requires sampling along a few meters to locate seismic activities. Therefore, it produces a high amount of spatial sampled data. The information presented by the DAS system enables efficient investigation. It presents new knowledge in the analyses, interpretation and monitoring of seismic activities. In addition, the DAS system has been reported to have a longer life span and present an overall low-cost estimation in the monitoring of seismic activities along several meters. The DAS system is reported to be used in harsh conditions. It provides safety to the monitoring crew due to the ability to utilize remote sensing. The investigation can be conducted remotely to ensure safety by placing the DAS system in extreme situations. These harsh conditions include seabed monitoring and challenging to reach terrain. In addition, the DAS system requires low maintenance and has less risk of damage easily.

3.4.3 Challenges of DAS technology

The DAS system has increasingly replaced other conventional systems. This is because it offers the possibility of high density arrays and full-length coverage of measurements. However, there are some challenges associated with the DAS system. One of these is that, compared to a 3D component geophone, the DAS system only provides seismic information in one component and excludes the azimuth information. However, this directivity issue can be partially resolved by utilizing helically wound cables [Kuvshinov, 2015]. A. [2020] modelled DAS response of the helically wound cables for microseismic applications.

Williams et al. [2017] present an estimation of this limitation by a finite different modelling method to generate one-dimensional synthetic seismic data. The arrival times of the P-wave or P-wave were detected by the DAS system and component measurements of a 3C geophone. This study observed that by using a simple model, the P-waves or P-waves and S-waves arrivals along linear arrays could be effectively used to detect the location by the DAS system without any additional information. Similarly, Williams et al. [2017] observed that straight cables were less effective as compared to deviated lines for both P and S wave detection. The study concluded by outlining the trade-off between the 3C geophone and the DAS system.

Also, the application of the DAS system to measure chirped-pulse currently has significant limitations. The chirped-pulse has been performed on only temperature variations with high errors. The errors are due to the low-frequency noise associated with the measurements [Wang et al., 2022]. Unfortunately, there are no proposed methods to overcome this problem.

3.4.4 Intelligent Processing of DAS data

Data in this generation is regarded as one of the most priced assets. Different organizations are interested in collecting data on various activities. This trend is partly due to the increase in technologies that allow huge data storage volumes. Also, the inception of artificial intelligence (AI) has significantly reduced the labour involved in the data processing. The high computing performance of the machine has also improved over the year. The combination of all these innovations has been adopted in all industries. The DAS technology is also a beneficiary of this innovative, intelligent system. The DAS system provides a vast volume of information from its measurements. Such high volumes of information make it possible for the accurate characterization, interpretation, and quantification of the observed seismic events. However, such high volumes of data require high labour for its processing and interpretation. To overcome this problem, most researchers have utilized the emerging importance of the AI system for the real-time processing of data obtained from the

DAS system providing accurate interpretations.

Data obtained from the DAS technology goes through a series of stages before information, and relevant interpretations can be made. Among them are the training stage and the classification stage. Different machine learning techniques have been utilized for different DAS feature identifications. Some applied machine learning models include Neural networks, Gaussian Mixture Modelling, Support vector machines, k-nearest neighbours, Fuzzy logic, etc. These intelligent methods have also detected different characteristics or features: the PSD wavelet, the FFT-based, the PSD-PCA, and many more. The features can be divided into three main categories: the time domain feature, the frequency domain feature, and the time-frequency domain features. The time frequency is reported to be suitable for stationary signals. At the same time, the frequency and the time-based features are suitable for non-stationary signals [Tejedor et al., 2017].

Bublin [2019] presented a comparison between the classic imaging method and the deep neural networks approach for the detection of seismic events. Bublin [2019] concluded that, although both methods could produce relatively good results, the deep learning is faster and present six times lower event detection delay and twelve times lower execution time. [Shiloh et al., 2019] presented a similar conclusion of significant improvement in the results given by the generative adversarial net (GAN) methodology.

Wu et al. [2021] emphasized that the combination of both the manual and the AI systems improved the identification capabilities of the DAS as compared to only the manual or the synthetic methods. From this study, the combination of both methods improved the computational efficiency by up to 90% at performance degradation below 1%. Peng et al. [2019b] present a supervised machine learning and unsupervised machine learning method based on interpreting the results of optical time-domain reflectometry (ϕ-OTDR). The implemented machine learning model provides about 90% accuracy in detecting human movements. Furthermore, data pattern recognition was also observed in the work of Peng et al. [2019a] when AI was used in processing a DAS system built by phase-sensitive optical time-domain reflectometry (ϕ-OTDR) with Rayleigh enhancement.

The disadvantage of signal to noise ratio of the DAS system was investigated by [Zhao et al., 2021] utilizing an artificially intelligent system. The proposal based on a denoising CNN method effectively suppressed different noise in the DAS data. Moreover, the effective signals have significantly low energy attenuation. DAS and intelligent systems have also studied the detection of earthquakes. Hernández et al. [2022] provided an assessment of the ability of a deep learning model (CNN) trained with actual seismic data could accurately predict earthquakes from DAS data. The study showed that the CNN model could reach an accuracy of 96.9% in predicting earthquakes and providing early warning signs. Data from low-frequency distributed acoustic sensing (LFDAS) signals were used to train a model to predict the fracture hit in wells during a hydraulic fracturing operation [Jin et al., 2019]. The study concluded that the model predictions agree well with manual picks in the training, validation and test data sets.

3.4.5 Future of DAS

The DAS technology is a relatively new technology that has gained a wide range of applications in geophysics and has become the principal technology for the acquisition of seismic data. While there are many adaptations and utilization of the DAS system currently, there is still a significant range of applications where the DAS system could be employed in the future. For example, in the world of climate change, the changes to the earth's seismic activities could be equally impacted. Hence, monitoring such activities could benefit immensely from the DAS system. Among these activities are monitoring volcanoes, changes in the arctic ice caps, monitoring of seismic activities in less seismic active regions, and mapping the seabeds across the globe. The ability of the DAS system to present enough data could help make predictions about possible environmental changes due to climate change. The most important aspect is that these could be done at a relatively low cost and could help prevent major earthquakes.

Fernández-Ruiz et al. [2020b] emphasized that the DAS system could be employed to monitor the glacier seismology under harsh conditions. The DAS is an excellent candidate to provide a dense array of data in such an environment without constant maintenance and human interference. Also, there are suggestions for applying the DAS system to explore other cosmic bodies. Past cosmic exploration has utilized DAS systems on a mission for different purposes [Fernández-Ruiz et al., 2020a]. However, the exploration of the geological makeup of other planets remains the frontier of space exploration. The DAS system is a perfect fit for such geological investigation and possible geoengineering of other cosmic bodies like Mars in the future.

3.5 Convolutional neural networks (CNNs)

CNNs [LeCun et al., 2015] operate by shifting small filters (kernels) around the input matrix. This implies that the kernels are recycled in the entire image to detect patterns. In essence, it speeds up training for the CNNs. The principal building block for CNNs is the convolutional layer, which processes a series of learnable filters to convolve three-dimensional input data (breadth, height, and depth). In general, the size of any filter in width and height is small but covers the entire input data depth. For instance, suppose the input data has a depth of 3, like in our case, a standard filter would have dimensions $5 \times 5 \times 3$, where the first two dimensions represent the height and width of the filter. The filter moves along the surface of the input matrix calculating the inner product at every point, while performing convolution. The result is a two-dimensional activation map, which comprises of the filter response at each location. Thus, the number of activation maps in a given layer equal that of filters within the same layer. In order to generate output data for input in next step, the activation maps are then stacked along the depth axis. Every neuron in a convolution layer is input as it were from its receptive field in the previous layer, i.e., the output at any time depends only on the input information height and breadth. This substantially diminishes the number of free parameters making the CNNs to be able to handle a large amount of input data such as in our case.

Downsampling is performed within a pooling layer immediately after the convolution operation in order to diminish the size of the data and reduce the number of calculations to avoid overfitting. The pooling is carried out autonomously along the depth cross-section of the input matrix after which the resulting feature maps are input into activation functions, like the Rectified Linear Unit, commonly referred to as *ReLU* and defined as $f(x) = max(x, 0)$, [Dahl et al., 2013], which then perform non-linear transformations. Without non-linear activation functions, the neural network would not be able to learn non-linear features and thus would be rendered linear predictor. The fully connected layer, which follows the series of convolutions and pooling layers, performs the 'high-level reasoning' for the network. The last layer in the network determines the penalty on the errors between actual and the calculated values for the regression problem.

3.5.1 Theoretical framework of CNN

In order to directly invert event locations and velocity models from raw microseismic data, the neural network should be able to project the input data from data domain (x, t) to the model domain (x, z) as demonstrated in Figure 3-9.

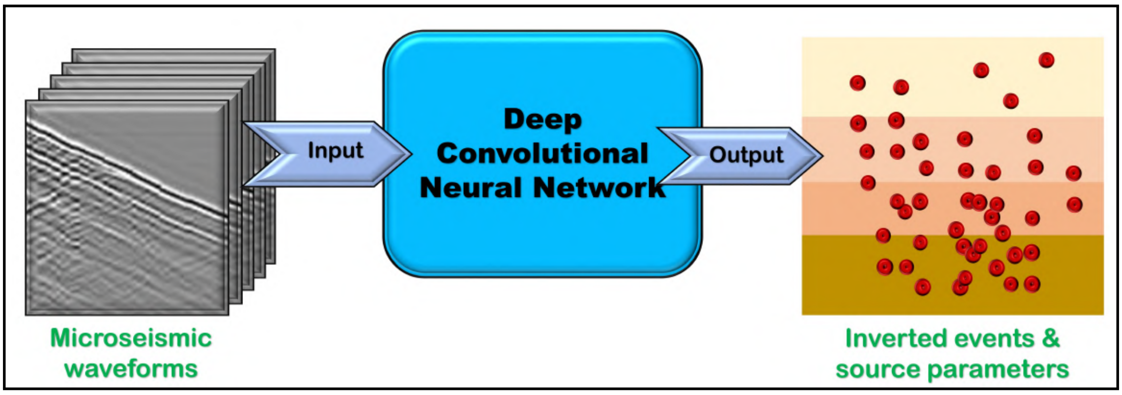

Figure 3-9: Schematic representation of inversion of microseismic events and source parameters from raw microseismic data using convolutional neural network.Adopted from [Wamriew et al., 2021b]

CNNs accomplish this task by establishing invaluable links between the input data and the output parameters. This can be expressed mathematically using the relation:

$$\tilde{m} = Net(d; \Theta), \tag{3.31}$$

where the predictions $\tilde{m} \equiv [\xi_{\mathbf{p}}; \mathbf{v}]$ includes the predicted event locations, $\xi_{\mathbf{p}} \equiv [x_p, y_p, z_p]$ and velocity model values, $\mathbf{v} \equiv [v_p, v_s, \rho]$ at the event locations, while d is the raw microseismic data. This approach comprises of two primary processes namely; *training process* – during which the network learns to associate key features from the input data to the outputs, and *prediction process* – when the network takes as input the test dataset and outputs parameters it associates with it. These two vital processes are illustrated in Figure 3-10.

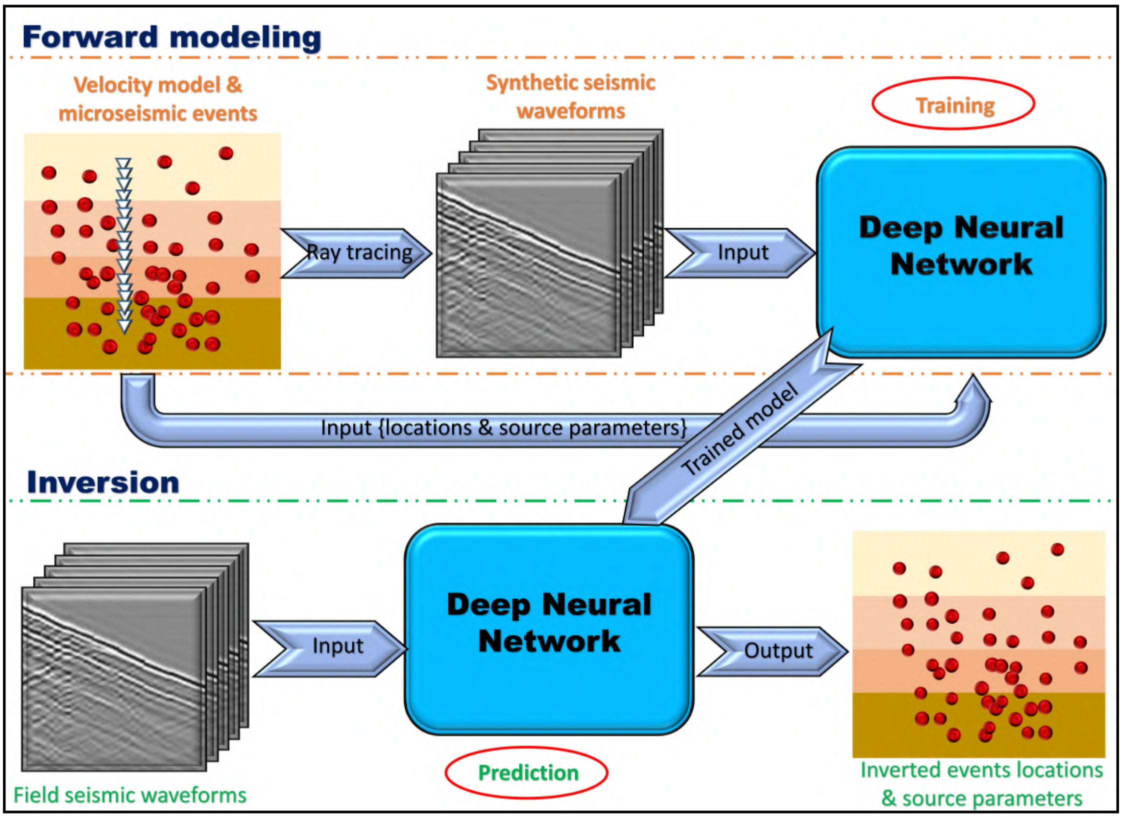

Figure 3-10: Flow chart depicting CNN-based microseismic events location and velocity model update network. The processes of training and prediction are highlighted and linked with the arrows. Red dots represent microseismic events. Modified after [Wamriew et al., 2021b]

Prior to training, forward modeling is performed to generate a lot of microseismic events and velocity models that are then used to compute synthetic seismic data (seismograms) for use in the neural network. Since the network requires two sets of datasets for input and output, the seismograms are used as the input while the velocity models and the event locations as outputs. During training, the network learns to associate the properties of the input dataset to the corresponding outputs (labels) by minimizing the mean squared error(MSE) loss function, which is a function of Θ. The optimization problem can be written as:

$$\hat{\Theta} = \arg\min_{\Theta} \frac{1}{N} \sum_{i=1}^{N} L(m_i, \tilde{m}_i), \tag{3.32}$$

where Θ indicates all the weights in the network, and L is the mean squared error loss function which calculates the disparity between the ground-truth values m_i and the predicted values $\tilde{m}_i$.

Throughout this research, the Adam algorithm [Kingma and Ba, 2014] was used to train the neural networks due to its adaptability. It uses estimates of the first and second moments of the gradients to compute individual adaptive learning rates for different parameters. Due to the huge amount of the training data and limited computer memory, it is not feasible to compute the gradient on the full range of data. For this reason, data was fed into the network in mini-batches of size h in order to compute the disparity, L_h, between the predicted and the ground-truth values in every iteration as a subset of the entire training dataset. The choice of h alongside other hyperparameters is achieved using trial and improvement or by Bayesian optimization. The later is suitable in cases of very deep networks while the former can be adopted in the case of shallow networks where training takes a few minutes or seconds. Consequently, the optimization task can be formulated using Equation 3.33 as follows:

$$\hat{\Theta} = \arg\min_{\Theta} \frac{1}{h} L_h = \arg\min_{\Theta} \frac{1}{h} \sum_{i=1}^{h} \|m_i - Net(d_i, \Theta)\|_2^2 . \tag{3.33}$$

Here the velocity models and the true locations are provided during the training and validation phases but are invisible to the network during testing. Using Adam algorithm [Kingma and Ba, 2014], the parameters of the network can be updated as follows:

$$\Theta_{t+1} = \Theta_t - \alpha \frac{\hat{M}_t}{\sqrt{\mu_t} + \epsilon}, \tag{3.34}$$

where M and μ are the corrected bias estimators for the first and second moments respectively, while α is the learning rate (step size) and ϵ is chosen so small to avoid division by zero. This approximation is straightforward to implement, effective in computation, and perfect for problems with huge amounts of data and parameters to be learned like in our case.

3.6 Data processing for deep learning

One of the many benefits of using deep learning for seismic/microseismic data analysis and interpretation is that it requires minimal data processing as the deep neural network algorithms are capable of extracting, by themselves, the outstanding features from the presented data. The aims of data processing for deep learning models is therefore two folds:

1. to improve SNR while maintaining data integrity,
2. to make the data presentable to the neural network.

The main stages of data processing are therefore: *filtering*, *downsampling* and *conversion to suitable input format for the neural network.* Filtering is done to attenuate the noise and improve SNR. There are two unique types of noise that in addition to cultural noise characterize DAS data. These are the *common-mode noise* and *fading.* The common-mode noise is caused by acoustic vibrations from the vicinity of the IU being registered across all channels of DAS records. It appears as horizontal stripes when the data is plotted with time in the vertical axis, as shown in Figure 3-11.

To remove the common-mode noise, an estimate of the noise can be determined by stacking together all the traces in the record. This will cancel out the actual seismic signal, leaving behind the common-mode noise. The resulting stacked trace is normalized by the number of traces in the record and then subtracted from each trace in the record in order to obtain the denoised record. This is equivalent to passing the entire traces through a 2-D median filter.

Fading occurs when low intensity backscattered light arrives back at the IU. The low intensity arises from the interaction of the backscattered light created from the distribution of random scattering sites in the fiber [Li et al., 2022b]. This results into large amplitude spikes when the intensity is converted to strain/strain-rate. It

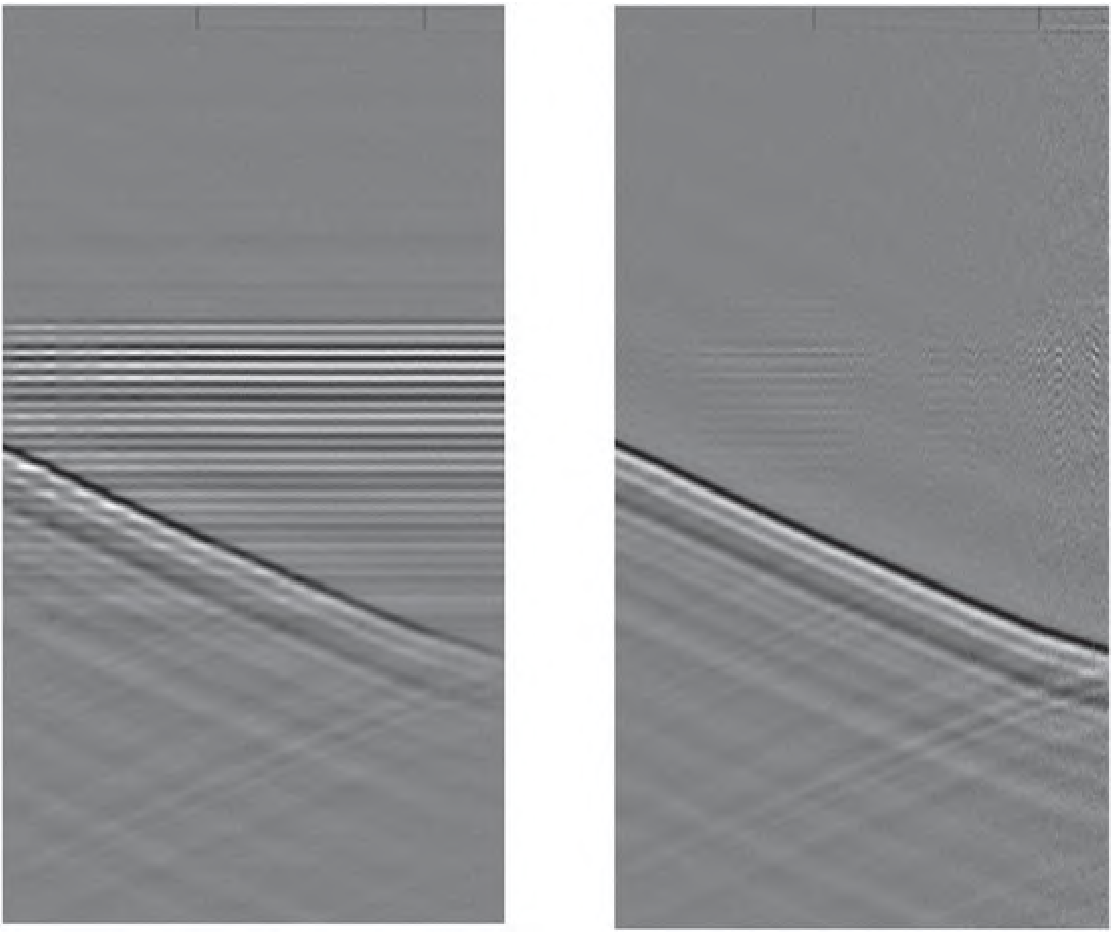

Figure 3-11: (Left) DAS record of strain rate showing common-mode noise; (right) same record after removal of the common-mode noise. Source: Li et al. [2022b]

appears as a vertical stripes on specific channels when the data is plotted with time on the vertical axis.

Fading can be mitigated during data acquisition. Where possible, data can be acquired by several sweeps followed by a weighted stacking of the sweeps to remove the large amplitude spikes. Alternatively, or in addition to weighted stacking, two or more different frequencies of light could be used to acquire the data simultaneously. This will make the locations of the fadings to be different because of the disparate frequency sensitivity of light to the scattering points in the fiber cable [Li et al., 2022b]. The choice of filter is largely dependent on the outlook of data and the signal of interest.

Downsampling can be done both in space and time to reduce the volume of the data considerably and increase SNR while care is taken to preserve the spatial and temporal resolution.

The final stage in data processing for deep learning, as tated, involves conversion of the data records to a suitable input format for the deep learning algorithm to be used in the inversion. This could be an image or a tensor of extracted features of interest.

"if we knew what it was we were doing, it would not be called research, would it?"

Albert Einstein

Chapter 4

Case Studies

In this chapter, we propose and implement algorithm for processing passive seismic data using deep learning. The algorithm is computational efficient and easy to implement. We demonstrate its implementation for processing DAS acquired data but also show its application to conventional geophone data for source mechanism inversion.

4.1 Data Processing workflows

The goal of microseismic data processing is to transform continuous wavefield records into precise and accurate estimates of event locations, magnitudes and other source characteristics.

4.1.1 Conventional workflow

The conventional workflow for processing downhole microseismic data comprises of two parallel workflows, namely: ***primary workflow*** and ***secondary workflow*** as shown in Figure 4-1.

In the primary workflow, the waveform data is processed to produce event catalogue; whereas the secondary workflow is used to estimate the sensor orientations as well as construction and validation of a calibrated background model. The workflow consists of four input data components: **Raw waveform data** - covering one or several time windows during the acquisition process; **Survey data** - containing

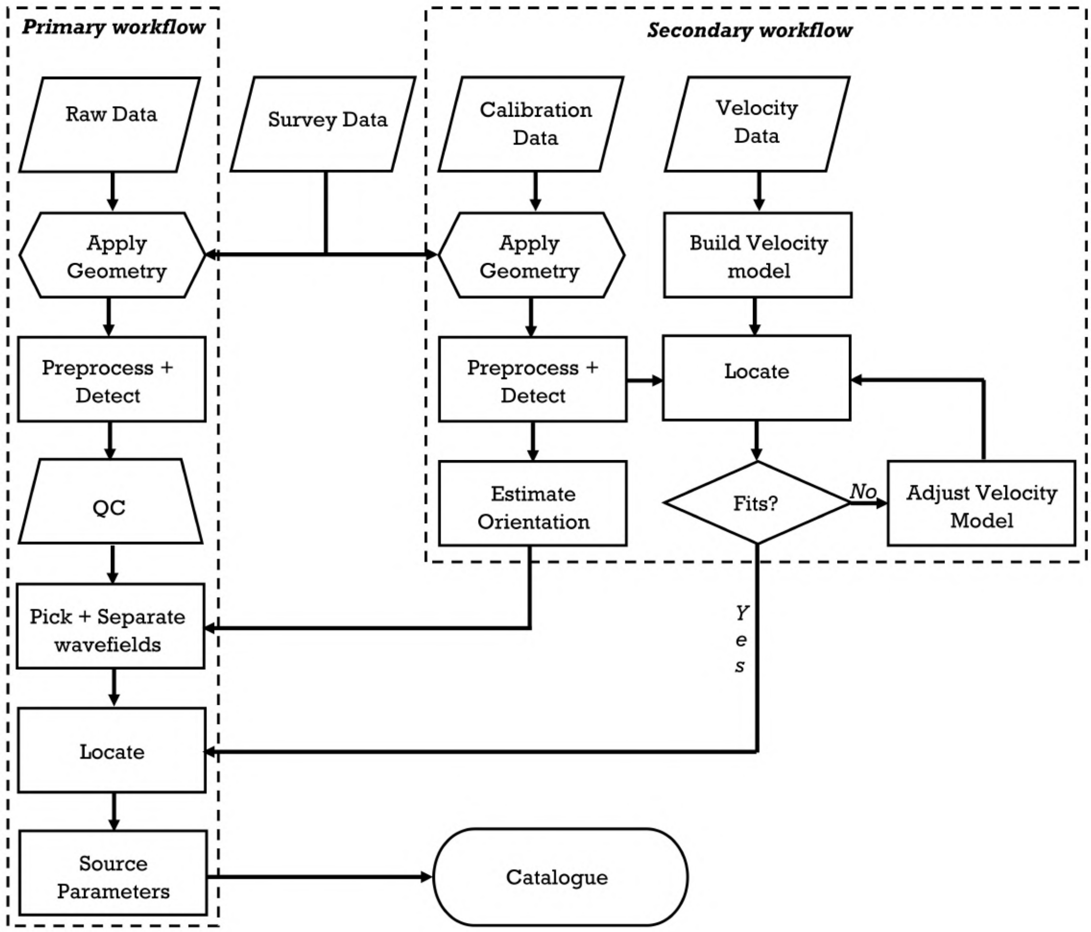

Figure 4-1: Conventional algorithm for processing borehole passive seismic data. Modified from [Eaton, 2018].

information about the positions of the sensors as well as those of treatment and observation wells; **Calibration data** - which is a subset of raw data; **Velocity data** - containing information about the well logs and or other sources of information for the background medium.

To generate a series of event files, the pre-processing steps entail transforming field coordinates into a fixed geographic reference frame, noise attenuation, event detection, phase picking, and rotation into ray-centered coordinates.

A calibrated background model should be built alongside the primary processing workflow. In that instance, approaches like template matching or FAST can be used to detect weak events with low SNR ratios that would otherwise be missed. Alternatively, automated approaches for determining relative hypocenter positions that are connected to independently obtained absolute locations of template events can be applied.

4.1.2 Deep learning based workflow

As evident, the conventional data process algorithm involves a lot of data handling which slows down the process and introduces uncertainty at every stage leading to, in some cases, inconsistent results. Yet in the case of real-time processing, often required during hydraulic fracturing operations, greater emphasis is put on computational efficiency in order to achieve sufficiently fast turnaround in each step. The conventional algorithm then suffers greatly. We thus propose the deep learning approach which takes as input the four data components, performs inversion and outputs the event locations, the updated velocity model and the source parameters all in one go. The deep learning based algorithm is fast, efficient, accurate and capable of dealing with the large streams of data in real-time. The algorithm is presented in Figure 4-2 and is implemented in the following sections.

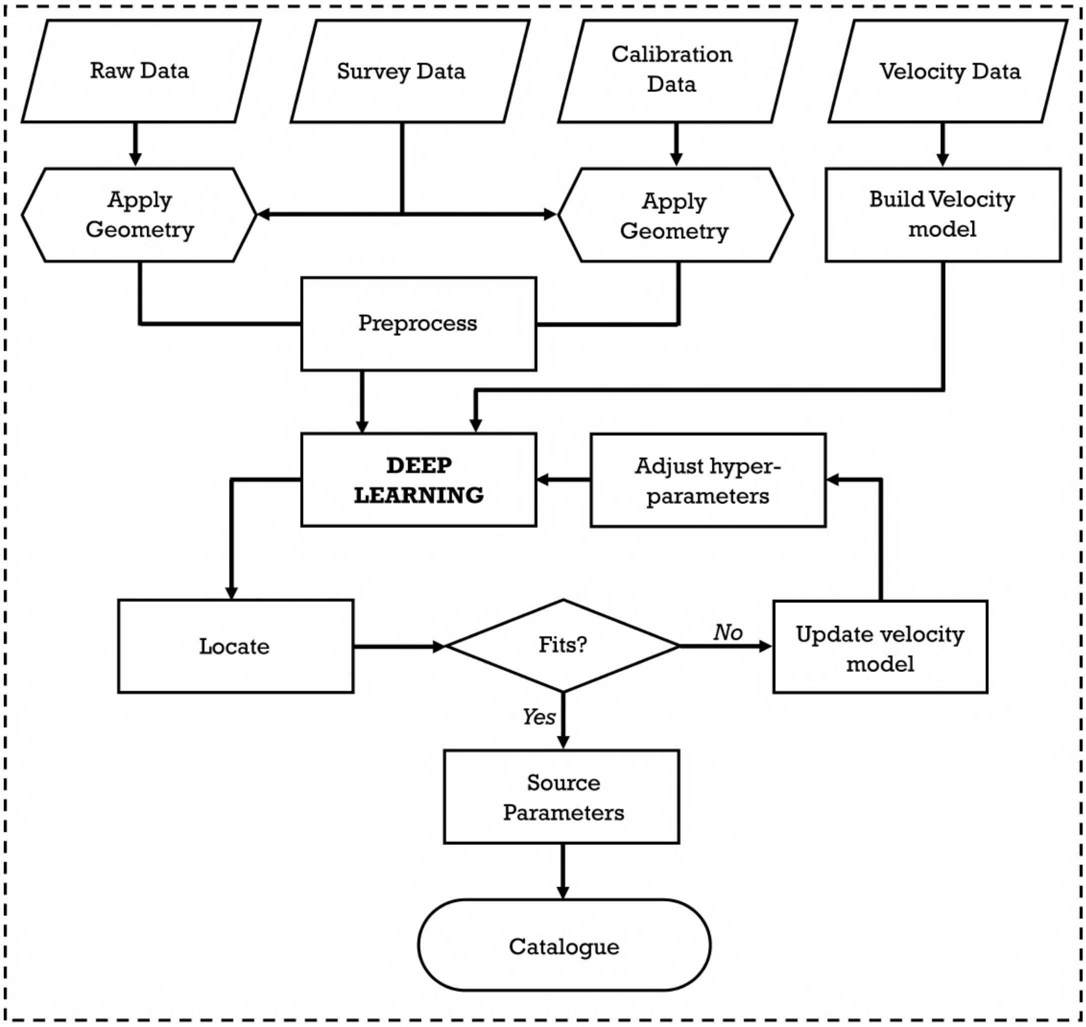

Figure 4-2: Deep learning based algorithm for processing borehole passive seismic data.

Part of the work presented in the following sections have been published in peer-reviewed journals during the course of this research.

4.2 Location and velocity model inversion in real-time

The work in this section has been published in the *Computers and Geosciences* journal [https://doi.org/10.1016/j.cageo.2021.104965].

Title: Joint event location and velocity model update in real-time for downhole microseismic monitoring: A deep learning approach.

Coauthors: Marwan Charara and Dimitri Pissarenko.

4.2.1 Abstract

We demonstrate the application of deep learning to real-time inversion of downhole microseismic data recorded by 3-C geophone sensors. We use synthetic data generated by dynamic ray-tracing and contaminated with both random and coherent noise to match as close as possible field data. Both the tasks of location of microseismic events and velocity model update are considered to be multi-dimensional and non-linear regression problems. Consequently, a two-dimensional (2-D) convolutional neural network is then constructed and it's hyperparameters tuned using Bayesian optimization. The CNN is then trained, validated and tested using data with different levels of SNR. Results indicate that the neural network is capable of learning the relationship between the microseismic waveform data and the event locations and reconstruct the velocity model in real-time to a high degree of precision as the errors in the inversion are less than a few percent.

4.2.2 Forward Modeling

Microseismic data are records of earth particle movements and, as such, the quantitative analysis of these movements can be evaluated by the principle of linear elasticity (Equation 3.6), which defines the basis and provides the context for the discussion of modeling, processing and inversion of microseismic data. The decision on the appropriate numerical method to use for forward modeling of microseismic events depends heavily on its accuracy and computational effectiveness, i.e, its ability to generate a large number of synthetic seismograms within a reasonably short time so as to be able to create a training dataset for the neural network. In forward modelling, we solve a well-poised forward problem by calculating the seismic response for a specified model whose elastic parameters are predefined.

4.2.2.1 Model set-up

In generating the velocity models, we considered horizontally layered earth with known boundary depths. Such models represent the vast majority of geological structures of shale, usually encountered in microseismic monitoring. We generated 500 randomly sampled velocity models with varying number of distinct layers between 4 and 12. Figure 4-3 shows sample velocity models generated and used in the study. Each layer's P- and S-wave velocity values were in the ranges 3830 $ms^{-1} \leq v_{p0} \leq 5059\ ms^{-1}$ and 2193 $ms^{-1} \leq v_{s0} \leq 3187\ ms^{-1}$, respectively, while the layers densities were in the range 2466 $kgm^{-3} \leq \rho \leq$2711 kgm^{-3}. These ranges represent the majority of velocity structure of shale. Both the velocities and densities varied with depth as shown in Figure 4-3. The top and bottom boundary depths of the layers were however fixed at 1500 m and 2000 m respectively.

Each velocity model was considered to be a cube with dimensions x $\times$ y $\times$ z $=$ 501 $\times$ 501$\times$ 501 grid points and increments of $\delta x = \delta y = \delta z = 5m$. The acquisition geometry comprised of a downhole array of 24 3-C receivers spaced equally at intervals of 20 m from a depth of 1505 m downwards in a vertical monitoring well set at the center of the model as shown in Figure 4-4.

This geometry was maintained for all the models. For each velocity model, we created 200 microseismic events randomly distributed within the cube. Such arrangement allows for uniform sampling of the events throughout the box and is suitable for creating training data for a neural network because it represents the full range of possible events in the given geological structure. The large number of sources is necessary for two reasons: the more the events the better the representation of every section of the cube and second, neural network requires large amounts of data for training and validation.

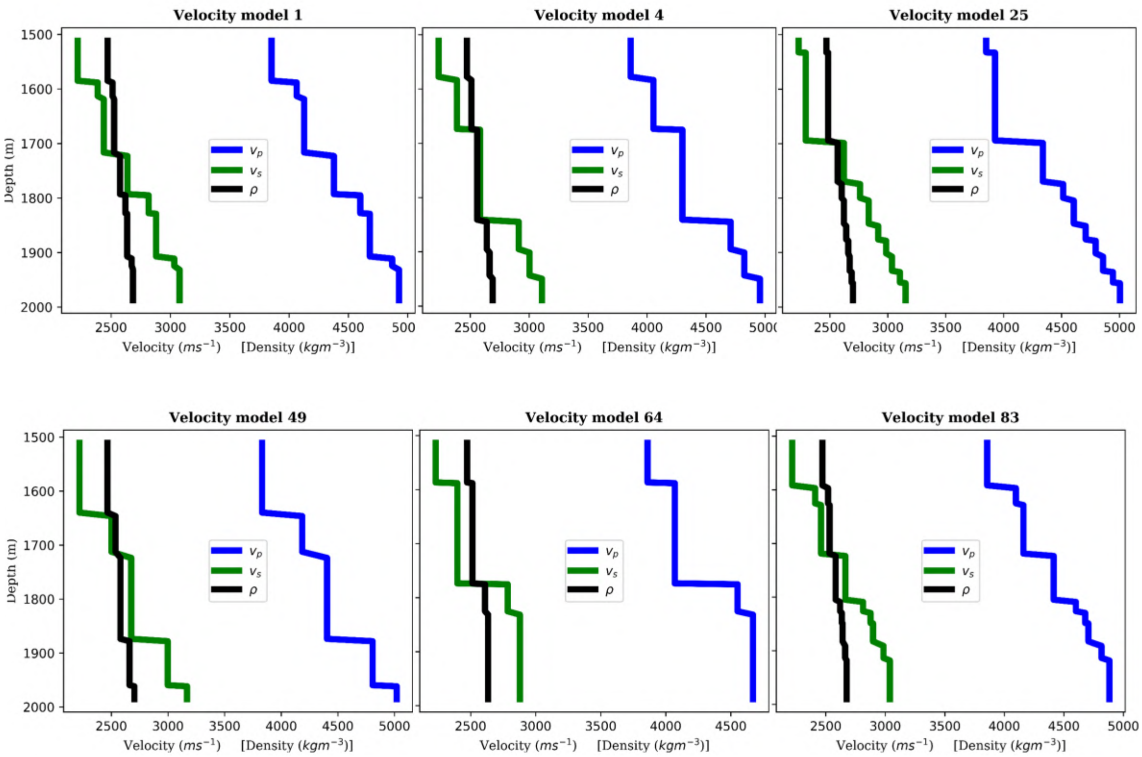

Figure 4-3: Sample velocity parameters for various models considered. The number of layers vary between 4 and 11. Blue and green curves represent P- and S-wave velocities in each layer while black represents the layer density.

4.2.2.2 Ray tracing and synthetic data

Ray tracing has over the years proven to be a very useful tool for approximation of high-frequency elastic waves and is continually applied to forward and inverse modelling problems in seismic exploration and has been used extensively in microseismic inversions, for example [Grechka et al., 2016, Akram et al., 2017, Yaskevich et al., 2019, Wang et al., 2020]. The main reason for its popularity is its versatility (i.e its applicability to a variety of media of different complexities) and numerical efficiency. When applied to smoothly varying layered media, it is capable of providing handy approximate solution to adequate levels of accuracy. The main drawback of ray tracing is that, since it is an approximate solution to the wave equation, it is only effective in smooth media and can give inaccurate results or even fail in singular regions [Červený and Pšenčík, 2011].

Dynamic ray-tracing was used to compute the amplitudes and travel times of

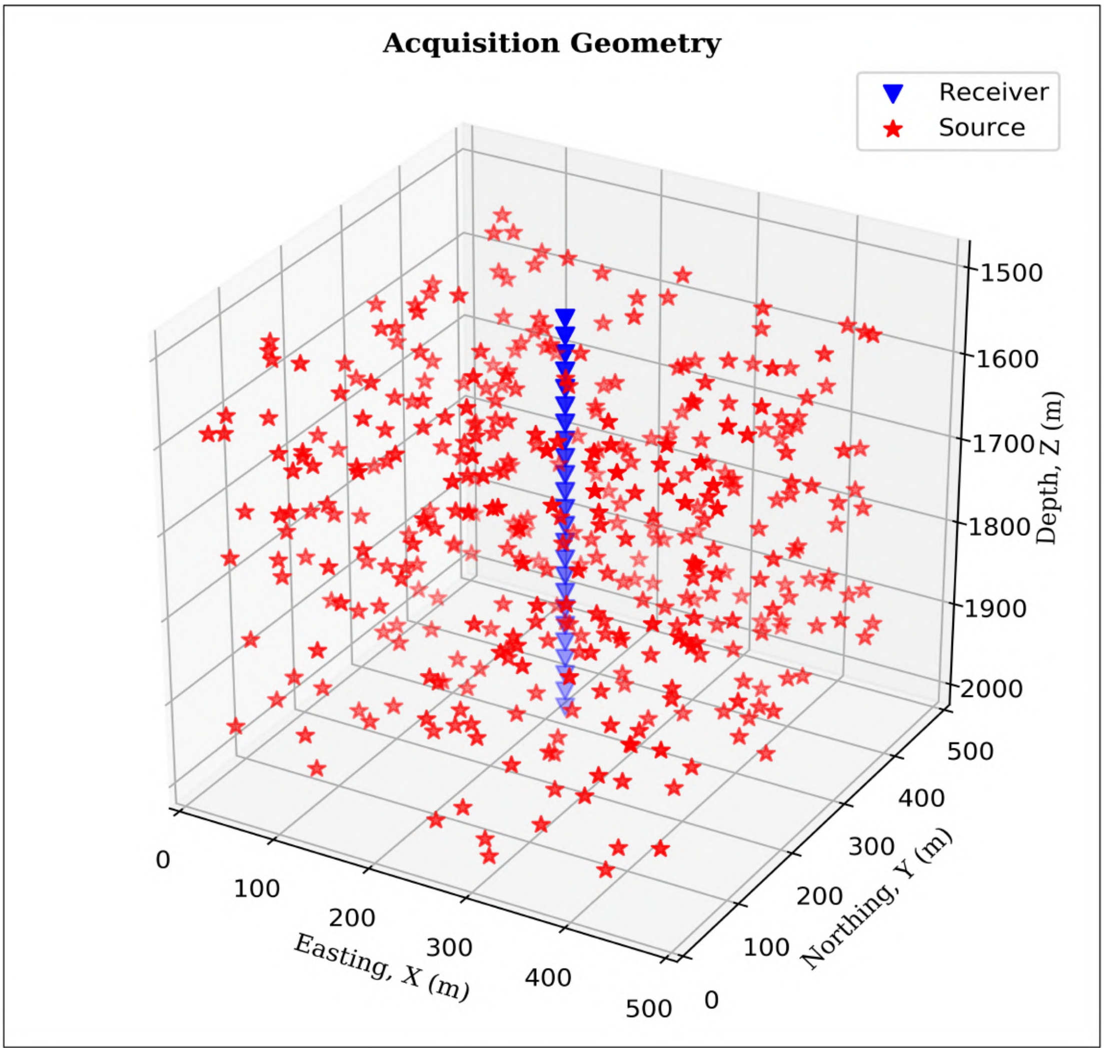

Figure 4-4: Acquisition geometry comprising of 24 3-C receivers in a downhole array (blue triangles) at intervals of 20 m, and 200 microseismic events (red stars) randomly distributed within the cube of sides 500m. The events had varying moment magnitudes in the range $-2.0 \leq \mathbf{M_w} \leq 0$.Source: [Wamriew et al., 2022a]

direct P-, and S-waves for each event. The ray-theoretical displacements generated by point dipole with moment tensor $\mathbf{M}$ is given by Equation 4.1 [Červený, 2001, Grechka and Heigl, 2017]:

$$u\left(\mathbf{X}, t; \xi\right) = \mathbf{G}\left(\mathbf{X}, t; \xi, \tau\right) * \mathbf{U}\left(\xi\right) \cdot \mathbf{M}\left(\xi, \tau\right) \cdot p\left(\xi\right). \tag{4.1}$$

Here, $\mathbf{G}\left(\mathbf{X}, t; \xi, \tau\right)$ is the zeroth-order time domain ray-theoretical Green's tensor calculated as:

$$\mathbf{G}(X,t;\xi) = \frac{\mathbf{U}(\mathbf{X})\mathbf{U}(\xi)}{4\pi\mathcal{L}\sqrt{\rho(\mathbf{X})V(\mathbf{X})\rho(\xi)V(\xi)}} \times Re\left\{\mathfrak{R}^c e^{\frac{-i\pi}{2}(\varsigma_0-\varsigma(\mathbf{X};\xi))}\delta^A\left[t-\tau-t(\mathbf{X};\xi)\right]\right\}, \tag{4.2}$$

where $\mathbf{U}$, V and $\mathcal{L}$ are unit polarization vector, phase velocity and geometrical spreading respectively; $\mathfrak{R}^c$ is the complete reflection-transmission coefficient, p is the ray parameter, τ is the origin time, t is the running time and $t(\mathbf{X};\xi)$ is the ray propagation time between source at position **xi** and receiver at the position $\mathbf{X}$.

4.2.2.3 Synthetic seismograms

We contaminated the ray-traced amplitudes using random noise to ensure the inversion stabilizes in the presence of noise and to imitate typical observed microseismic field data. The SNR ratio was calculated using Equation 4.3:

$$\mathbf{SNR} = 20\log_{10}\left(\frac{A_{signal}}{A_{noise}}\right), \tag{4.3}$$

where A is the root mean square (**RMS**) amplitude of the signal.

In computing the seismograms, We used a Ricker wavelet as the source-time function. The corner frequency of the source-time function was randomly chosen in the range 50 - 500 Hz for each point source in order to sample even the very low magnitude events. The moment magnitudes, M_w of the events were randomly sampled in the range -2.0$\leq M_w \leq$0, typical for microseismic events. Throughout the experiments, the double couple source mechanism is used since it best describes the types of failures that produce microseismic events. The data was collected for up to 0.24 seconds at a 0.001 sampling interval. Consequently, each trace had 240 time samples and the gathers had 3-D form of 3 $\times$ 24 $\times$ 240, corresponding respectively to the number of components, receivers and time samples. Figure 4-5 shows sample noise contaminated seismograms for a single event. From the figure, it is clear that addition of noise drowns the signal making it difficult to identify first arrivals.

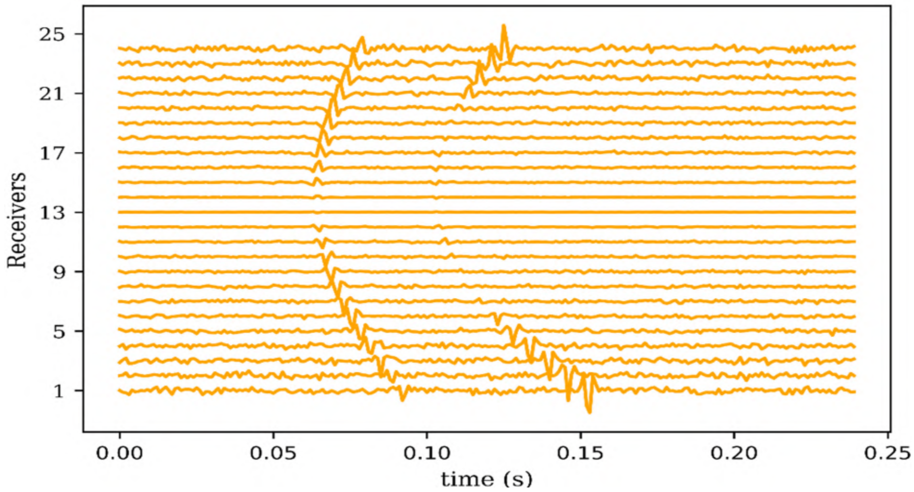

(a) X-Component

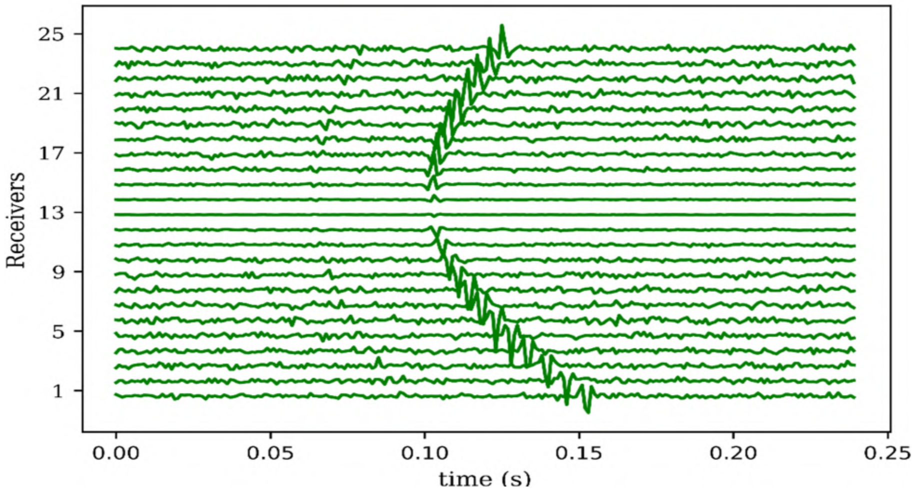

(b) Y-Component

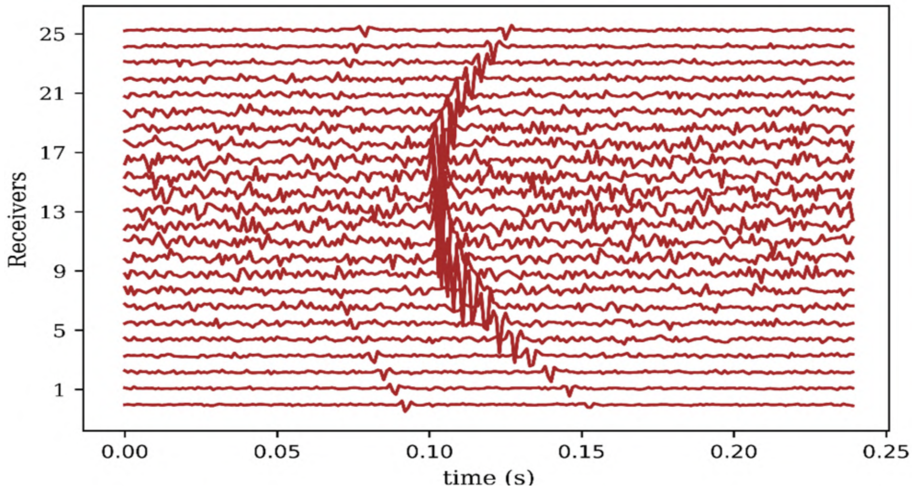

(c) Z-Component

Figure 4-5: Sample noise contaminated synthetic seismograms obtained by forward modeling. P-wave arrivals are almost entirely subdued by noise in both the X- and Y-components of the geophones. The seismograms were recorded for a duration of 0.24 seconds. Adopted from [Wamriew et al., 2022a]

4.2.3 Dataset Preparation

Neural networks require large quantity of data for training and validation purposes. In order to achieve this, we generated 100 000 gathers of 3-C synthetic seismograms (together with their labels) from the 100 000 microseismic events recorded with the 500 horizontally layered models. We contaminated the seismogram with random noise to mimic typical microseismic field data. One of the advantages of using CNNs for seismic inversion is that it requires minimal data pre-processing. Therefore, our data preparation comprised of only two almost trivial processes: scaling, and splitting the data into training, validation and testing datasets. Scaling of the data is essential for two reasons:

- it makes the data simpler for the neural network and easy to learn,
- it speeds up the training process.

One sample of the dataset comprises of a single gather of 3-C seismograms, also known as *features*, and its corresponding labels (i.e event location; $x-$, $y-$ and $z-$coordinates and velocity model parameters for each layer; v_p, v_s and ρ). We scaled each seismogram (features) by subtracting from it the median and then dividing by the interquartile range in order to ensure that the seismograms are scaled using statistics that are robust to outliers. As for the labels, we subtracted the mean and then divided by the standard deviation in order to give them the properties of a standard normal distribution with a unit variance and zero mean. Having scaled the data, we split it randomly into three sets comprising of 70%, 10% and 20% for training, validation and testing respectively.

4.2.4 Neural network model architecture

We adopted and modified the AlexNet [Krizhevsky et al., 2017] architecture, originally developed for image recognition, in order to accomplish the tasks of location of microseismic events and velocity model update, in real-time, from raw microseismic data. Figure 4-6 illustrates the comprehensive architecture of the modified model.

This network comprises of the input layer, seven convolution layers, seven batch normalization (*BatchNormalization*) and non-linear activation (*ReLU*) layers, six

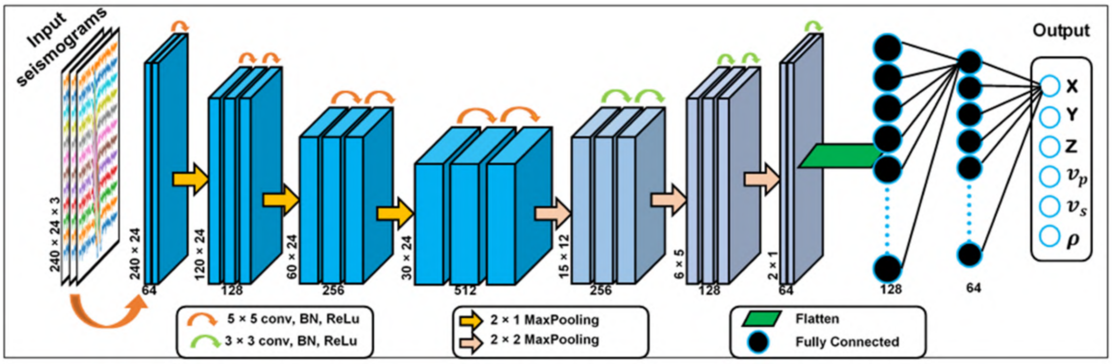

Figure 4-6: Architecture of the neural network used to locate the microseismic events and perform velocity model inversion. The blue and grey cuboids represent multiple channel feature maps with the number of channels indicated beneath the cuboids. The input dimensions of each layer is given along the lower left edge of the cuboids. The size and operations denoted by each kind of arrow are defined in the boxes beneath the network. Source: [Wamriew et al., 2022a]

maximum pooling (*MaxPooling2D*) layers, two fully connected layers and a single regression (*linear*) layer. The input matrix was zero padded before convolution to preserve the original size. Batch normalization was applied to every convolutional and fully connected layer. Each of the seven 2D convolution layers comprised of 64, 128, 256, 512, 256, 128 and 64 kernels (filters), in that order from first to last. The first four kernels had spatial dimensions of 5 × 5 and the remaining three had 3 × 3 with the depth corresponding to the number of kernels in each layer. The convolutional layers were 'fired' using the *ReLU* non-linear activation function as it is more computational efficient compared to other functions such as the *tahn* and *elu*. Every convolutional layer was followed by a two-dimensional maximum pooling layer (MaxPooling2D) with spatial dimensions of 2 × 1 for the first three layers and 2 × 2 for the final three layers, and a stride of 2. The purpose of the maximum pooling is to reduce every four (or two – for the case of 2 × 1) neurons to a single neuron, by taking the highest value between the four (or two). After the last convolution and maximum pooling, we 'flattened' the next layer and added a fully connected layer comprising of 128 and 64 nodes respectively, and *ReLU* activation functions. This was then followed with the final regression layer comprising of 6 neurons, to match the expected output of the velocity model parameters and the spatial coordinates of locations of the microseismic events. This layer was activated with a linear activation function, which allows the output to take on arbitrary values. The theoretical framework of this network is as discussed in subsection 3.5.1.

4.2.5 Training the neural network

Having set the network structure, we used the training and validation data prepared in previous section to train and validate it. The seismograms were sorted into gathers with three distinct channels: X, Y and Z, according to the receivers' components and then used as the input for the neural network. The input volume was a 3-D tensor of shape $240 \times 24 \times 3$.

Adam algorithm, which supports a variety of loss functions and penalties to fit linear regression models was used to train the model. Adam is the best for regression problems with huge amount of training data, as in our case. To speed up the training, the data was input in minibatches of size 32, after the pilot tests showed that smaller minibatch sizes led to longer training time, with no improvement in model performance, while bigger minibatch sizes compromised the regression accuracy and lowered the performance of the model. To avoid the risk of overfitting, we implemented two precautionary measures. First, we monitored how the model performed on the test dataset after each epoch and only saved its weights if there was improvement on its performance on the test dataset. Secondly, we used a validation dataset comprising of 10% randomly sampled data to validate the performance of the network, after every epoch of training. We shuffled both the validation and training data before every epoch. As the loss function to be minimized, we used the mean squared error (MSE). This loss function measures how close the output of the model matches the true values. We trained the model for 270 epochs and achieved the convergence. The neural network was constructed and trained using an open source Python library Keras running on a TensorFlow backend. We used a GPU GeForce GTX 1080 Ti.

4.2.6 Results and Discussion

After training the network, we examined its performance using the testing dataset. The testing dataset contained events with similar geological properties to those in the training dataset because the same model parameters were used to generate the dataset. This dataset comprised of 20,000 microseismic waveform gathers from 100 velocity models with number of layers ranging between 4 and 12. The dataset was not included into the network during training and was therefore unknown to the model. We input this dataset into the model and obtained the predicted values for both the velocity model and the location of the microseismic events.

In order to get a clear view of the locations of the inverted events with respect to their ground-truth values, we plot three distinct plan view projections of the locations of inverted and the actual events on the local grid as shown in Figure 4-7. For clarity purposes, only 200 randomly selected events have been plotted.

From Figure 4-7, it is clear that the locations of the inverted events match almost perfectly the ground-truth event locations. A comparison of the three plots on this figure reveals that the deep learning model gives very accurate inversion of the depth coordinate as compared to the lateral coordinates. The difference is however almost negligible.

Next, we plotted the actual versus predicted velocity values in the velocity-depth profiles to quantitatively evaluate the accuracy of the predicted velocity models. Figure 4-8 shows the 1-D velocity-depth plots. The predictions match almost perfectly the ground-truth values.

In order to validate the potential of the proposed approach, we performed a statistical analysis of the prediction results for all the six parameters under this study. The summary of the results is shown on Figure 4-9.

The event location percentage mean squared errors for x, y and z are 1.05%, 1.27% and 0.12% respectively; while the standard deviations between the predictions and the ground-truth models are 3.57 m, 4.37 m and 2.74 m for x, y and z respectively. Similarly, the errors in the velocity values are 0.54%, 0.74% and 0.18%; while the standard deviations are 41.2 ms^{-1}, 33.0 ms^{-1} and 8.23 kgm^{-3}, respectively for v_p, v_s and ρ respectively. We observe that while the errors in the predicted

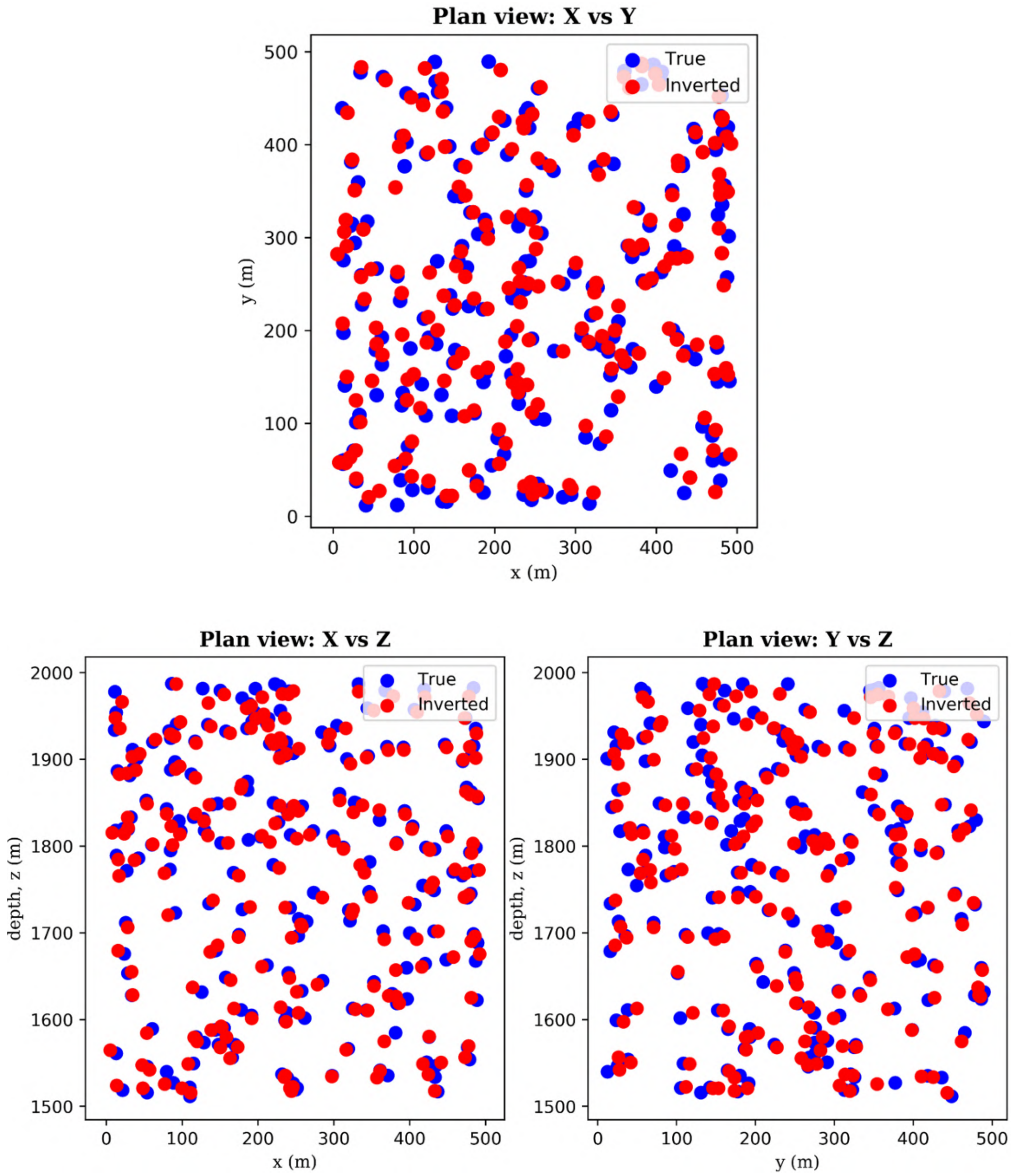

Figure 4-7: 2-D plan view plots of the ground-truth and inverted locations of the microseismic events. Here, the blue dots show the locations of the ground-truth events while the red dots are the inverted (predicted) locations by the neural network model. Adopted from [Wamriew et al., 2022a]

velocity models are lower than those in the inverted locations, the standard deviations of the velocity models are much higher. This can be attributed to the fact that the number of velocity models used in the inversion are far less than the number of events and hence the neural network may have not properly mastered the properties

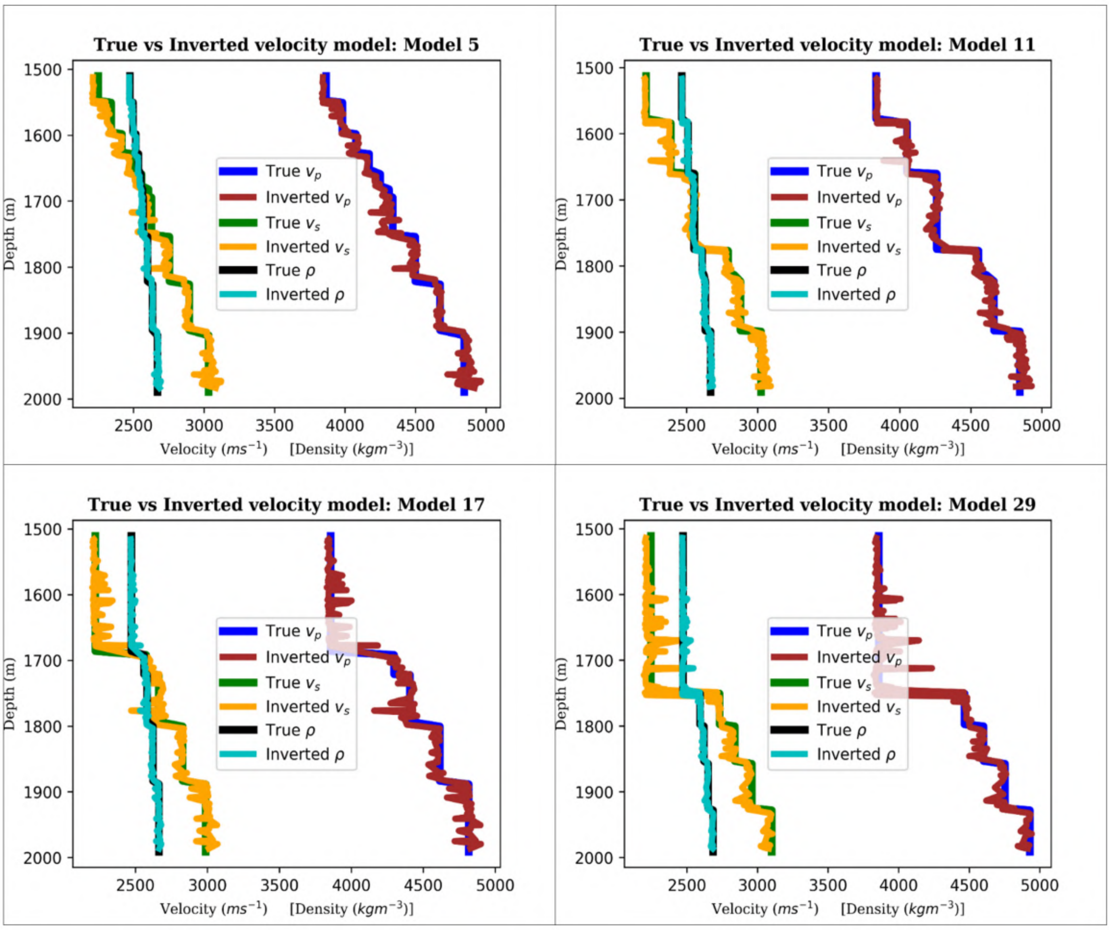

Figure 4-8: Sample inverted and ground-truth velocity model parameters: Blue, Green and Black staircases represent ground-truth P- and S-wave velocities and layer density respectively while brown, yellow and cyan their corresponding predicted values by the deep neural network. The number of layers vary in each plot between 4 and 12. Adopted from [Wamriew et al., 2022a]

of the velocity models as compared to the event locations. It is possible to improve the results by using more velocity models in the inversion. This however comes with additional computational cost.

Further, we examined robustness of the network by evaluating its performances on data with different kinds and levels of noise as discussed in the following subsections:

4.2.6.1 Random noise

During hydraulic fracture stimulation, the microseismic data acquired suffer from contamination with random noise originating from the surface activities and or even

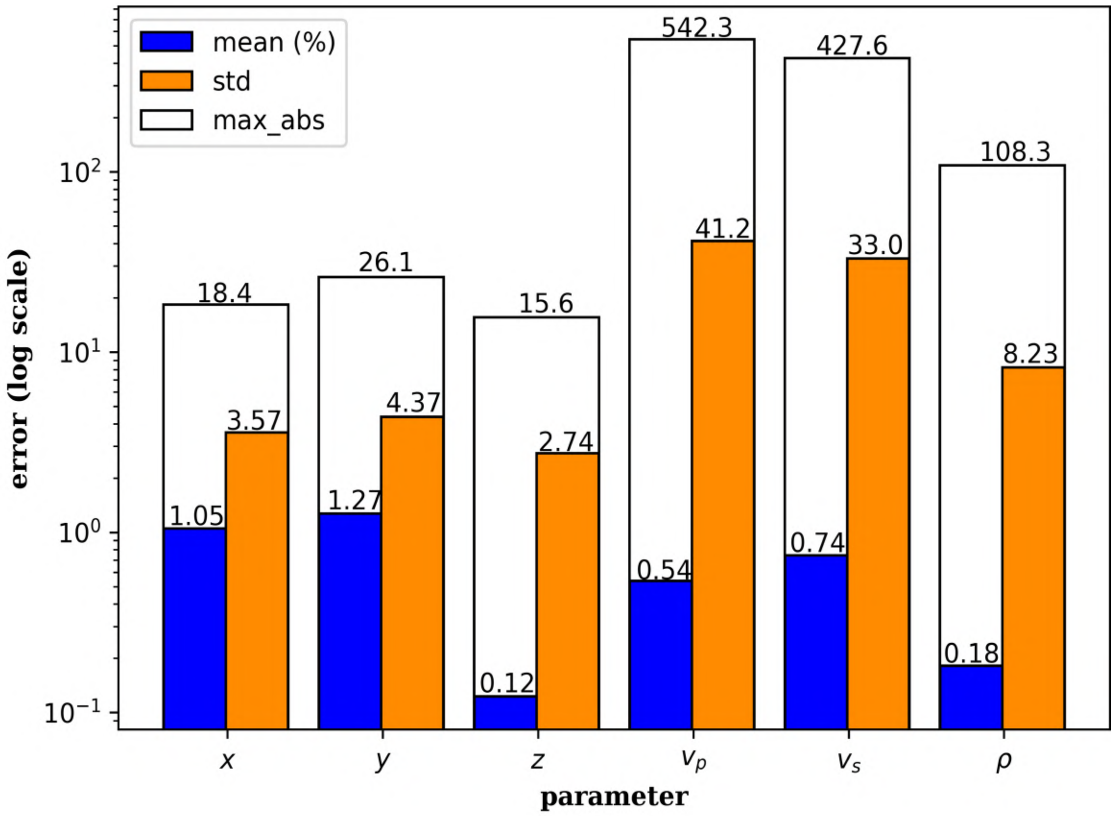

Figure 4-9: Percentage error bar graph for the location and velocity model parameters inverted by deep learning. The vertical scale is logarithmic while the parameters are shown on the horizontal axis with their respective values at the top of each bar. Blue, orange and white bars represent the mean, standard deviation and maximum errors respectively. Source: [Wamriew et al., 2022a]

downhole operations. In order to account for this scenario, and to test the robustness of the trained neural network, the computed traces were contaminated with random noise proportional to the root mean square amplitude of the trace signal and then fed into the network for prediction. The box and whisker plots in Figure 4-10 show the statistical analysis of the network's performance at various noise levels: 10%, 20%, 30%, 40% and 50%.

Generally, the neural network's performance is stable at low to moderately high noise levels but begins to decline at higher noise levels as the signal becomes completely drowned in the noise.

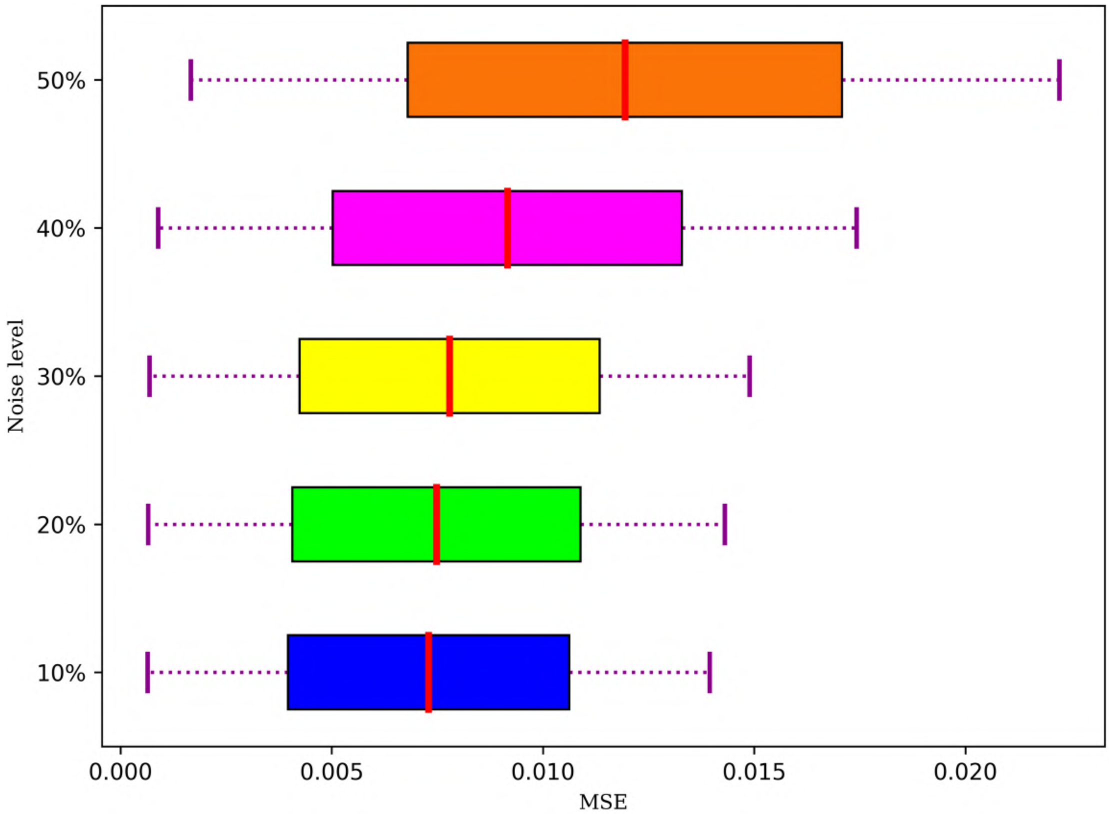

Figure 4-10: Box and whisker plot for the performance of the CNN on data contaminated with noise to the given percentages on the vertical axis. The red line in the middle of the plots represent the median while the left and right edges of the box are the lower- and upper-quartiles respectively while the left and right whiskers are the minimum and maximum mean squared errors respectively. Source: [Wamriew et al., 2022a]

4.2.6.2 Coherent noise

We further test the robustness of the neural network model by inverting data from orthorhombic media with varying levels of anisotropy. The choice of signal from such a medium as coherent noise is justifiable [Bazulin et al., 2021] since our neural network is designed for horizontally layered (VTI) media. Orthorhombic medium has three planes of symmetry and can be fully defined by nine independent components of the elastic stiffness matrix comprising of the six diagonal and three off diagonal elements, with Thomsen parameters: $\varepsilon^{(2)}$, $\delta^{(2)}$, $\gamma^{(2)}$, $\varepsilon^{(1)}$, $\delta^{(1)}$, $\gamma^{(1)}$, $\delta^{(3)}$, v_p0, v_s0; [Thomsen, 1986, Tsvankin, 1997]. If the parameters of the medium are identical in both the vertical planes of symmetry (i.e, $\varepsilon_1 = \varepsilon_2$, $\delta_1 = \delta_2$, $\delta_3 = 0$ and $\gamma_1 = \gamma_2$), and the P- and S-wave velocities in the horizontal plane are constant, an orthorhombic medium simplifies to VTI medium. To generate the test dataset for the neural network, we considered 25 VTI models with elastic parameters given in Table 4.1. We used the same geometry as before to generate the dataset.

Table 4.1: Elastic parameters of the VTI models used to generate coherent noise test dataset.

Parameter	v_{p0} ms^{-1}	v_{s0} ms^{-1}	ρ kgm^{-3}	ϵ	δ	γ
Range	3830 - 5059	2193 - 3197	2466 - 2711	0.3866	0.2800	-0.055

Further, to test for robustness, we perturbed the anisotropic parameters of these models by 10%, 20%, 30%, 40% and 50% respectively and computed the signal at each receiver position, obtaining six sets of datasets each with 5000 events. We then fed these datasets to the neural network and obtained the predictions for source location and velocity model parameters for each set. Statistical analysis of the output is shown in Figure 4-11.

The results show that the model is capable of extracting both the event locations and velocity model parameters of the orthorhombic medium to a reasonable degree of accuracy, even with increasing anisotropy up to about 50% from the initial model. Even so, the variation of anisotropic parameters least affect the velocity model compared to event locations as seen from the graph.

4.2.7 Conclusion

We propose, in this study, a new deep learning approach for microseismic events location and velocity model inversion in real-time as an alternative to the classical approaches. Unlike the classical approaches that perform inversion based on the local subsurface parameters, the novel deep learning approach is capable to reconstruct these parameters directly from microseismic records after training. Numerical experiment results show that CNN models are capable of learning, to a high degree of precision, the relationship between microseismic waveform data and the location of the events as well as the velocity model compared to classical approaches. Even more, the tasks of velocity model update and events location are performed concur-

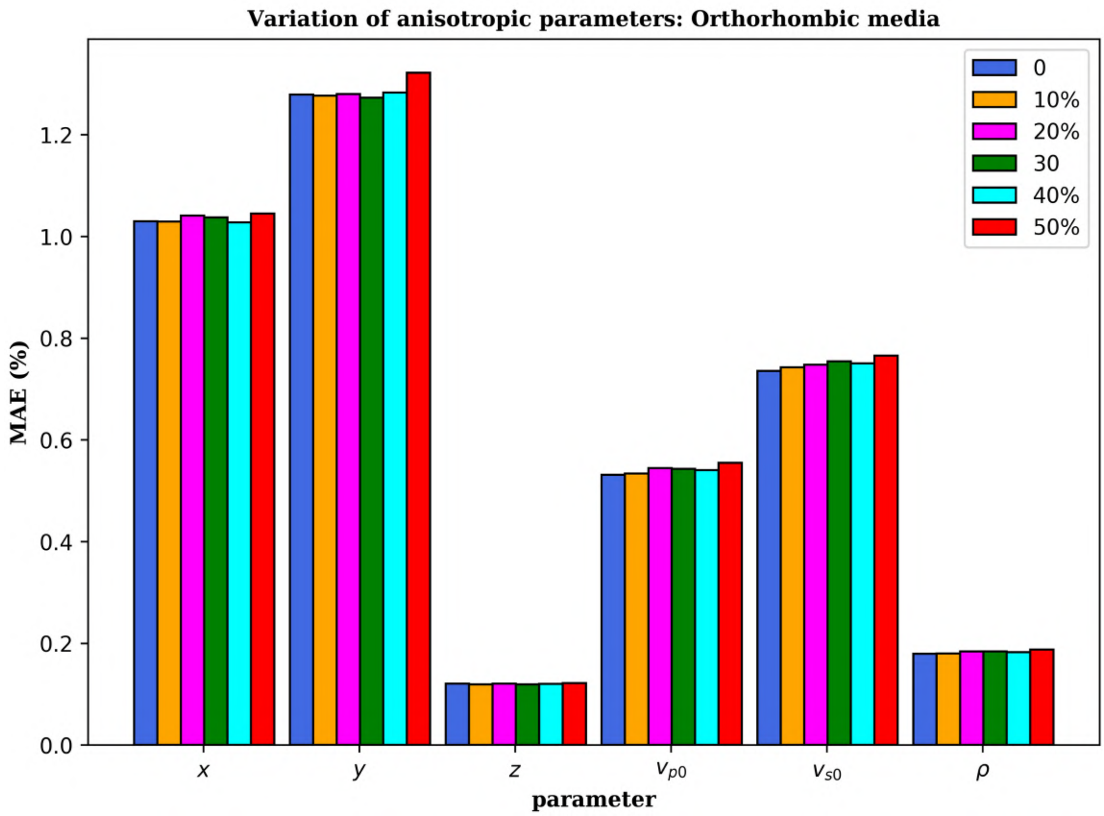

Figure 4-11: Comparison of location and velocity model parameters for orthorhombic medium inverted by the CNN trained on VTI data. Different colors represent various levels of perturbations of anisotropic parameters as indicated on the legend of the bar chart. Source: [Wamriew et al., 2022a]

rently using a single network. The deep learning approach has many benefits that make it more beneficial for microseismic monitoring in real-time. Most importantly, the approach requires minimal pre-processing of data since the model is capable to learn by itself the properties of recorded waveform data and interpret them in order to locate the microseismic events and invert for velocity models. This therefore eliminates the uncertainties resulting from data handling and processing by human expert. Once trained the model is computationally efficient.

Future work should aim at assessing the performance of the neural network model on more complex geological structures with varying levels of anisotropy. Also, the potential possibility of integrating classical approaches with specific deep learning models should be explored with the intention to develop novel neural network designs capable of handling a wide range of complex geological structures.

4.3 Detection, Location and Velocity Model Inversion.

The work in this section has been published in the *Sensors* journal [https://doi.org/10.3390/s21196627].

Title: Deep neural networks for detection and location of microseismic events and velocity model inversion from microseismic data acquired by Distributed Acoustic Sensing Array.

Coauthors: Roman Pevzner, Evgenii Maltsev and Dimitri Pissarenko.

4.3.1 Abstract

In this study, we demonstrate the feasibility of application of deep learning approach to detect and locate microseismic events and simultaneously estimate the velocity model from DAS acquired data. Unlike previous studies that use classification approach to detect the events, here, we adopt a regression-based approach in order to perform the three tasks of detection, location and velocity model inversion concurrently. We train the neural network using synthetic DAS data and validate it using both synthetic and field DAS microseismic data from a hydraulic fracture stimulation operation. The results indicate that the trained network is capable of detecting and locating microseismic events from DAS data and simultaneously update the velocity model to a high degree of precision. The mean absolute errors in the event locations and the velocity model parameters are 2.04, 0.72, 2.76, 4.19 and 0.97 percent for distance (x), depth (z), P-wave velocity, S-wave velocity and density respectively.

4.3.2 Field microseismic data

We use publicly available field data from phase 2C hydraulic fracture stimulation of the FORGE Research Site near Milford, Utah, USA [Moore et al., 2019, Martin and Nash, 2019]. Three vertical wells were used in the project, for stimulation and monitoring purposes. The monitoring well is 1000 m deep and is located 400 m to the Southeast of the treatment well as shown in Figure 4-12.

Figure 4-12: Photo (looking southeast) showing the relative location of the three boreholes. Well 68-32 is 100 m northeast of 58-32 and 78-32 400 m southeast of 58-32. Source Moore et al. [2019]

A fiber-optic cable was installed in this well and hydraulic fracture stimulation was conducted in the treatment well. The cable was connected to Silixa iDAS v3 interrogator, which natively measures strain-rate. In addition, data was also acquired using 3C geophones [Energy and Geoscience Institute at the University of Utah, 2019]. The iDAS had a gauge length of 10 m and a channel spacing of 1m along the cable. Data was recorded continuously at a sampling frequency of 2000 Hz throughout the injection period of ∼11 days in April-May, 2019. Forty microseismic events were detected and located with moment magnitudes, $\mathbf{M_w}$, in the range -1.653 to -0.519 [Pankow et al., 2020]. For detection of microseismic event, every five traces were stacked to boost the signal-to-noise ratio (SNR) and reduce the data volume. For each stacked trace, the SNR at each time step was computed. This is accomplished by measuring the root mean square (RMS) amplitude 24 ms before and 6 ms after each time sample using sliding windows. The ratio of the RMS values before and after a particular period represents the SNR at that point in time. It will be greatest at the start of an event's arrival, when the signal is located in the after window and the background noise is located in the before window. A 300 Hz minimum phase low-pass and 2-D median spatial filter were applied to attenuate the noise and remove the common-mode noise respectively. Since DAS only measures single component strain(-rate), the events were constrained to a 2-D vertical grid. Figure 4-13 shows sample traces from the field data.

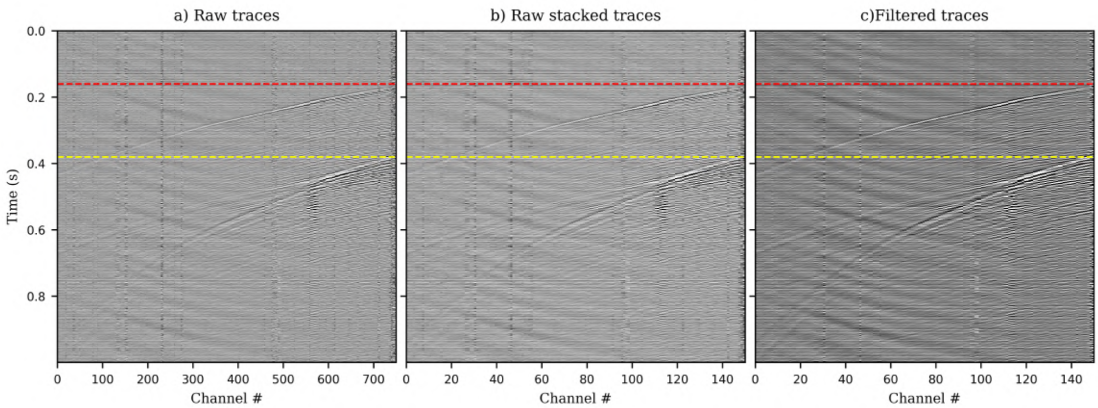

Figure 4-13: Sample detected event (a) raw DAS traces before stacking (b) raw traces after stacking (c) same traces after 300 Hz minimum phase low-pass and 2-D spatial filtering. P-wave arrival (red) and S-wave arrival (yellow). Source: [Wamriew et al., 2021b]

4.3.3 Training data

Sixty thousand synthetic microseismic events were generated and used in this study to train and optimize the neural network. In generating the synthetic data, we considered 1-D anisotropic VTI models with known boundary depths as such models represent the vast majority of geological structures encountered in microseismic monitoring. Strong anisotropy is chosen so that the network, trained on such models, will be able to generalize to lower levels anisotropy. Six hundred such models were randomly generated with varying number of layers between 3 and 12. Table 4.2 summarizes the range of velocity model parameters.

Microseismic events were randomly sampled within a 2-D vertical grid of dimensions 700 m × 900 m. The treatment and the monitoring wells were set 400 m apart as it were in the FORGE project. One hundred and fifty receivers with a spacing of

Table 4.2: Range of parameters used to generate the velocity models. Thomsen anisotropic parameters [Thomsen, 1986] of $\epsilon = 0.51$, $\gamma = 0.36$, $\delta = 0.25$, were taken to be constant throughout the layers.

Parameter	$\mathbf{v_{p0}}$ (m/s)	$\mathbf{v_{s0}}$ (m/s)	ρ **(kg/m³)**	**Depth** (m)
Minimum	3830	2193	2466	1000
Maximum	5059	3187	2711	1900

5 m were straddled in the monitoring well from a depth of 1050 m down to 1795 m. For each velocity model, 100 microseismic events were randomly generated within the grid giving 60,000 events for the 600 models. The focal mechanisms of the events were associated to shear faulting and the corresponding strike, dip and rake angles randomly generated. The events were primarily double couple with some deviatoric components owing to the anisotropy in the velocity models, and had moment magnitudes, $\mathbf{M_w}$, within the range $-2.0 \leq \mathbf{M_w} \leq 0$.

Raytracing was performed to calculate travel times and ray amplitudes of the point sources. Only the vertical channel was considered for particle displacement computation. A statistical estimate of the wavelet was first performed on the field data (Figure 4-14) to establish the appropriate source time function for the synthetic traces. Consequently, an Ormsby wavelet [Ricker and Ormsby, 1994] with the four defining frequencies randomly sampled in the intervals [50-100] Hz, [150-200] Hz, [300-350] Hz and [400-450] Hz, respectively was loaded onto each source, and velocity seismograms computed. The data was recorded at a 0.5 ms sampling interval for a duration of 1 second and the particle velocity converted to strain-rate. Conversion of dynamic particle velocity ($\mathbf{v}_z$) to strain-rate ($\dot{\epsilon}_{zz}$) along the fiber is straightforward since DAS record is essentially the difference between two geophones over time. Thus the conversion can be achieved by the relation [Bakku, 2015]:

$$\dot{\epsilon}_{zz}^{DAS} = \frac{v_z\left(z + \frac{L}{2}\right) - v_z\left(z - \frac{L}{2}\right)}{L}, \tag{4.4}$$

where v_z is the dynamic particle velocity at depth location z, and $\dot{\epsilon}_{zz}^{DAS}$ is the converted uni-axial DAS strain-rate in the vertical direction . In this conversion, L is the spatial gauge length.

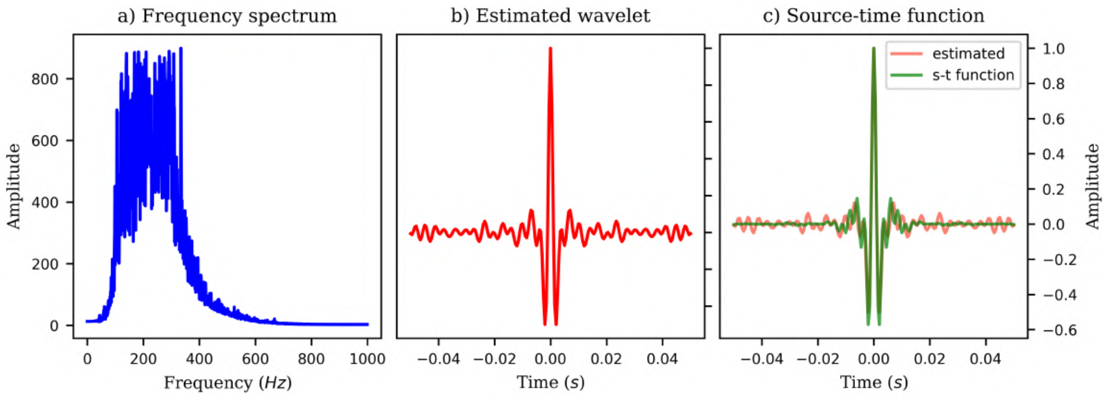

Figure 4-14: Statistical wavelet estimate from field data (a) mean frequency spectrum of field signal (b) estimated wavelet from field data (c) source time function used in generating synthetic data. Source: [Wamriew et al., 2021b]

The seismograms were then contaminated with real-ambient noise from the DAS field records and in addition to the 60,000 events, further 10,000 noise seismograms from the field data were added to the training dataset. The noise was also stacked together and their amplitude normalized to ensure that the amplitudes are comparable before contamination. Figure 4-15 shows samples of the synthetic events signal and ambient noise.

One sample of the dataset comprises of a stack of 1-C seismograms from a single event and its corresponding labels comprising of the depth (z) coordinate and the velocity model parameters: v_{p0}, v_{s0} and ρ. For regression purpose, all the labels for noise were set to zeroes.

4.3.4 Convolutional neural network (CNN)

We used a 50–layer deep residual network commonly referred to as ResNet50 [He et al., 2016] to perform the task of inversion of the microseismic data recorded by DAS. This deep neural network overcomes the problem of vanishing gradient as the residual links speed up the network convergence. The network comprises of 49 convolutional layers and a single fully-connected (FC) layer. The convolutional layers are split in five blocks of 1, 9, 12, 18, 9 and 1 layer(s) respectively from first to last, with varying kernel sizes and strides. For instance, the single convolutional layer in the first block comprises of 64 kernels of sizes 7×7 and stride of 2 while the

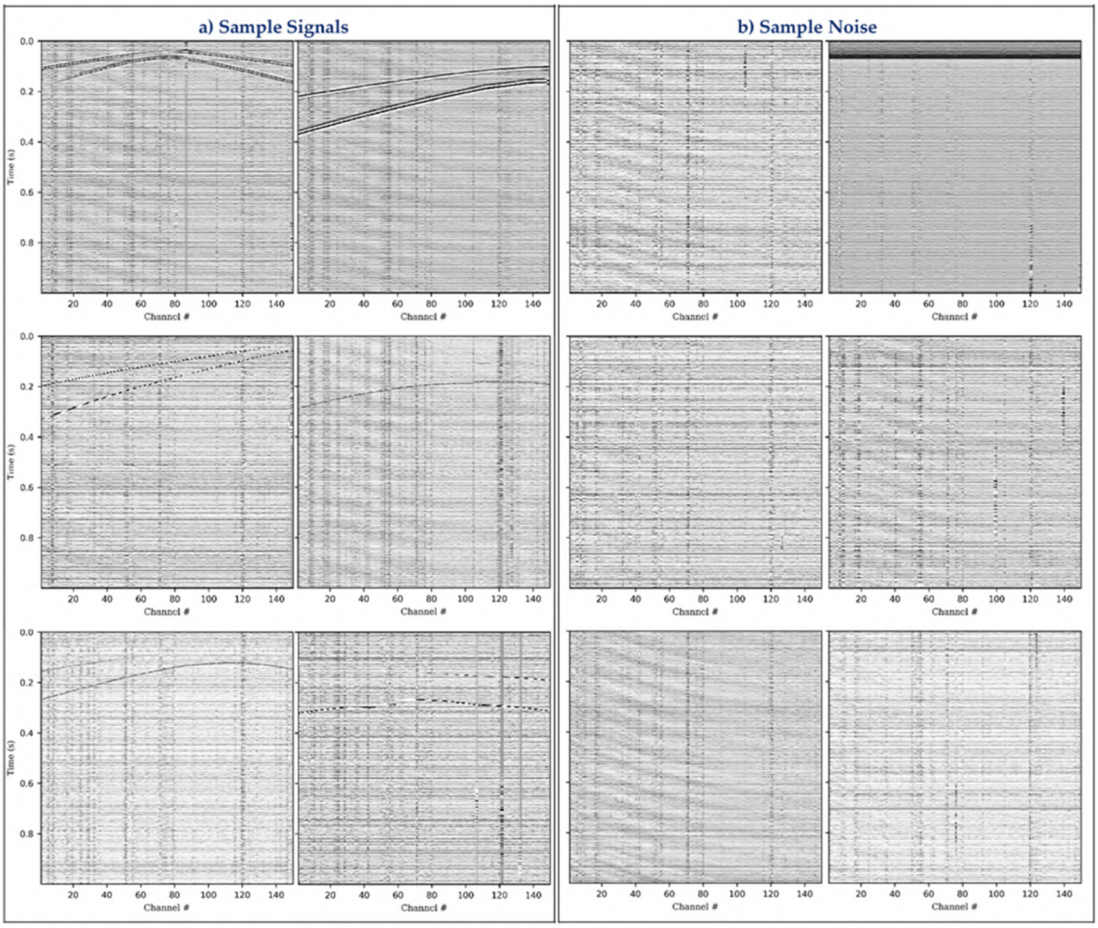

Figure 4-15: Sample synthetic data **(a)** DAS microseismic events contaminated with ambient noise from field data **(b)** sample DAS ambient noise from extracted from field data. Source: [Wamriew et al., 2021b].

first three layers of the second block comprise of 64, 64 and 256 kernels of sizes 1×1, 3×3 and 1×1 respectively, and strides of 2. Table 4.3 gives a summary of sizes of outputs and convolutional kernels of the network while Figure 4-16 is a visual presentation of the network architecture. Each convolutional layer was activated using the $ReLU$ activation functions due to its computational efficiency. Maximum and average pooling layers were applied after the first and last convolutional layers respectively.

The following adjustments were made to ResNet50 in order to accomplish the task at hand : after the last convolution layer, a fully connected layer comprising of 256 nodes was added followed by the final regression layer comprising of 5 neurons, to match the expected output of the microseismic event location and the velocity

Table 4.3: Details of the 50-layer deep residual neural network used in this study. Abbreviations: Conv – Convolution layer, Conv_x – Convolution and identity layer)

Layer ID	**Number of layers**	**Output size**
Block 1[Conv1]	7 × 7, 64, stride 2	128 × 128
	3 × 3 maxPool2D, stride 2	
Block 2[Conv2_x]	[1 × 1, 64 3 × 3, 64 1 × 1, 256] ×3	64 × 64
Block 3[Conv3_x]	[1 × 1, 128 3 × 3, 128 1 × 1, 512] ×4	32 × 32
Block 4[Conv4_x]	[1 × 1, 256 3 × 3, 256 1 × 1, 1024] ×4	16 × 16
Block 5[Conv5_x]	[1 × 1, 512 3 × 3, 512 1 × 1, 2048] ×3	8 × 8
	Global average pooling 2D	
Fully connected	nodes = 256, activation = Linear	2 × 1
	Total parameters	**24 106 178**
	Trainable:	24 053 186
	Non-trainable:	52 992

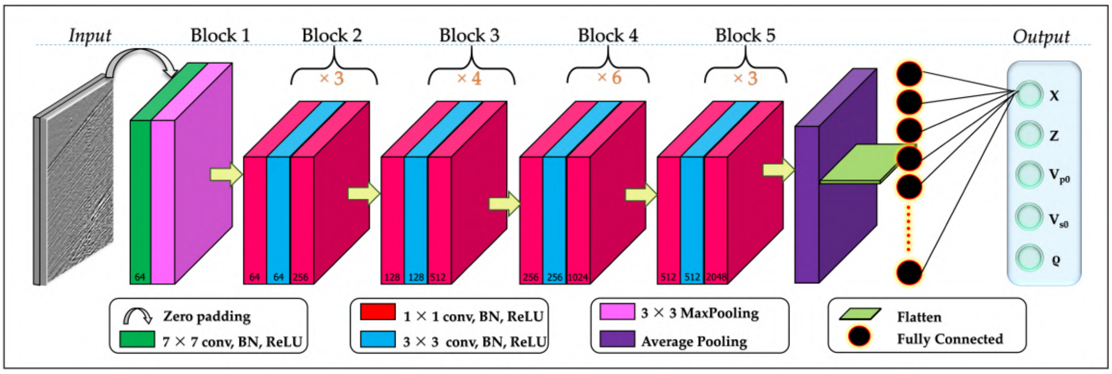

Figure 4-16: Deep convolutional neural network architecture used in the study. Green, blue and red cuboids represent multi-channel feature maps with number of channels shown at the bottom of the cuboids. The input dimensions of each layer is given in Table 4.3. Source: [Wamriew et al., 2021b].

model parameters. The network architecture is shown in Figure 4-16.

4.3.5 Training and validation of the network

The dataset was split as follows: 5000 samples comprising of 50 velocity models were reserved for testing while the remaining 65,000 was split in the ration 7:3 for training and validation respectively. The test dataset was only fed into the network to obtain the predictions after the training was complete. The seismograms were converted to grey scale images of pixel dimensions 256 × 256 before input into the network. The data was input in mini-batches of size 32 after prior tests indicated that smaller or larger mini-batch sizes did not improve the network's performance. Two precautionary measures were taken to avoid overfitting: first, we tracked the model's performance on the validation dataset after each epoch and only saved its weights if its performance improved on the validation dataset. Second, we used a validation dataset comprising of 30% of the entire dataset, randomly sampled, to evaluate the network's performance after each epoch of training. The neural network was built and trained using the open source Python package Keras, which was run on a TensorFlow backend. We used a GeForce GTX 1080 Ti GPU for training and the model trained for 135 epochs before reaching convergence. The training took 7.2 hours.

4.3.6 Results

4.3.6.1 Synthetic data analysis

The test dataset comprising of 5000 DAS microseismic events from 50 distinct velocity models was used to evaluate the performance of the trained network. As a first step in evaluating the model's performance, we input the entire test dataset and plot the scatter diagram (Figure 4-17) of predictions vs ground-truth values to determine the correlation between the predictions and the actual values.

The scatter plots for both location and velocity model estimates show strong positive correlation between the predicted and the ground-truth values, indicating that deep learning is capable to invert the raw DAS microseismic data for the detection,

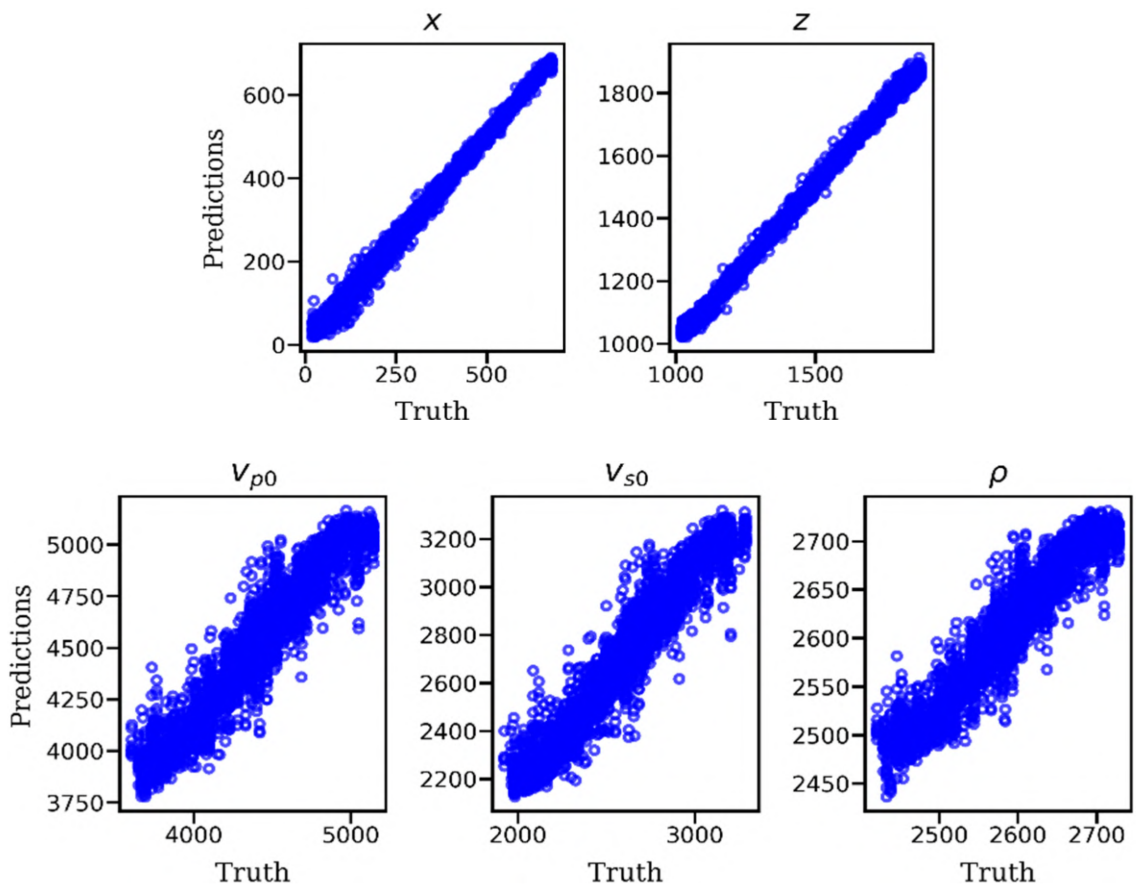

Figure 4-17: Scatter plots of predictions versus ground-truth values of event depth location and velocity model parameters v_{p0}, v_{s0} and ρ. The plots show strong positive correlation. Adopted from [Wamriew et al., 2021b].

location and velocity model inversion.

To examine the goodness-of-fit of the trained model, we performed residual diagnostics. Two rules of thumb are verified, i.e, for a good model, the residuals should randomly deviate from zero, and secondly, the residuals should be close to zero themselves. Figure 4-18 displays the histograms of residuals for each parameter under study and an envelope of probability density function.

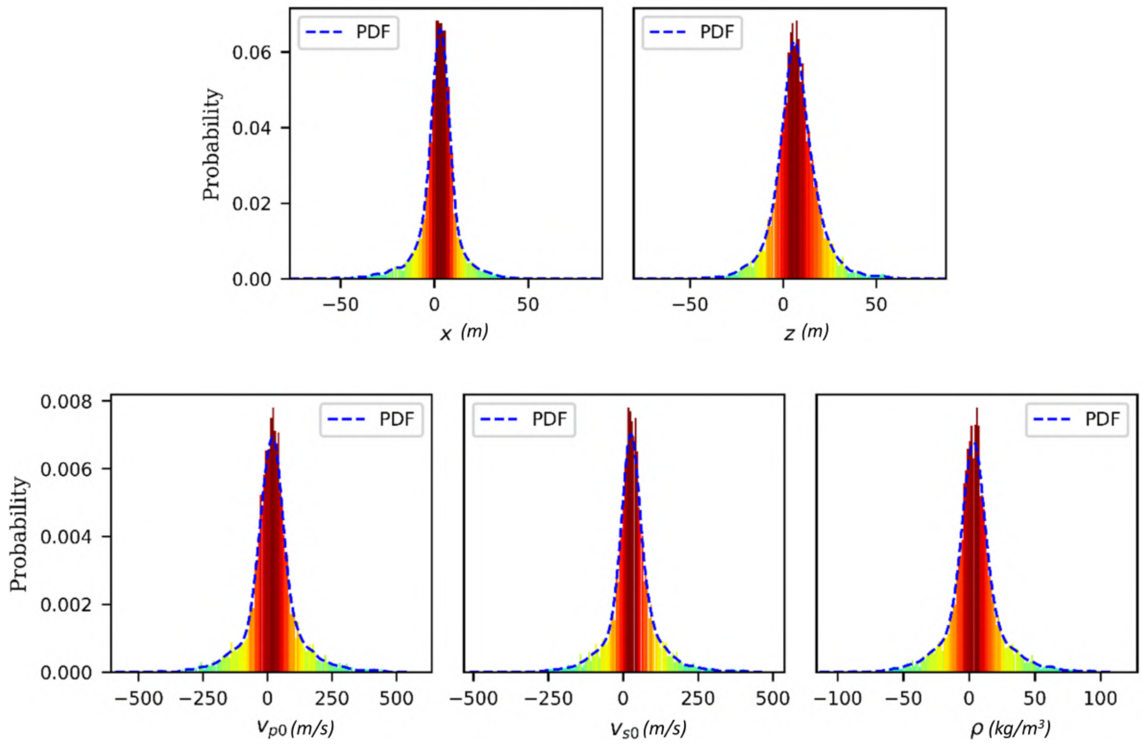

Figure 4-18: Residual diagnostic histograms for trained CNN model. The blue envelope represents the probability density function. The velocity model parameters of each histogram is indicated at the bottom center of each plot. Adopted from [Wamriew et al., 2021b].

The distribution of the residuals for the trained model, as seen on Figure 4-18, follow a normal distribution for all the five parameters under study. The mean of the residuals is very close to zero for all the parameters, which indicates compliance with statistical assumptions that residuals have zero-mean and constant variance. Having verified the suitability of the model, we proceed to evaluate its output for each of the five parameters.

In order to visualize the relative locations of the predicted and ground-truth events, we plot a 2-D plan view projection of the event locations as shown in Figure 4-

19. For clarity, we plotted only 100 events from a single velocity model. From Figure 4-19, it is clear that the predicted event locations (blue stars) almost perfectly match the ground-truth locations (red stars) with very minimal deviations in some cases.

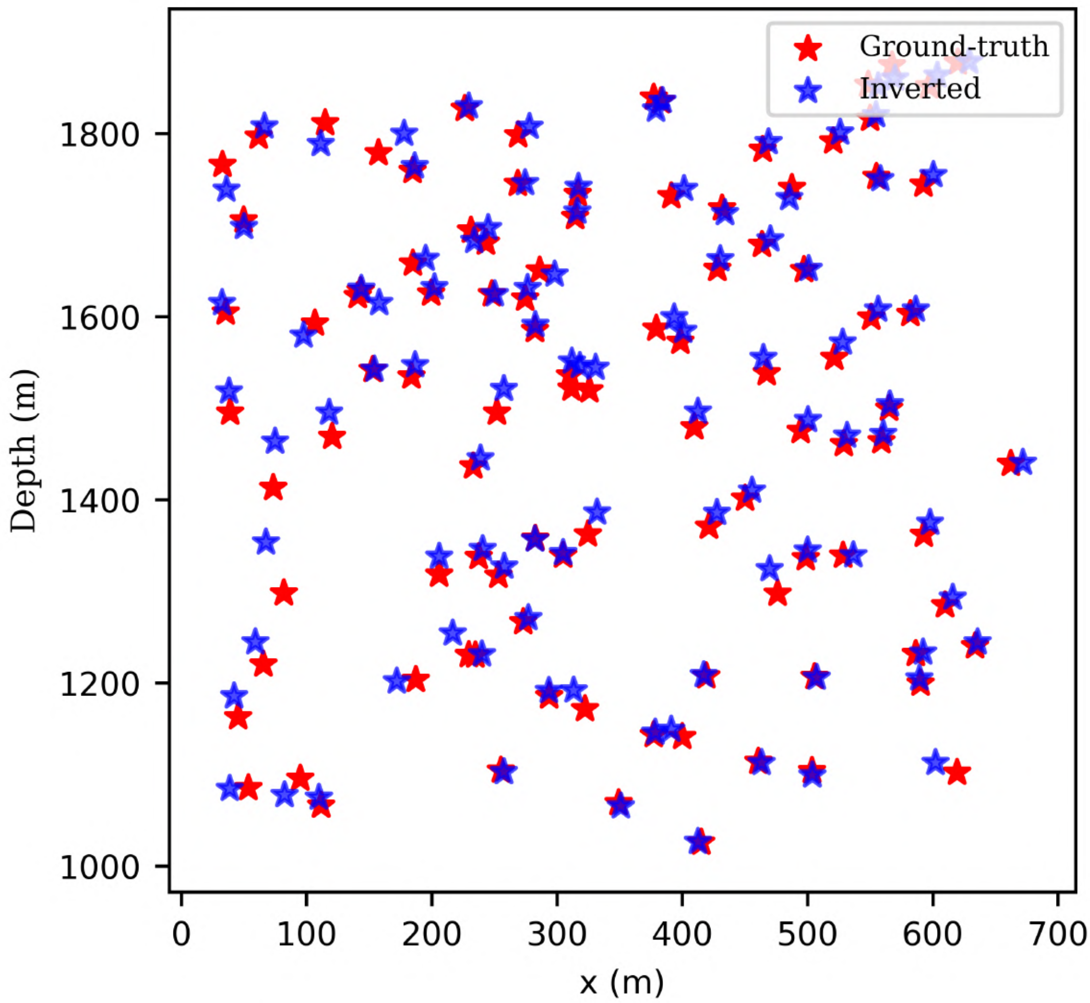

Figure 4-19: 2-D plan view projection of the inverted DAS microseismic depth locations (blue stars) versus ground-truth locations (red stars). Only 100 events from one velocity model are displayed. Source: [Wamriew et al., 2021b].

Further, we compare the velocity model parameters from the predictions against the ground-truth values in the velocity versus depth profiles displayed in Figure 4-20 to quantify the accuracy of the velocity model predictions. Evidently, the predicted velocity models, to a large extent, match the patterns of the ground-truth models.

To further validate the capability of the proposed approach, we performed statistical analysis of the prediction results for all the five parameters under study. A

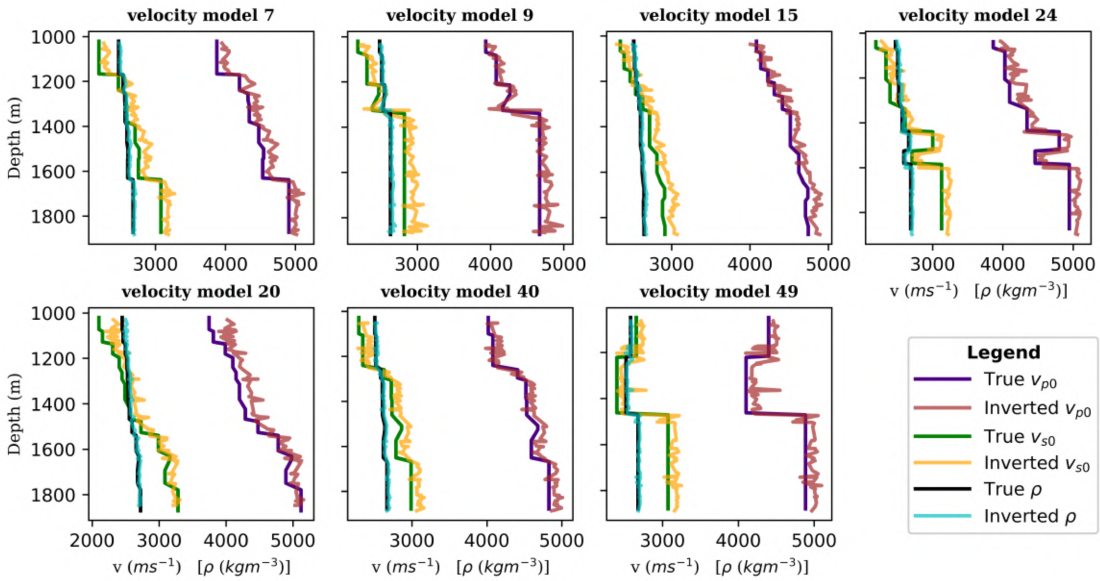

Figure 4-20: 1-D velocity model profiles for prediction versus ground-truth values. Blue, green and black represent ground-truth v_{p0}, v_{s0} and ρ values respectively, while red, orange and cyan the corresponding inverted values. Source: [Wamriew et al., 2021b].

summary of the results is presented on Figure 4-21. The mean absolute errors in the inversion are 2.04, 0.72, 2.76, 4.19 and 0.97 percent for x, z, v_{p0}, v_{s0} and ρ respectively, while the corresponding standard deviations are 5.49, 4.80, 26.30, 24.60 and 26.96.

We observe that while the errors in the predicted velocity models are minimal, the corresponding standard deviations are somewhat high compared to that of inverted locations. This can be attributed to two reasons. First, the number of velocity models used in the inversion are significantly smaller than the number of microseismic events, meaning we have more information on the latter. Second, while the number of microseismic events was maintained constant in all the velocity models, the number of layers in a velocity models varied between 3 and 12. Hence, the neural network may have not adequately learned the properties of the velocity models in comparison to the event locations. The results can be improved by increasing the number of velocity models in the inversion and maintaining constant number of layers throughout the experiments.

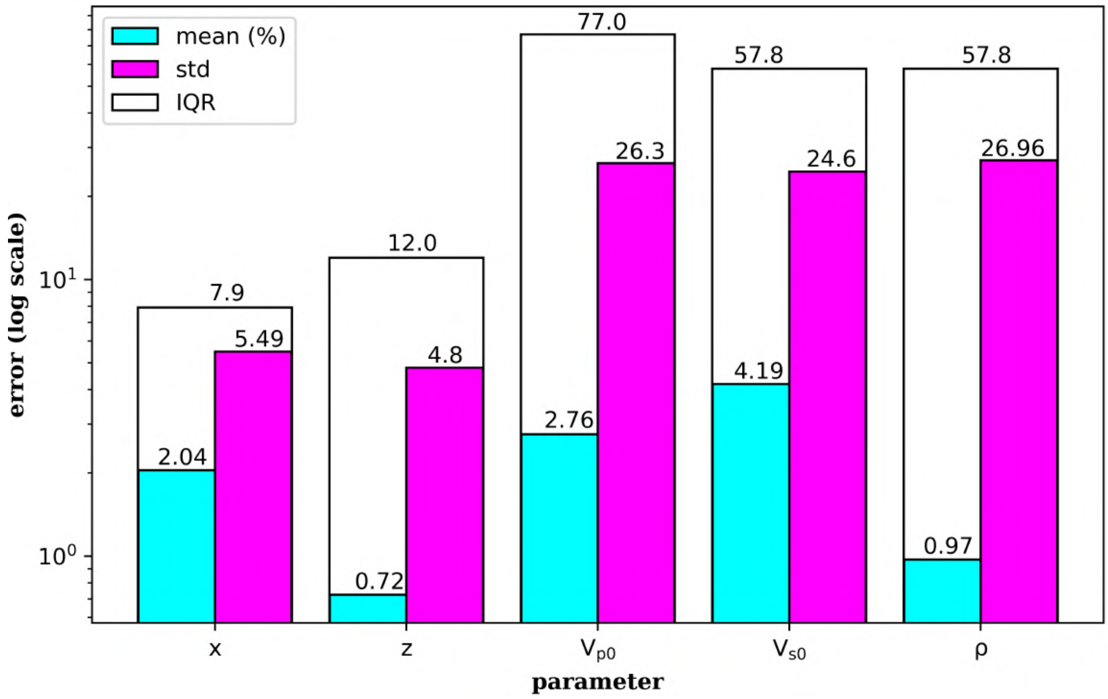

Figure 4-21: Error bar graph for the location and velocity model parameters inverted by deep learning. The vertical scale is logarithmic while the parameters are shown on the horizontal axis with their respective values at the top of each bar. Cyan, purple and white bars represent the mean absolute error, standard deviation and the interquartile ranges respectively. Source: [Wamriew et al., 2021b].

4.3.6.2 Field data analysis

In this section, we test the limits and potential of the deep learning approach with field data from FORGE project [Energy and Geoscience Institute at the University of Utah, 2019], discussed in subsection 4.3.2. The microseismic database consists of 15 seconds long SEG-Y data files collected over a period of 11 days, with events of different magnitudes. We chose a three-hour subset of the data, cycles 7 and 8 of stages 27 and 28, confirmed to contain 30 events [Moore et al., 2019, Energy and Geoscience Institute at the University of Utah, 2019]. We split the data to 1-second lengths using a sliding window to give a time sample of 2000 time steps for use in the pre-trained neural network. We then applied 300 Hz minimum low pass filter followed by a 2-D median filter to attenuate the noise and remove the common-mode noise respectively. The entire test dataset thus contained 10,800 samples which were amplitude-normalized and then converted to grey scale images of pixel size 256 $\times$ 256. No further processing was done.

For testing the pre-trained CNN model, we input the entire test dataset into the network and obtain predictions of event locations and velocity model parameters v_{p0}, v_{s0} and ρ. A plot for the estimated velocity model is shown in Figure 4-22.

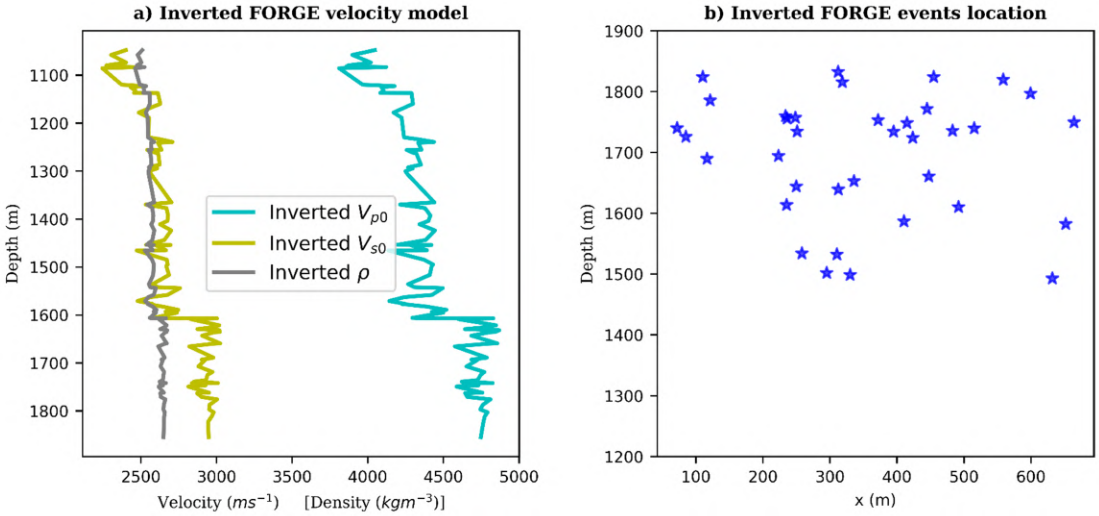

Figure 4-22: Inversion results: (**a**) Velocity model of FORGE estimated by the neural network. Cyan, yellow and grey curves are the raw patterns output of v_{p0}, v_{s0} and ρ by the network, (**b**) Events locations. Source: [Wamriew et al., 2021b].

In addition to the 30 previously confirmed events, the neural network was able to detect and locate six more low magnitude events that had not been previously reported. Determination of the events moment magnitudes is however beyond the scope of this study.

4.3.7 Discussion

Both DAS and deep learning are promising new technologies in microseismic monitoring. A combination of both could be a game changer. DAS has in the recent times, become a favorite alternative for acquisition of microseismic data due to its spatial and temporal resolution and physical robustness. However, the large volumes of originating from DAS sensors make it very difficult to process in real-/semi-real-time using the conventional routines. This is where deep learning comes in. While there are plenty of standard tools for seismic event detection, location and velocity model inversion, the deep learning approach combines all three stages and, as such, saves the time.

In the foregoing sections, we have attempted to demonstrate the feasibility of application of deep learning approach for inversion of microseismic data acquired by DAS. Results for both synthetic and field data from FORGE enhanced geothermal project near Milford Utah depict the potential of deep learning approach for inversion of DAS acquired data. We were able to detect and locate microseismic events from DAS records to high degree of accuracy, and approximate the velocity model (Figure 4-22). The tasks can be performed in real-time, in the case of hydraulic fracturing operation or in semi-real time, in case of passive seismic monitoring. The proposed approach could help both petroleum and mining engineers fast-track field decision making process and assist in production optimization. However, it must be validated with long-term monitoring and data from different formations.

In generating the training dataset, we used ray tracing however, it is possible to use other methods such as reflectivity or full waveform inversion. Ray tracing was chosen due its versatility and numerical efficiency. When performed in a smoothly varying layered media, ray tracing is capable of delivering reliable approximate solutions with sufficient levels of accuracy. Its primary limitation is that, because it is an approximate solution to the wave equation, it is only practically functional in smoothly varying medium and might produce incorrect results or even fail in singular regions [Červený and Pšenčík, 2011]. As mentioned in forward modelling, we used 1-D layered anisotropic velocity models but more accurate results can be achieved using a 3-D model and iterative methods.

4.3.7.1 Limitations of DAS

The sensitivity of DAS is dependent on the angle of incidence of seismic energy with respect to the orientation of the fiber optic cable due to well-known properties underlying the system's operation. Generally, DAS is most sensitive to seismic signals incident along the axial direction of the sensing optical fiber. On the contrary, the system is less sensitive to those signals that are incident perpendicular to the axial direction of the sensing fibers, that is, broadside signals.

It is worth noting that this directionality is linked to the phase of the seismic wave that arrives at a specific incidence angle. If the angle of incidence, ϕ, (Figure 4-23) is

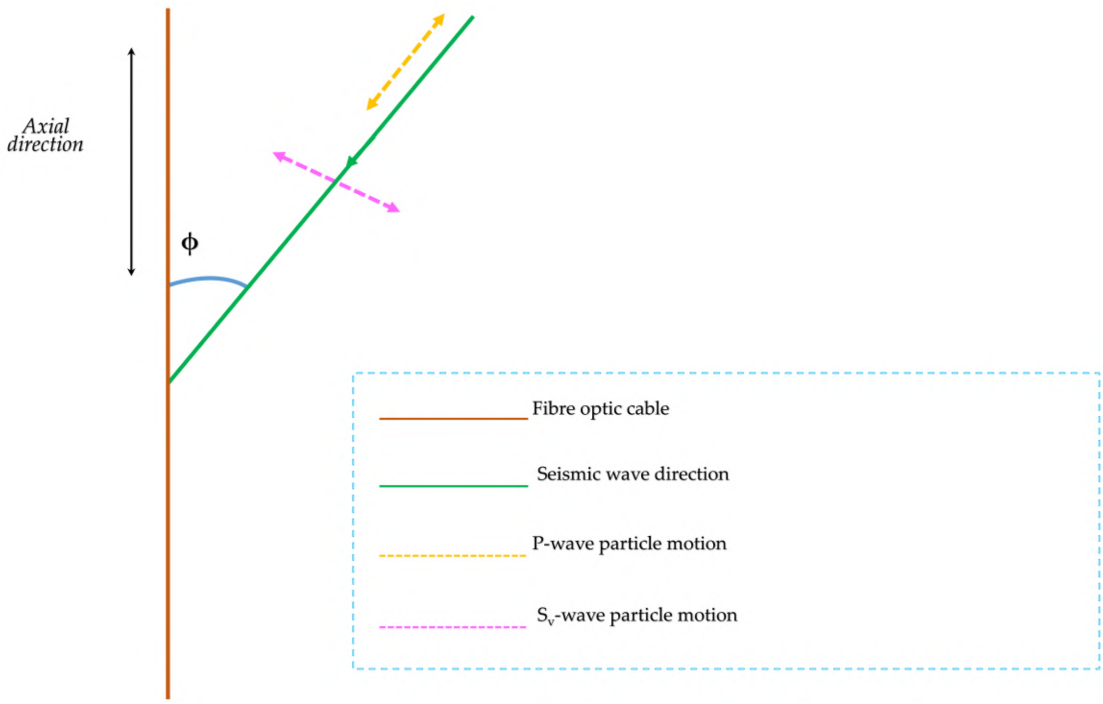

Figure 4-23: Directional sensitivity of DAS to body waves. DAS is most sensitive to the component of particle motion that is in the axial direction. Source: [Wamriew et al., 2021b].

defined as 0 degrees for arrivals propagating along the fiber's axial direction and 90 degrees for arrivals propagating perpendicular to the optical fiber, the sensitivity to P-wave arrivals is greatest for angles of incidence approaching 0 and least for angles approaching 90 degrees. On the contrary, since S-waves propagate perpendicular to directions of motion, their sensitivity increases as the incidence angle approaches 90 degrees and diminishes for angles closer to 0.

4.3.7.2 Limitations of Deep Learning

Due to their large architectures, deep learning models require large volumes of data for training. While availability of data is not a challenge in microseismic/ passive seimic monitoring using DAS, the large volumes of data make training of the models extremely computational expensive. Also, a model trained in one situation will requre retraining to be applied to a different situation. Once trained however, the models are computational efficient. In addition, despite their excellent performance on the benchmark dataset, deep learning models may fail on field dataset if there are significant differences between the field data and the training data. For field application of deep learning, it is a major challenge to generate the characteristics and links between data domain and model domain.

4.3.7.3 Field implementation

The deep learning approach can be easily implemented in the on-site automated field data processing workflow. A field experiment where DAS data acquisition and processing was automated was recently published by Isaenkov et al. [2021]. In that study an array of 5 deep wells generates ∼1.3 *Tb* of raw data per day, and the data is processed as active time-lapse VSP. The data pre-processing was done in a similar way to the way we prepared the data for analysis in this study. As explained in section 3.2 above, the pre-processing involves filtering, downsampling and conversion of gathers to greyscale images.The images are then fed to the pre-trained CNN model for inversion. The neural network outputs the locations of detected events as well as an estimate of the velocity model. The inversion process is very fast, for instance, it took 673 milliseconds on an octa-core CPU to process 1.3 GB of pre-processed data. In the case of hydraulic fracturing, data can be streamed in real-time thus reducing the input data size and decreasing the processing time.

4.3.8 Conclusions

The results of this study show that deep neural network models are capable of learning the relationship between microseismic waveform data and the location of the events as well as the velocity model to a high degree of precision. Furthermore, the tasks of updating the velocity model and locating events are carried out concurrently on a single network. The deep learning approach has numerous advantages that make it more appealing for semi/real-time microseismic monitoring. Most importantly, the approach requires minimal data pre-processing because the model is capable of learning and interpreting the properties of recorded waveform data by itself, in order to detect and locate microseismic events and invert velocity models. As a result, the uncertainties associated with data handling and processing by human experts are eliminated. Furthermore, as more data is acquired, the network's performance can be improved in real-time during training. The model is computationally efficient once it has been trained for instance; the inversion of the five thousand test dataset only took 673 milliseconds on an octa-core CPU Future research should focus on evaluating the neural network model's performance on more complicated geological formations with various degrees of anisotropy. In order to build innovative neural network designs capable of managing a wide range of complicated geological formations, the idea of combining conventional techniques with specialized deep learning models should be investigated.

4.4 DAS Data Analysis Using Deep Learning

In this section, we demonstrate the use of two cutting-edge technologies: distributed acoustic sensing (DAS) and deep learning for microseismic monitoring and analysis. Building on the work in section 4.3, we investigated the possibility of improved microseismic event detectability and location: (i) given a well-known velocity model; (ii) using different neural network architectures; and (iii) reducing the number of output parameters. In addition, the output detections by the neural networks were verified using the conventional STA/LTA method. The work presented in this section has been published in the *Remote Sensing* journal [https://doi.org/10.3390/rs14143417].

Title: Microseismic Monitoring and Analysis Using Cutting-Edge Technology: A Key Enabler for Reservoir Characterization.

Coauthors: Desmond Batsa Dorhjie, Daniil Bogoedov, Roman Pevzner , Evgenii Maltsev, Marwan Charara, Dimitri Pissarenko and Dmitry Koroteev.

4.4.1 Abstract

Microseismic monitoring is a useful enabler for reservoir characterization without which the information on the effects of reservoir operations such as hydraulic fracturing, enhanced oil recovery, carbon dioxide, or natural gas geological storage would be obscured. This research provides a new breakthrough in the tracking of the reservoir fracture network and characterization by detecting the microseismic events and locating their sources in real-time during reservoir operations. The monitoring was conducted using fiber optic distributed acoustic sensors (DAS) and the data were analyzed by deep learning. The use of DAS for microseismic monitoring is a game changer due to its excellent temporal and spatial resolution as well as cost-effectiveness. The deep learning approach is well-suited to dealing in real-time with the large amounts of data recorded by DAS equipment due to its computational speed. Two convolutional neural network based models were evaluated and the best one was used to detect and locate microseismic events from the DAS recorded field

microseismic data from the FORGE project in Milford, United States. The results indicate the capability of deep neural networks to simultaneously detect and locate microseismic events from the raw DAS measurements. The results showed a small percentage error. In addition to the high spatial and temporal resolution, fiber optic cables are durable and can be installed permanently in the field and be used for decades. They are also resistant to high pressure, can withstand considerably high temperature, and therefore can be used even during field operations such as a flooding or hydraulic fracture stimulation. Deep neural networks are very robust; need minimum data pre-processing, can handle large volumes of data, and are able to perform multiple computations in a time- and cost-effective way. Once trained, the network can be easily adopted to new conditions through transfer learning.

4.4.2 Microseismic Data

The process of obtaining a high-resolution DAS microseismic dataset requires the use of specific data processing. This is mainly due to the technological features of the data acquisition. In the most typical downhole DAS installation, the fiber optic cable is permanently cemented on the outside of the well-casing. When a propagating seismic wavefield from a source passes through the fiber optic cable, it reacts to the propagation and, as a result, lengthens and shortens in the longitudinal direction of the fiber optic cable. The lengthening and shortening of the fiber optic cable cause interference wave patterns, similar to the vibrations of a coil in a conventional survey seismic receiver. These interference patterns are collected and interpreted by the interrogation unit, which reproduces the seismic waveform at specific points on the cable. Usually these points are arranged in constant increments every 1–5 m, similar to a receiver array. The distance between the "receivers" in the DAS cable results in the revolutionary ability of the DAS cable to provide inexpensive, high spatial, and temporal resolution downhole seismic measurements.

We used the downhole DAS microseismic data recorded during the phase 2C hydraulic fracture stimulation experiment at the FORGE research site near Utah, in the United States and discussed in details in subsection 4.3.2.

4.4.3 Data Processing

The acquisition geometry in the DAS application caused the seismic sources and receivers to be at very different elevations. Such geometry invalidates the common midpoint assumption, which is critical for traditional common depth point (CDP) processing. This makes generating reflection images from the data recorded in this geometry much more difficult than from the data recorded with sources and receivers at the same elevation. For our purposes, however, there is no need for high-level processing techniques since a neural network is capable of learning the properties of the seismic waveforms by itself to a high level of precision [51]. To refine the wavefield of the DAS data and to simplify the task of searching for seismic events in the data, spectral processing of the data can be considered necessary and sufficient [56]. Thus, the key task of DAS processing, in our case, was to increase the SNR and refine the wavefield to separate seismic events and simplify their identification. As shown in Figure 4-24, it was almost impossible to distinguish the seismic events by wave patterns from the raw data as the data are drowned in noise. This is typical of DAS data.

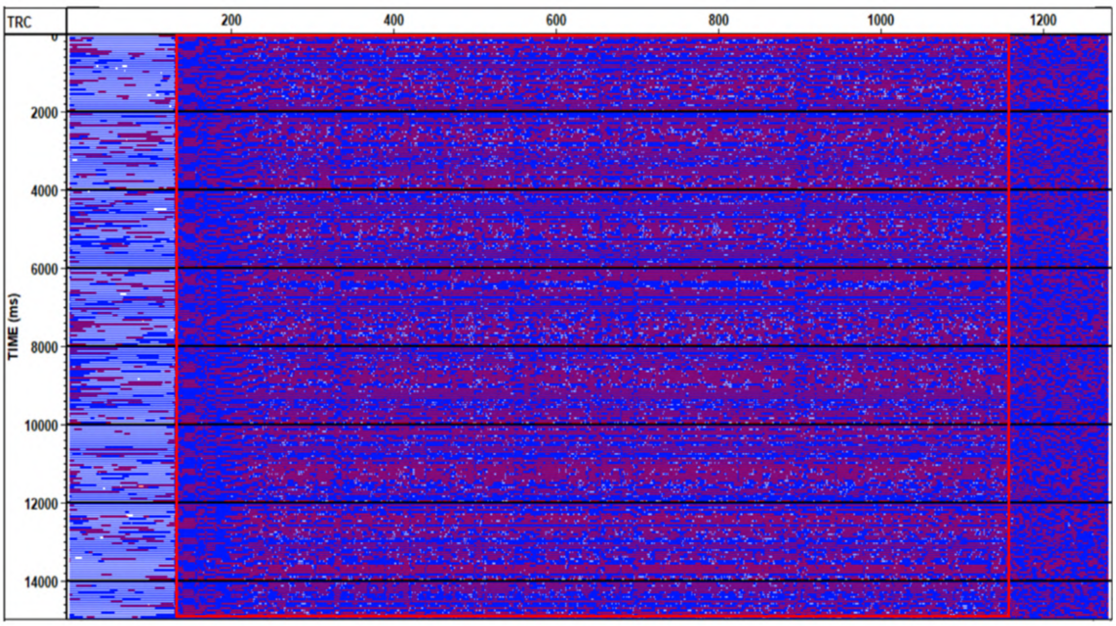

Figure 4-24: A fragment of the DAS record before processing. The area of interest highlighted in red is due to the technical peculiarities of the data collection. Source: [Wamriew et al., 2022b].

The complete spectral image of the full seismic section in Figure 4-24 was analyzed before processing the data (Figure 4-25(a). Due to the large variations in signal amplitudes, it is more appropriate to separate the wavefields in the case of DAS data by using a logarithmic scale such as the dB value scale used here.

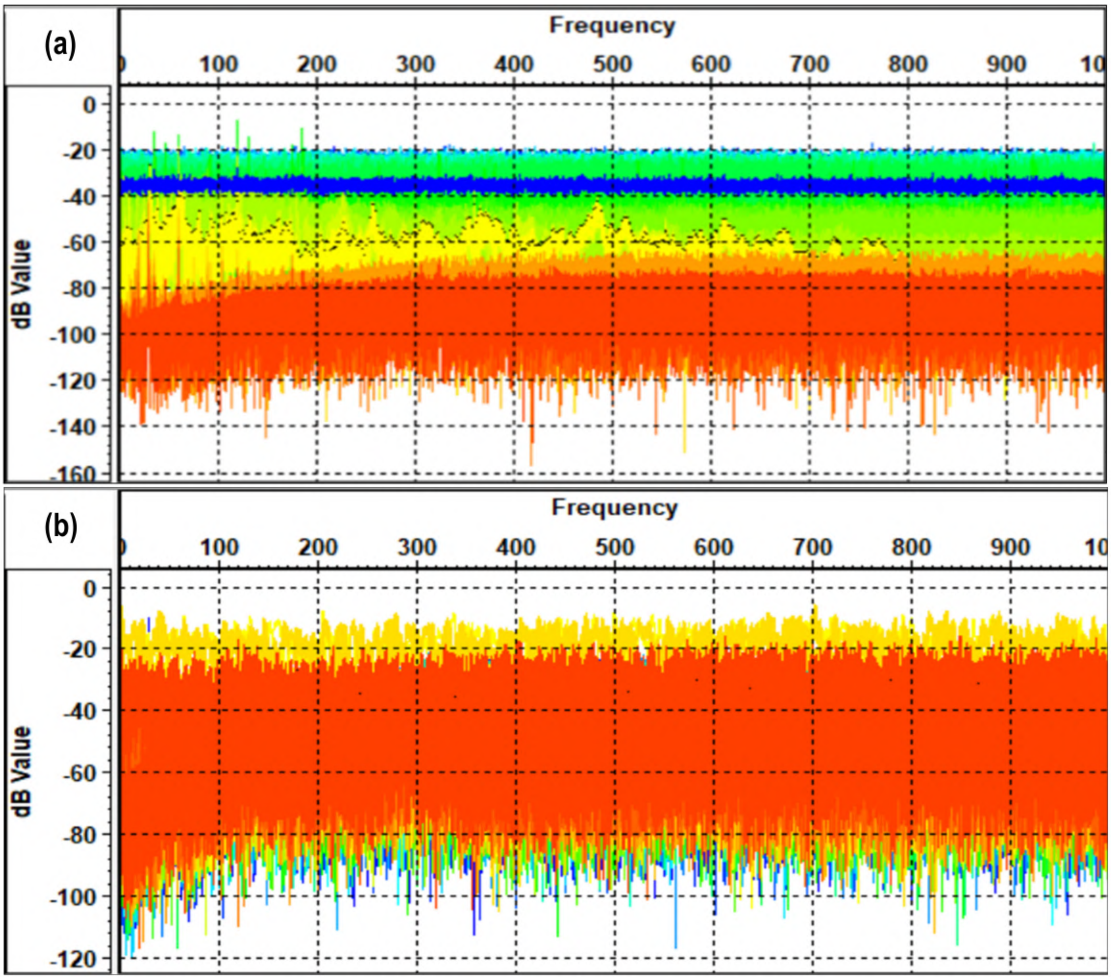

Figure 4-25: (a) All traces of the dB spectrum graph display of the DAS data (blue shows the averaged amplitude spectrum over the entire section; the background coherent noise domain is shown in green; orange—the tail part of the record, close to the bottom of the well. The yellow color on the spectrum shows the events we are interested in). (b) The bottom graph shows the amplitude-frequency spectrum representing the region of interest, depicted in Figure 4-24 inside the red rectangle. Source: [Wamriew et al., 2022b].

The spectral picture of the full data section can be separated by origin, but after cutting off the entire data area that is not of interest (data outside the red rectangle from the Figure 4-24), only the spectrum of the target data interval is left (Figure 4-25)b). The spectral image of the area of interest appears to be extremely noise-prone and the separation of the wavefields seems to be a difficult task.

Having established the frequency spectrum of the useful signal, the processing flow in Figure 4-26) was adopted to achieve the overall goal of improving the SNR. The workflow was based on classical spectral data processing.

Figure 4-26: DAS data processing workflow.

The choice of scaling was due to the high spike values on the seismic profile. The mean scale showed the greatest effectiveness for clarifying the wave pattern. For two-dimensional (2-D) F-k filtering, the horizontal box rejection zone was selected, as shown in Figure 4-27.

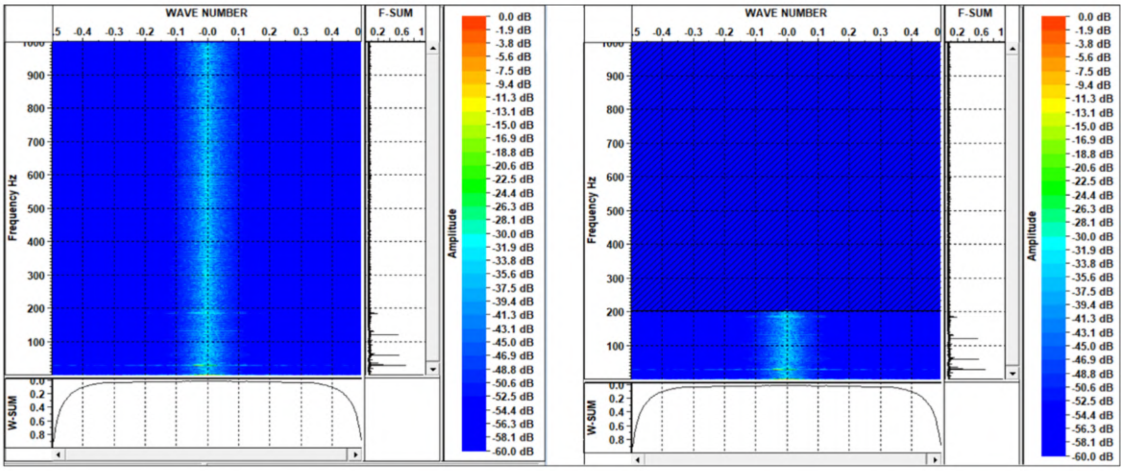

Figure 4-27: Original F-k area on the left. The right picture shows the horizontal box rejection zone. Source: [Wamriew et al., 2022b].

As can be seen in the F-k region beyond 200 Hz, the useful signal is lost and there remains constant noise. In the next step, the remaining noise is filtered out with the band pass Ormsby filter. Analysis of the result at this stage showed the need to apply a 2-D median filter [Duncan and Beresford, 1995, Justusson, 1981] to remove the common mode noise, which appeared as persistent horizontal stripes in the data. As a result of applying the DAS processing graph presented above, we were able to significantly improve the SNR of the data as well as prepare the data for seismic event detection without the loss of useful data (Figure 4-28).

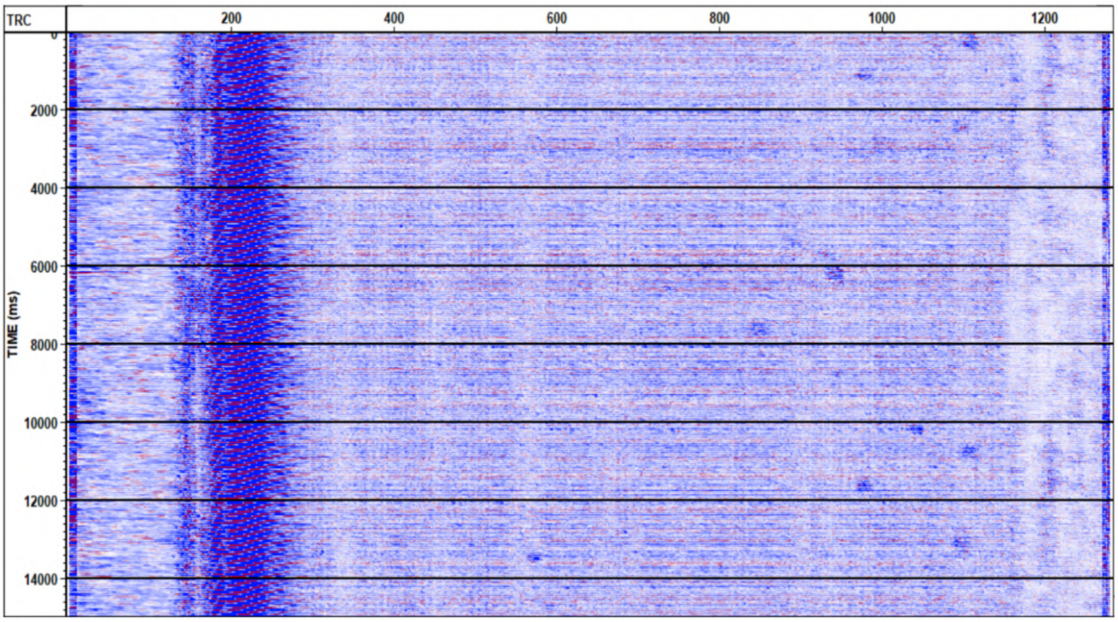

Figure 4-28: Result of the DAS data processing using the presented workflow. Source: [Wamriew et al., 2022b].

4.4.4 Training Dataset

The training data for the deep neural network comprised of twenty thousand synthetic microseismic events contaminated with noise from the field data and an equivalent amount of pure noise drawn from the field data, giving a total of forty thousand samples. Each sample comprised of gathers of receiver responses from 150 receivers used in the forward model. Thus, one sample consisted of 150 seismic traces. A single 1-D anisotropic velocity model with three layers was used in the forward model. The S-wave velocity was taken from the FORGE velocity estimates by Zhang and Pankow [2021] and Wamriew et al. [2021b], while the P-wave velocities and the densities were estimated using the Castagna [Castagna et al., 1985] and Gardner [Gardner et al., 1974] equations, respectively. Relatively high Thomsen anisotropic parameters [Thomsen, 1986] of $\epsilon = 0.51$, $\gamma = 0.36$, and $\delta = 0.25$, were chosen since previous studies have revealed that a neural network, trained on high anisotropic parameters, would generalize well when presented with waveforms from lower anisotropic models [Wamriew et al., 2022a]. Table 4.4 shows the 1-D velocity model used in the study.

The monitoring well was set 400 m from the hypothetical treatment well and

Table 4.4: 1-D velocity model used in the forward models.

Parameter	$\mathbf{v_{p0}}$ (m/s)	$\mathbf{v_{s0}}$ (m/s)	ρ (kg/m^3)	Depth (m)
Layer 1	3834	2133	2439	1000
Layer 2	4317	2549	2513	1100
Layer 3	4979	3120	2604	1600

was arrayed with one hundred and fifty single-component receivers separated at 5 m intervals from a depth of 1050 m downward. This dense spatial sampling was deliberately chosen to match the final downsampled field DAS records. Twenty thousand microseismic events with moment magnitudes between -1.5 and 0.5, similar to the field data, were sampled at random in a two-dimensional plane of a width and depth 700 × 900 m, respectively. The amplitudes and travel times of the transmitted waves were calculated using ray-tracing. The trapezoidal Ormsby wavelet with low-cut, low-pass, high-cut, and high-pass frequencies was injected at each source point and randomly sampled in the intervals 50–100 Hz, 200–250 Hz, 300–350 Hz, and 400–550 Hz, respectively, to calculate the particle velocity. The data were sampled at a frequency of 2000 Hz for a duration of 1 s. The DAS record is essentially the difference between two geophones over time. Thus, the particle velocity can be converted to the strain-rate using Equation 4.4.

The obtained strain-rates were then amplitude normalized before being added noise from the field data. The noise was spatially downsampled to 5 m, split into a 1 second length by a moving window, and then rescaled to make sure that the amplitudes compared with those of the strain-rates before the addition. Additional 20,000 pure field noise samples were reserved for addition to the training data. A human expert manually inspected the continuous wavelet transform of the noise dataset to ensure that they did not contain any low-magnitude microseismic events. The final step in the preparation of the data involves the conversion of the samples to PNG images of pixel sizes 256 × 256 × 1 ready for use in training the neural network.

4.4.5 CNN Model Architecture

To achieve the objectives of detecting and locating microseismic events from the DAS microseismic data, we designed and employed two deep CNN-based neural networks, namely the residual neural network and an inception-residual neural network. The residual-type deep convolutional neural network comprised of forty-nine convolutional layers, one maxpooling layer, one global average layer, and one fully connected layer. The model was further divided into five blocks with the first block comprised of one convolutional layer with sixty-four filters of dimensions 5×5 and stride of 2; a single batch normalization layer; a single 2-D maximum pooling (maxpool2d) layer and a $ReLU$ activation function. The subsequent four blocks were each comprised of equal numbers of convolutional and identity layers. Figure 4-29 and Table 4.5 show a detailed representation of the architecture of the neural network model.

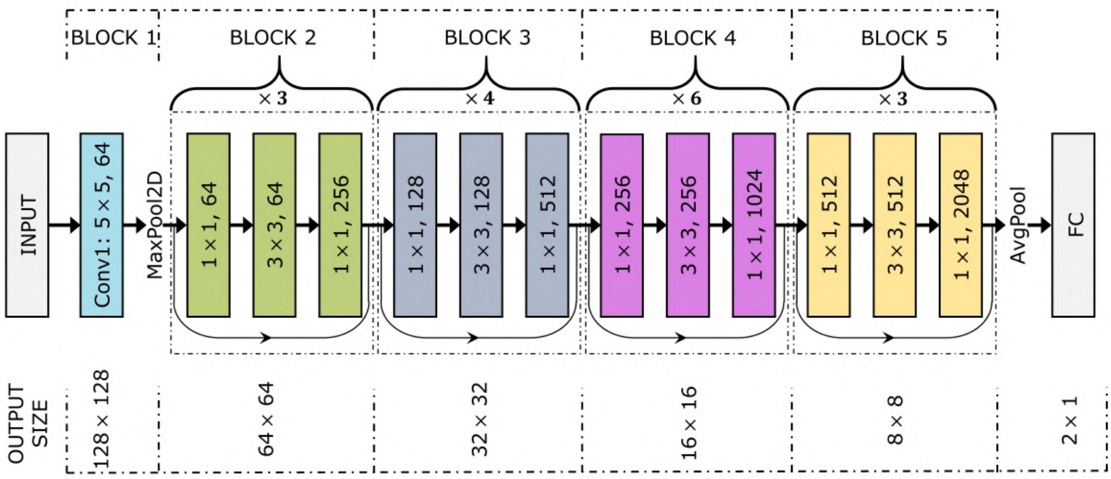

Figure 4-29: Architecture of the 50-layer deep neural network used in this study. Abbreviations: Conv—convolutional layer, MaxPool2D—two-dimensional maximum pooling layer, Avg-Pool—global average pooling layer, FC—fully connected layer. Source: [Wamriew et al., 2022b].

The network also has residual linkages that help to alleviate the problem of diminishing or exploding gradients by providing an alternative path for the gradient to pass through. The identity layers help to speed up the network training by controlling the number of training parameters. The fifth convolutional block is followed by a 2-D global average pooling layer and the output is then flattened into

Table 4.5: Details of the 50-layer deep residual neural network used in this study. Abbreviations: Conv—convolution layer, Conv_x—convolution and identity layer)

Layer ID	**Number of layers**	**Output size**
Block 1[Conv1]	7×7, 64, stride 2	128×128
	3×3 maxPool2D, stride 2	
Block 2[Conv2_x]	[1×1, 64 3×3, 64 1×1, 256] $\times 3$	64×64
Block 3[Conv3_x]	[1×1, 128 3×3, 128 1×1, 512] $\times 4$	32×32
Block 4[Conv4_x]	[1×1, 256 3×3, 256 1×1, 1024] $\times 4$	16×16
Block 5[Conv5_x]	[1×1, 512 3×3, 512 1×1, 2048] $\times 3$	8×8
	Global average pooling 2D	
Fully connected	nodes = 256, activation = Linear	2×1
	Total parameters	**24 106 178**
	Trainable:	24 053 186
	Non-trainable:	52 992

a 1-D continuous linear vector. A dropout layer is then applied to randomly set 30% of the vector output to zeros in order to avoid overfitting. The result is input into a fully connected layer with a linear activation function and two output nodes to match the expected outputs of the locations of the microseismic events.

The Inception-ResNet neural network combines, as the name suggests, the architectures of both the inception and the ResNet models in order to boost its performance. It is comprised of three main building blocks (i.e., the stem block, inception-residual block, and the scaling block). The stem is a pure inception block that forms the input to the neural network. It essentially contains several partitions of sub-networks, which are joined together to form a large network. The partitions provide flexibility for tuning the parameters (e.g., number of filters) of various network layers without affecting the quality of the full network. This block is then followed by an inception-residual block, which uses less expensive inception layers in conjunction with residual layers in order to compensate for the dimension reductions introduced by the inception block. The final block is the scaling block, which scales down the residuals before adding them to the previous layer's activation. This in turn helps to stabilize the training without the need to manually change the training rate as advocated by He et al. [2016]. A detailed description of the Inception-ResNet model can be found in Szegedy et al. [2016]. We adopted the Inception-ResNetv4 model, introducing only changes to the dropout layer (see subsection 4.4.6) and the fully connected. We added a dense layer with two output nodes (for x and z coordinates) with a linear activation function in order to perform the regression. Figure 4-30 shows the architecture of the network.

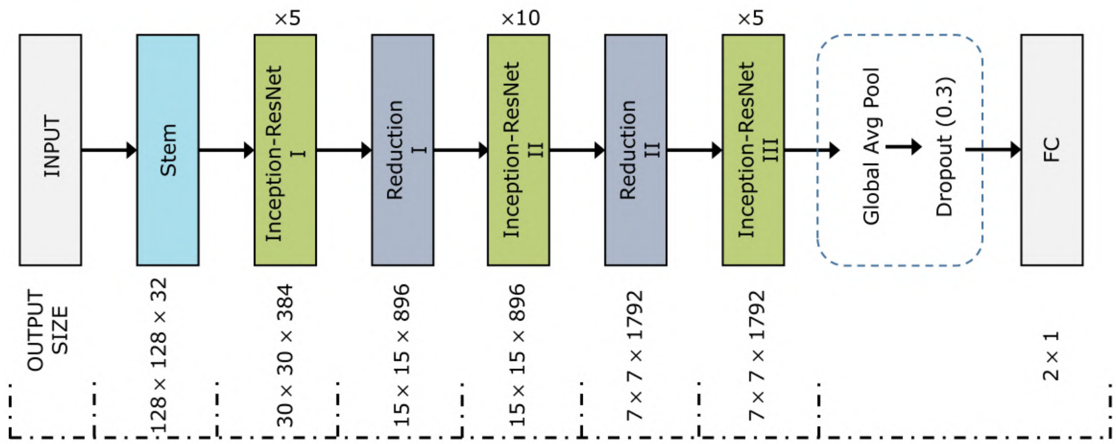

Figure 4-30: Architecture of the inception-ResNet. Abbreviations: FC—fully connected layer, Global Avg Pool—global average pooling. Source: [Wamriew et al., 2022b].

4.4.6 Neural Network Training and Validation

Before training, a random sample of 1000 events and 1000 noise data together with their corresponding labels were reserved for testing the neural network after training. The remaining 38,000 samples were split as follows: 26,600 for training and 11,400 for validation purposes. The labels were the horizontal (x) and the vertical (z)

offsets of the microseismic event sources from the receiver. To solve the regression problem, the noise labels were all initialized with zeros. The training data were input into the network in batches of sizes of 32. This batch size was arrived at after conducting several trials with a variety of sizes. The tests revealed that while larger batches sped up the training process of the neural network, they significantly reduced the generalization performance of the network. On the other hand, smaller batch sizes considerably increased the training time of the neural network without significant improvements on its convergence. A batch size of 32 was the optimum. While the architecture of our neural network deals effectively with the problem of vanishing gradients by use of the skip connections, it is still susceptible to overfitting due to its complexity. To avoid overfitting, the following measures were taken:

(i) A validation dataset comprising of 30% samples randomly picked from the overall dataset was reserved to assess the performance of the neural network after every epoch of training.

(ii) A dropout layer of 30% was introduced just before the fully-connected layer to set 30% of its input data to zero.

(iii) During training, the performance of the network on the validation dataset was tracked at every epoch and its weights saved only if there was improvement.

(iv) An early-stopping call was introduced to stop the training of the network if there was no improvement in its performance for 20 epochs in a row.

The mean squared error (MSE) loss function was used to train the neural network and its weights updated using the Adam algorithm Kingma and Ba [2014]. Both models were trained on a GeForce GTX 1080 Ti GPU running on 64 cores. The ResNet model trained for 11.8 h and 289 epochs while the Inception-ResNet model trained for 7.2 h for 294. Figure 4-31 shows the metrics training and validation loss and mean absolute errors. The training loss measures the performance of the model on the training dataset while the validation loss measures the performance of the model on the validation dataset.

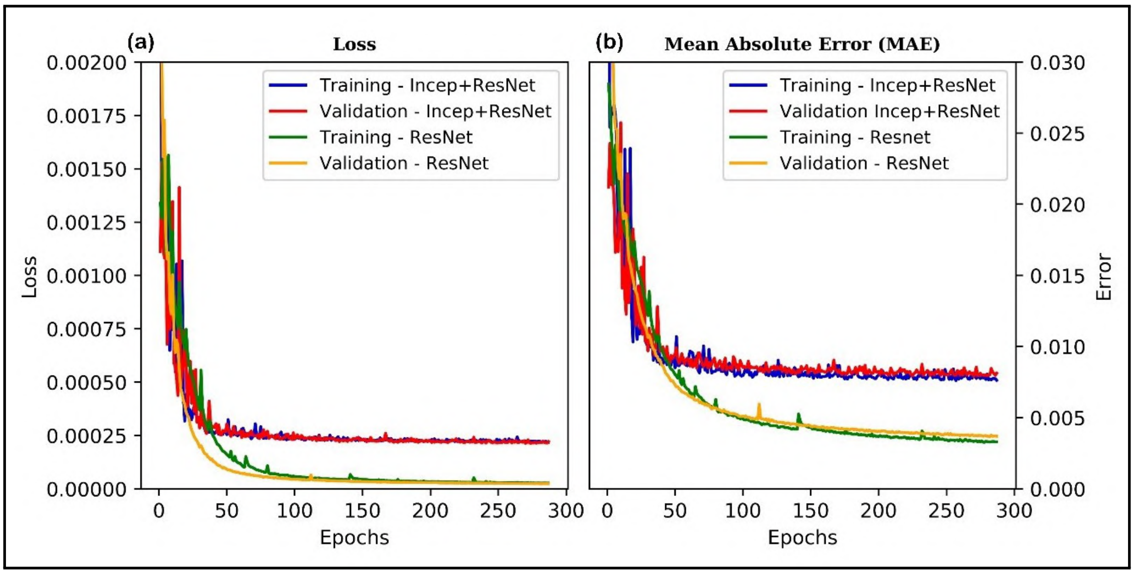

Figure 4-31: Training and validation metrics for both the ResNet and inception-ResNet models: (a) training and validation loss; (b) training and validation mean absolute errors. Source: [Wamriew et al., 2022b].

4.4.7 Results

The results of evaluating the trained neural network on the test dataset as well as its application to the field data are reported in this section.

4.4.7.1 Evaluation of the Trained Neural Network

After training the networks, the test dataset comprised of 2000 samples (1000 microseismic events and 1000 noise samples) was used to evaluate their performances. Figure 4-32 shows the correlation plot for the predictions (inverted data) versus the ground-truth (synthetic data) events.

As can be seen in both plots, the neural network model correctly distinguished between the noise and microseismic events. The noise was located at the origin (since all noise was labeled with zeros for regression purposes). The Pearson's product moment correlation coefficient for the predictions and ground-truth values of the x and z coordinates for the Inception-ResNet model was 0.996 and 0.998, respectively, while that of the ResNet model was 0.998 and 0.999 for x and z, respectively, as evident in both plots in Figure 4-32 and Figure 4-33. This indicates that the predictions are strongly correlated to the ground-truth values and hence are reliable.

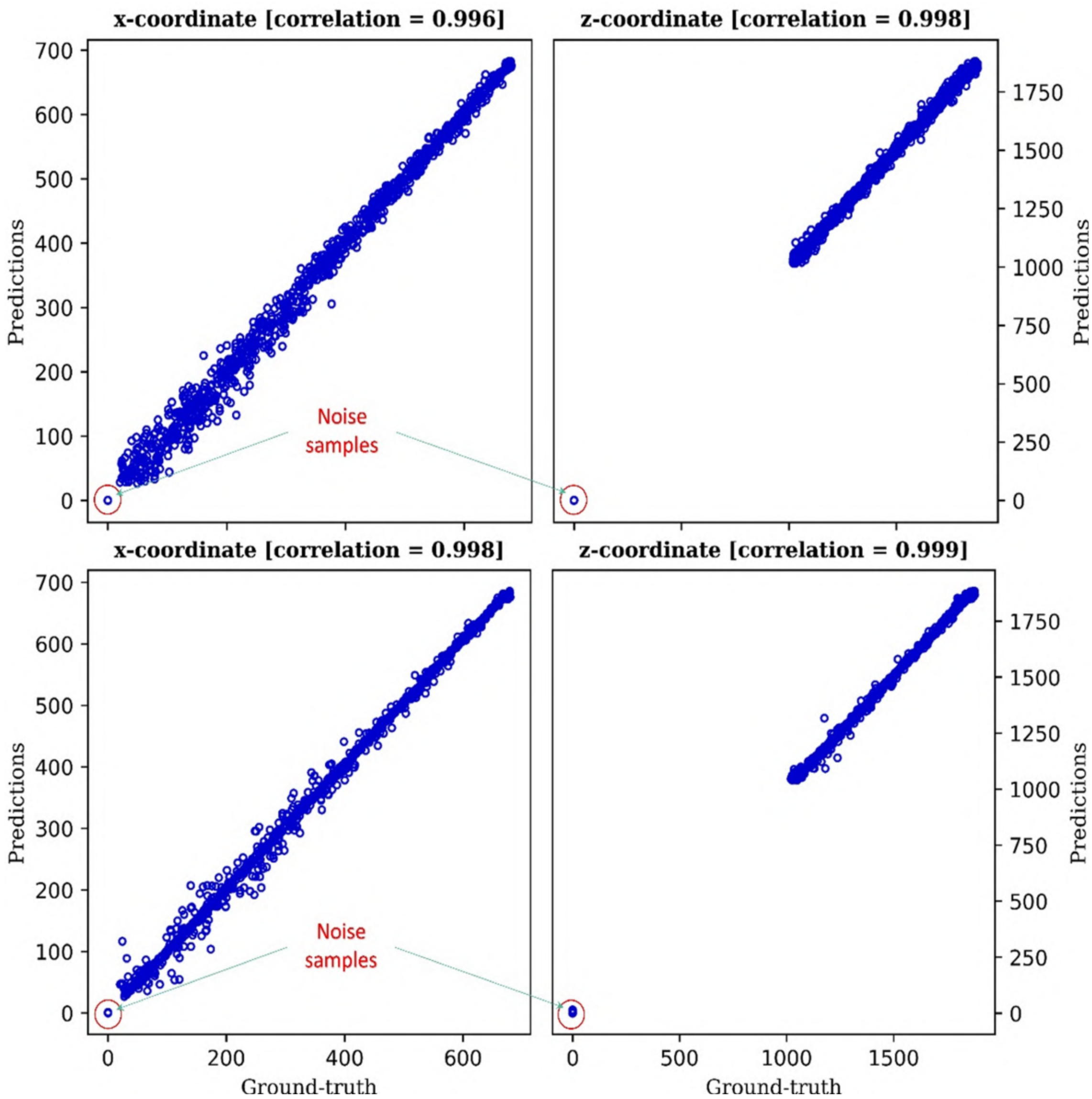

Figure 4-32: Correlation plot of the predicted versus ground-truth events. The dots at the origin of both plots are the noise samples. The wide gap in the right plot is because the minimum depth of the microseismic events was 1050 m. Top row: Inception-ResNet output. Bottom row: ResNet output. Pearson correlation coefficient is indicated in the subtitle of each plot. The same correlation plots are shown in Figure 4-33 after the removal of noise samples from the plots. Source: [Wamriew et al., 2022b].

The ResNet model showed a better correlation than the Inception-ResNet model. In Figure 4-33, we only plotted the output of the ResNet model after the removal of the noise samples.

To measure the trained model's performance on data that it had not seen before, we performed a statistical analysis of the disparity between the predicted and

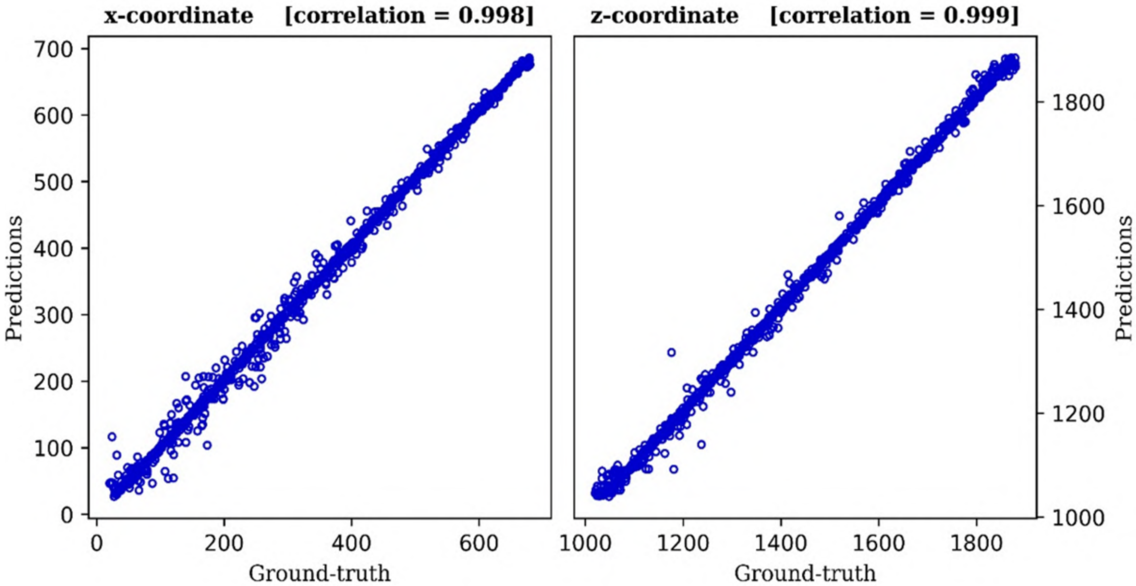

Figure 4-33: Correlation plot of the predicted versus ground-truth microseismic events after the exclusion of noise samples from the test dataset. Source: [Wamriew et al., 2022b].

ground-truth values. Figure 4-34 shows a plot of the errors versus the ground-truth values for the 1000 microseismic events in the test dataset. The errors here were the differences between the predicted event locations and the ground-truth values. From the plots, it is evident that the errors were centered around zero with a few extreme values, as can be seen in the plots in Figure 4-34.

A 2-D section view projection of 150 randomly selected events from the test dataset alongside the inverted (predicted) events is shown in Figure 4-35. The locations of the predicted events closely matched the benchmark data with minor or no discrepancies in certain cases, as can be seen from the plot. In addition, the distribution of the microseismic events can be seen to spread out in definite patterns, possibly mimicking the fracture network of the reservoir.

The calculated statistics for the disparities between the prediction and ground-truth values support the results obtained in Figure 4-33 and Figure 4-34, confirming the robustness of the neural network approach. Table 4.6 presents a summary of the findings. The mean absolute percentages errors (MAPE) in the event locations using the ResNet model were 2.21 and 0.614 for the lateral distance (x) and depth (z) locations, respectively, with the corresponding standard deviations of 11.8 m

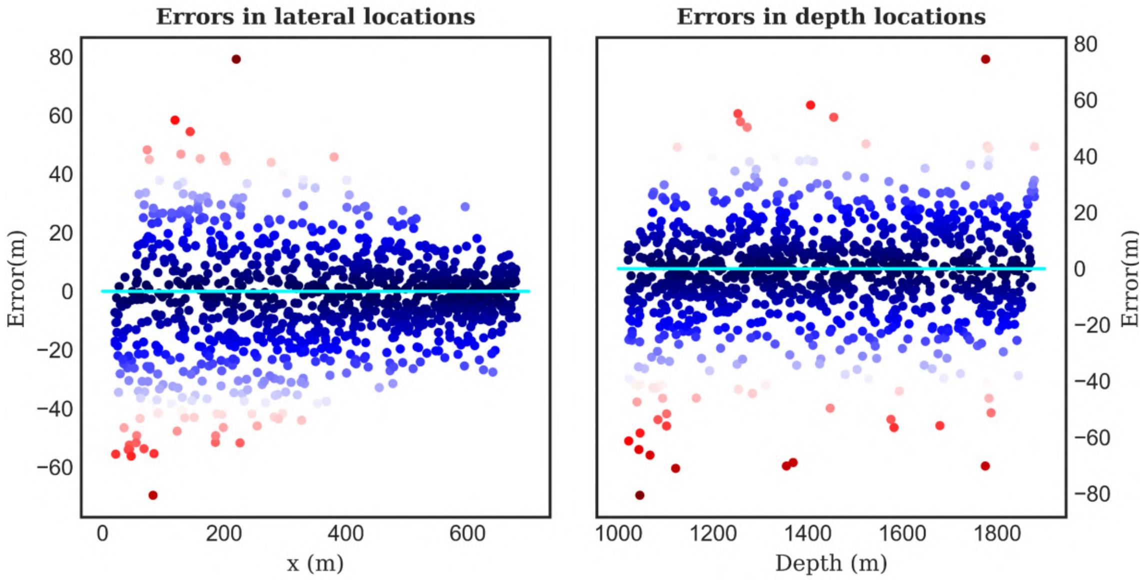

Figure 4-34: Errors in the locations of the microseismic events. Dark to medium blue are within two standard deviations from the mean, while red is more than two standard deviations from the mean. The events underlying the cyan line had no errors. Source: [Wamriew et al., 2022b].

and 12.0 m.

Table 4.6: summary of the statistical analysis of the uncertainty between the predictions and ground-truth values for the two deep CNNs implemented.

Error	MAPE (%)		Standard Deviations (m)	
Network	ResNet	Incep + ResNet	ResNet	Incep + ResNet
Distance (x)	2.21	3.39	11.8	16.6
Depth (z)	0.61	0.79	12.0	16.1

We observed that the mean absolute errors in depth were minimal in both models, but were more spread out, as evident in the standard deviations. This might be attributed to the high values of the anisotropic parameters used in the velocity models as well as the possible uncertainties in the velocity model. Nevertheless, this is necessary for the practical application of the approach, as a good estimate of the velocity model is crucial for the accurate and verifiable inversion of the event locations. Evidently, the ResNet model outperformed the Inception-ResNet model by a

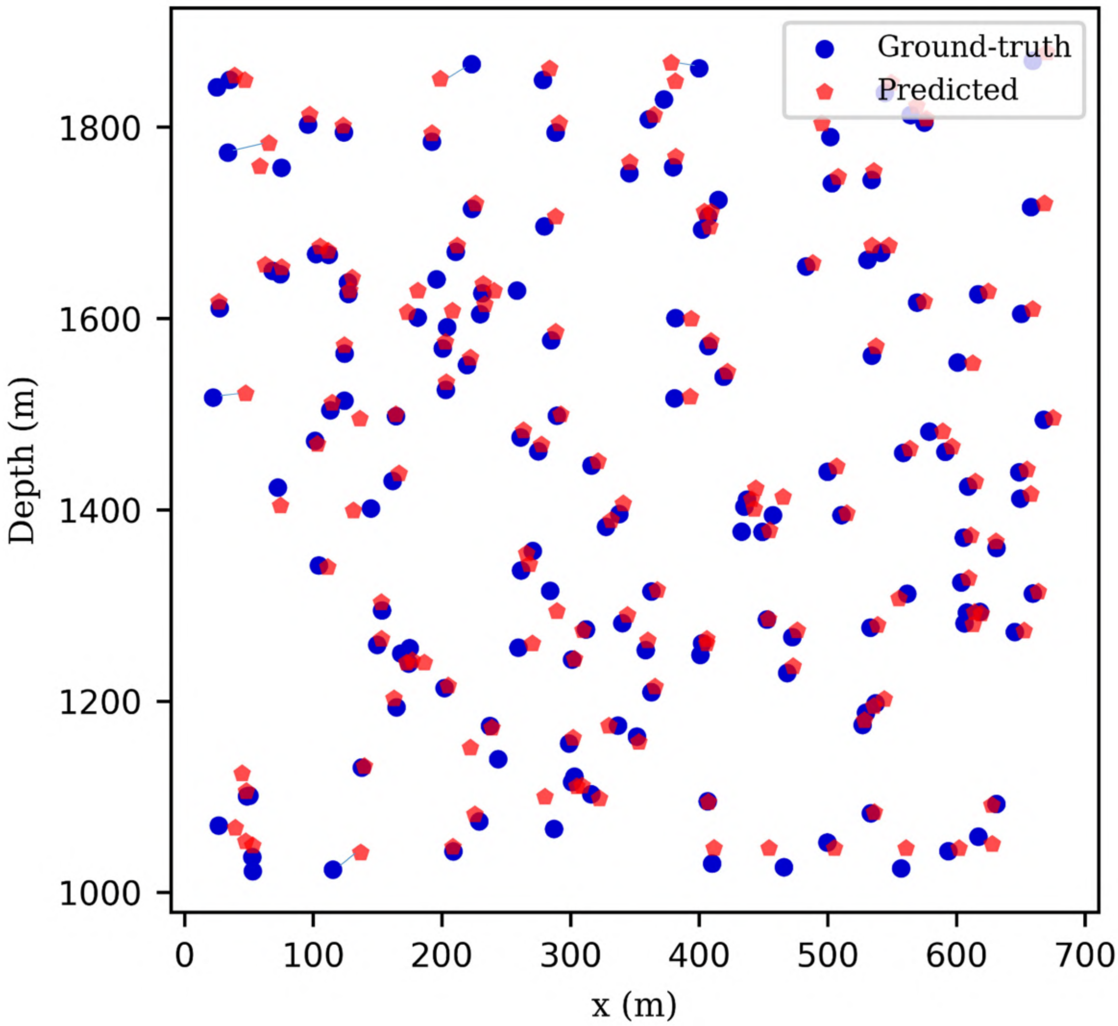

Figure 4-35: 2-D section view project of the predicted versus ground-truth microseismic events. Blue dots represent the ground-truth locations while the red pentagons represent the inverted events. Source: [Wamriew et al., 2022b].

considerably large margin of errors, as seen in Table 4.6. However, the Inception-ResNet architecture is computationally efficient compared to the ResNet.

4.4.7.2 Application to Field Data

Having evaluated the trained neural network on noise contaminated synthetic data, the neural network was applied to automatically identify and locate microseismic events from the field DAS acquired microseismic data from the FORGE project. This dataset comprises fifteen-second SEG-Y data files of the recording of the hydraulic fracture stimulation experiments conducted in the FORGE reservoir during a period of eleven days. A three-hour subset of this dataset from the seventh and eighth cycles of stages 27 and 28 of the stimulation experiments was chosen for inversion with the deep learning model. This subset has been confirmed to contain thirty microseismic events of varying local magnitudes between -1.5 and 0.5.

Each SEG-Y file was split using a one-second length sliding window, giving fifteen samples of 2000 time steps each. The resulting dataset contained 10,800 samples, which were processed as described above in subsection 4.4.3. As a last step, the preprocessed data were amplitude-normalized and converted to greyscale images with pixel sizes of 256 $\times$ 256. Then, the data were fed into the pre-trained ResNet neural network for inversion purposes, as it has been proven to be more robust that the Inception-ResNet model. The neural network detected and located thirty-six microseismic events. Six of these events were new events, which had not been reported before in the events catalogue. Figure 4-36 shows a sample of the new events, while Figure 4-37 shows a 2-D section plot of the inverted event locations.

A human expert using the STA/LTA algorithm with STA and LTA windows of lengths of 0.1 s and 1.0 s, respectively, verified the detected events, as shown in Figure 4-38.

4.4.8 Discussion

Microseismic monitoring and analysis has proven to be a valuable screening tool for reservoir characterization, assisting in the calibration and verification of fracture models as well as inferring fracture height, extent, and orientation from wellbore characterization data. In particular, existing fracture properties of a new play as well as the presence of sweet spots in the vicinity of the existing fractures can be well-understood through the analysis of microseismic data. The information gathered during the real-time analysis of microseismic data is vital as it provides knowledge about the progress of each stage of pumping, which is crucial for onsite decision making.

In the preceding sections, we sought to demonstrate the practicality of employing a deep learning approach to invert microseismic data recorded by the fiber optic DAS technology. Deep learning and DAS are both revolutionary technologies with many benefits to the field of microseismic monitoring and analysis. DAS is rela-

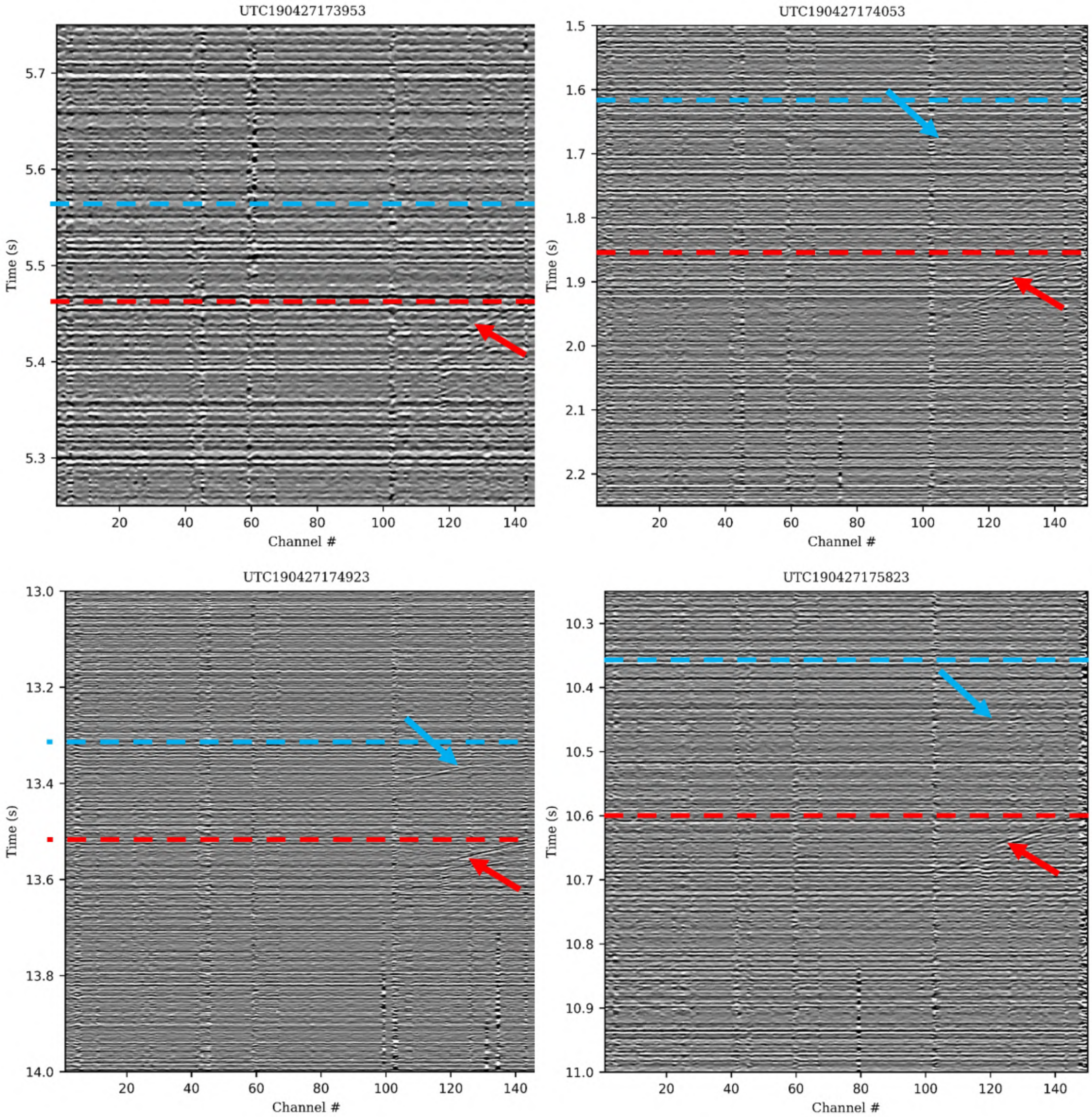

Figure 4-36: Sample of the low magnitude events detected by the CNN but were not in the events catalog. The red lines represent the S-wave arrival times while the cyan shows the estimated P-wave arrivals. Similarly, the cyan and red arrows show the P- and S-waves respectively. Source: [Wamriew et al., 2022b].

tively cheap compared to conventional geophones and accelerometers, is durable, can withstand high downhole pressure, and has a high spatial and temporal resolution, which when fully exploited, provides a detailed mapping of the reservoir. DAS equipment captures massive amounts of data attributable to its high temporal and spatial resolution, making it almost impossible to process and interpret in real-time and poses a challenge for storage space. However, this can be resolved by the use of deep learning. The massive amounts of data that stream in from DAS equipment

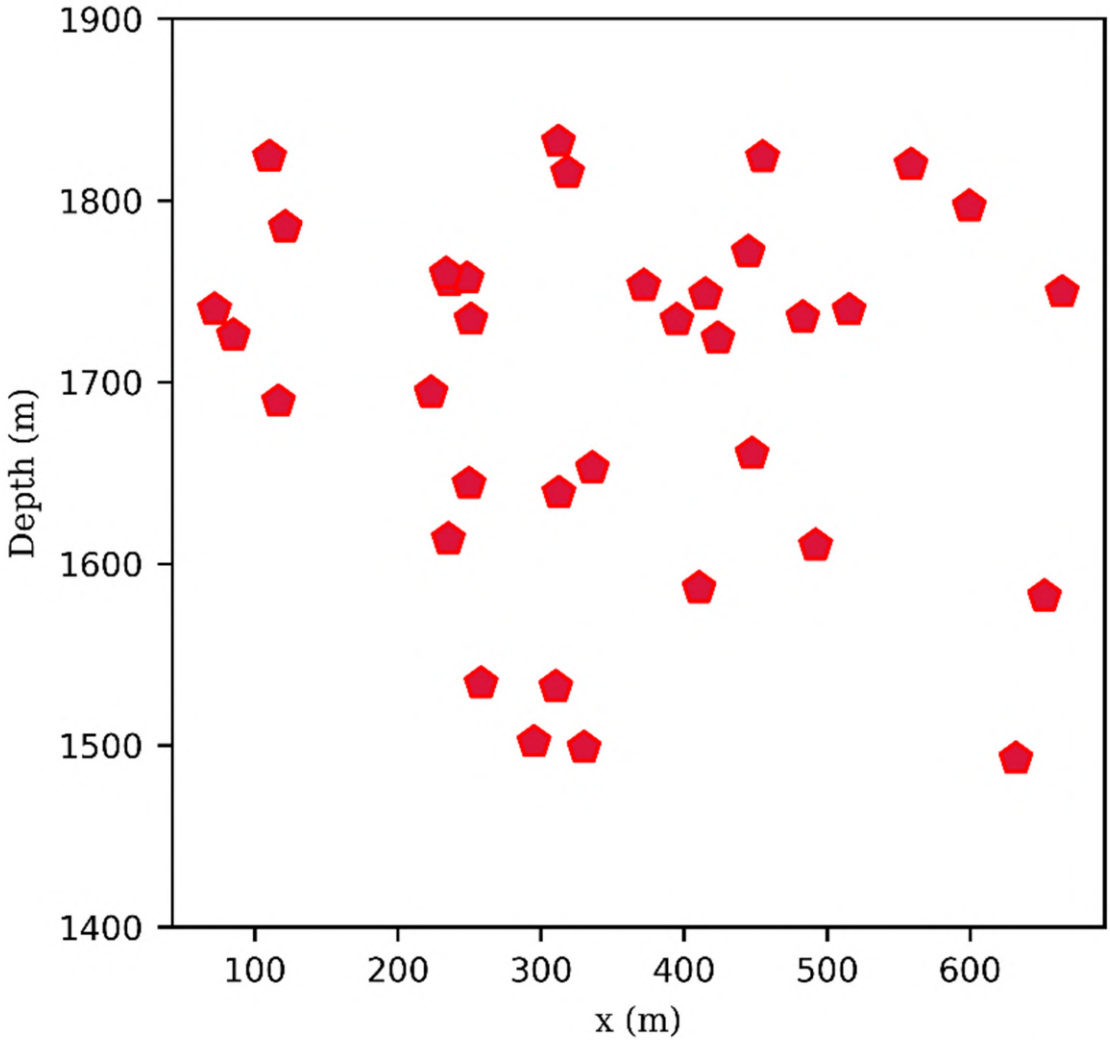

Figure 4-37: 2-D section view projection of the inverted locations of the microseismic events from the FORGE data. Source: [Wamriew et al., 2022b].

make it a perfect candidate for deep learning, which leveraging on this advantage, could be applied to train deep neural network models to detect and perform inversions on microseismic data in real-time during reservoir operations. This could expedite the decision-making process for the optimization of the overall goal of the characterization of the reservoir.

The potential of a deep learning approach for detecting and locating microseismic events from DAS records is demonstrated here by results for both synthetic and field records from the hydraulic fracture stimulation project of the FORGE reservoir in Utah, the United States. The CNN model was able to effectively detect and locate thirty-six microseismic events in the DAS data from stages 27 and 28 of the reservoir

...

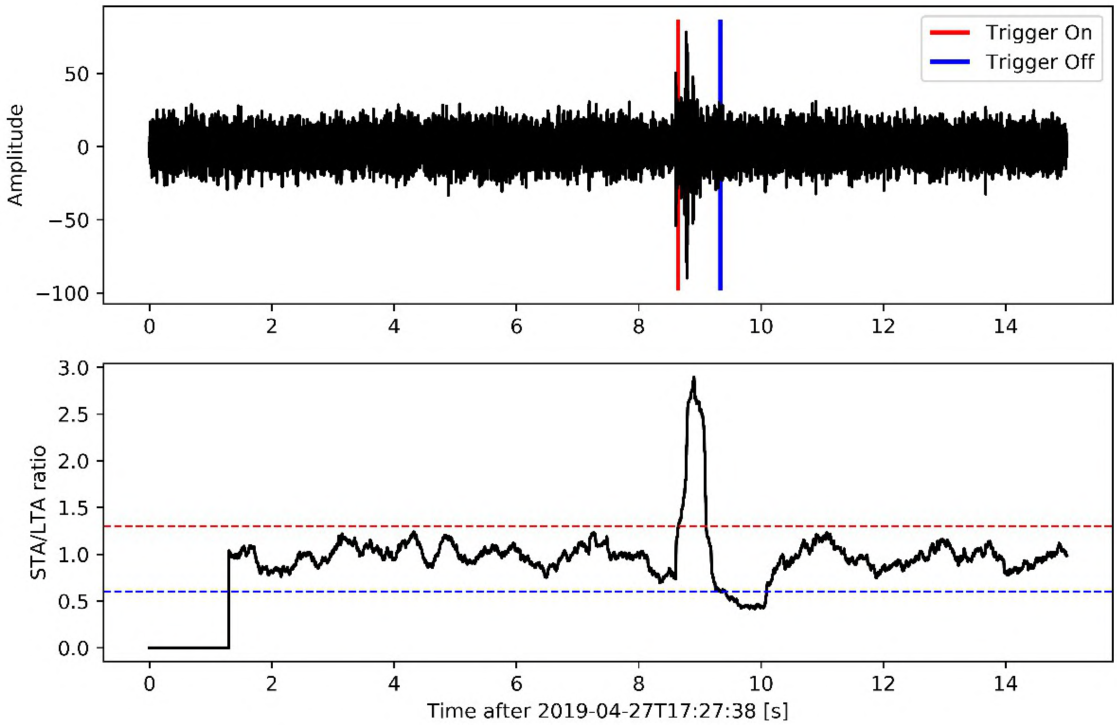

Figure 4-38: An example of the STA/LTA implementation for the detection of microseismic events. **(Top)** Amplitude spectrum of the waveform. **(Bottom)** STA:LTA ratio plot. An event is declared when the STA:LTA ratio exceeds 1.3. Red and Blue dotted lines indicate the thresholds above and below which the trigger is on and off respectively. Source: [Wamriew et al., 2022b].

stimulation, identifying six new weak events that had not been detected previously. The results indicate that the proposed deep learning approach could be applied in real-time during hydraulic fracture stimulation or any other reservoir operations for the simultaneous detection and location of microseismic events or induced seismicity, in the case of passive seismic monitoring.

Integration of the presented method can provide useful information to field engineers that will enable them to make on-the-fly changes to treatment designs, avoid geohazards, locate fault lines that divert fluids and proppants away from the desired fracture zone, and ensure that the spacing between fracture stages is just right. The results of microseismic analysis provide much more information than just the location of individual cracks. The oil and gas industry is learning more about how the reservoir will react to simulated events thanks to the use of microseismic analysis.

This allows them to gain a better understanding of how the reservoir will respond to the situation.

In this study, seismic raytracing was used to create the training dataset due to its numerical and computational efficiency and versatility. When conducted in a smoothly changing layered medium, ray tracing can yield dependable approximation solutions with adequate levels of precision. However, because it is simply a rough solution to the elastic wave equation, it can only be used in smooth changing media and may provide inaccurate results in singular regions [Červený and Pšenčík, 2011]. For this reason, other robust approaches such as the full waveform inversion and reflectivity methods could be used to generate the training data. In addition, with sufficient computational resources, 3-D velocity models can be used in the forward models, as they can be better constrained than the 1-D models used in this study. The inclusion of well log data could also help to better fine-tune the velocity model and enhance the inversion capability of the neural network in the long run.

Better results could be achieved for the detection of the microseismic events by integrating the proposed approach with well-known conventional algorithms such as template matching and STA/LTA routines, which will enhance the detection threshold of the network, especially in cases when the signal is drowned in noise. For the location of the events, the inclusion of shot/calibration data during training of the network could help to further constrain the network and lower the uncertainties in its prediction. Finally, the integration of 3-C geophone data in addition to DAS could solve the problem of cylindrical symmetry and enable 3-D event location while reducing uncertainty.

4.4.9 Conclusions

In this study, a regression-based deep learning approach for detecting and locating microseismic events from seismic waveforms recorded by DAS equipment is presented. Two deep CNN-type neural networks were implemented and their performances compared. The neural network models were trained, validated, and tested on synthetic data injected with noise from the field data. The ResNet outperformed the Inception-ResNet model and its feasibility was tested on the field microseismic data from the hydraulic fracture stimulation experiment of the FORGE project. The errors in the location results for the ResNet model were 2.21% and 0.61% for x and z, respectively, while for the Inception-ResNet model, they were 3.39% and 0.79% respectively, showing the capability of the proposed deep learning approaches in microseismic data analysis.

The trained neural network can be applied to detect and locate microseismic events in real-time during field operations such as hydraulic fracture stimulation, fluid injection for enhanced oil recovery, and carbon dioxide and hydrogen geosequestration. This will fast-track the field decision making process and in turn optimize the reservoir characterization. A combination of DAS and deep learning for reservoir characterization is revolutionary in the sense that the two approaches complement each other. While DAS records large amounts of data that are almost impossible to process in real-time using conventional routines, deep learning benefits from this since it requires large amounts of data for training and validation. Despite the challenge of single channel recordings, the numerous advantages associated with DAS such as high temporal and spatial resolution, durability, ability to sustain high downhole pressures, and low cost make it a priority choice for microseismic monitoring.

4.5 Moment Tensor Inversion using Deep Learning

In this section, we demonstrate the possibility of use of deep CNN for determining the locations of microseismic events as well as inverting for their moment tensor from single borehole seismic data recorded by 3-C geophones. The work presented in this section has been published in the *SPE* conference proceedings [https://doi.org/10.2118/201925-MS].

Title: Deep Neural Network for Real-Time Location and Moment Tensor inversion of borehole microseismic events induced by hydraulic fracturing.

Coauthors: Marwan Charara and Evgenii Maltsev.

4.5.1 Abstract

Locations and source mechanisms of microseismic events are very crucial for understanding the fracturing behavior and evolution of stress fields within the reservoir and hence facilitates the detection of hydraulic fracture growth and estimation of the stimulated reservoir volume (SRV). In the classic workflow, there are two main methods for locating microseismic events with a calibrated fixed velocity model: grid search and linear inversion. The grid search is very stable; can find a global minimum and does not need initial event locations. However, it is computationally intensive and its resolution depends on the grid size, hence, it is not suitable for real-time monitoring. On the other hand, although the linear inversion method is quite fast, the inversion may be pushed into a local minimum by thin shale layers and large velocity contrasts leading to false locations. The source mechanisms of the located events, which provide information about the magnitudes, modes and orientations of the fractures, are obtained through moment tensor inversion of the recorded waveforms. In this paper, we propose a deep neural network approach to solve the above challenges, in real-time, and increase the efficiency and accuracy of location and moment tensor inversion of microseismic events, induced during hydraulic fracturing. Location of microseismic events was considered as a multi-dimensional and non-linear regression problem and a multi-layer two-dimensional (2D) convolutional

neural network (CNN) was designed to perform the inversion. The source mechanisms of the microseismic events were inverted using a multi-head one-dimensional (1D) CNN. The neural networks were trained using synthetic microseismic events with low signal to noise ratio (SNR) to imitate field data. The overall results indicate that both the 2D CNN and 1D CNN models are capable of learning the relationship between the events locations and source mechanisms and the waveform data to a high degree of precision compared to classical methods. Both the event location and source mechanism errors are less than few percent. Deep learning offers a number of benefits for automated and real-time microseismic event location and moment tensor inversion, including least preprocessing, continuous improvement in performance as more training data is obtained, as well as low computational cost.

4.5.2 Forward Modeling

4.5.2.1 Model set-up

We considered a horizontally layered weak-anisotropic model with the P-wave velocity (v_{p0}), S-wave velocity (v_{s0}) and densities ρ as shown in Figure 1. Such a model represents the vast majority of geological structures of shale, usually encountered during hydraulic fracturing. The top boundaries of the layers are located at depths of 2000 m, 2300 m, and 2700 m below the surface respectively. The bottom shale layer of the model was the target for hydraulic fracturing stimulation. Table 4.7 gives the details of the seismic parameters of the 2D model presented in Figure 4-39.

Table 4.7: Velocity model for used in the forward model. The weak anisotropic parameters were obtained from Thomsen [1986]. A visual representation of the model is shown in Figure 4-39

					Thomsen parameters		
Layer number	**Top depth** (m)	$\mathbf{v_{p0}}$**(m/s)**	$\mathbf{v_{s0}}$**(m/s)**	ρ**(kg/m^3)**	ϵ	δ	γ
1	1000	3200	1900	1700	0.195	-0.220	0.180
2	2000	3300	1950	1790	0.110	-0.035	0.255
3	2300	3900	2300	1900	0.055	-0.035	0.255
4	2700	3800	2200	1820	0.030	0.045	0.030

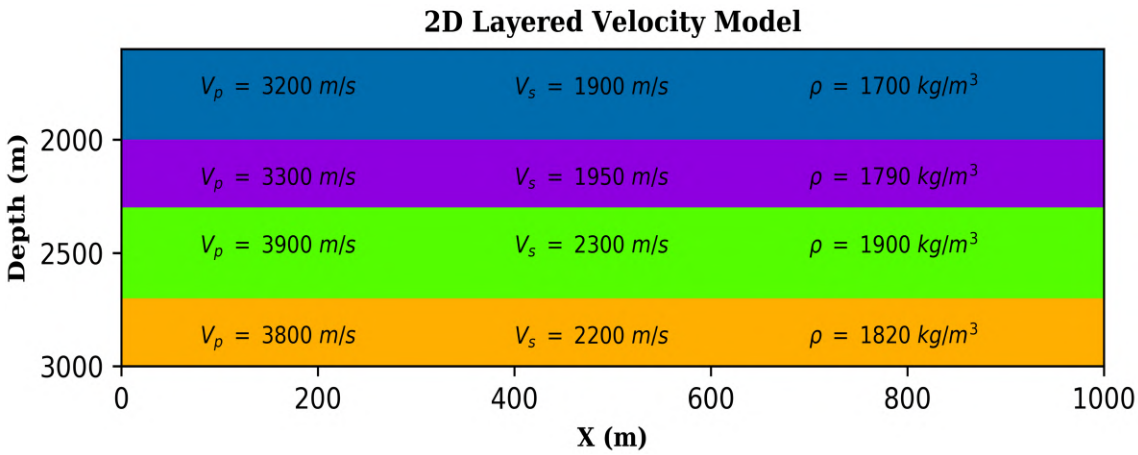

Figure 4-39: Velocity model used in the forward modeling to produce synthetic seismograms by ray tracing. Source: [Wamriew et al., 2020].

Using the velocity model presented in Figure 4-39, we considered a hypothetical deep-downhole array consisting of 24 three-component (3-C) receivers spaced equally at 20 m intervals from a depth of 2060 m downwards in a vertical monitoring well set 300 m from the treatment well. The x (Easting) and y (Northing) coordinates of the receivers were fixed in the middle of the grid at 500 m and 500 m respectively. We defined five frac positions along the horizontal section of the treatment well, at a depth of 2950 m below the surface as shown in Figure 4-40a. For each frac position, we generated 400 random microseismic events with varying moment magnitudes, strikes, dips and rakes (slips). The events source parameters were randomly sampled within the ranges given by Table 4.8.

Table 4.8: Range of label parameters for the focal mechanisms of the microseismic events.

Parameter	**Range**
Strike (ϕ)	-180 – 180 degrees
Dip (δ)	0 – 90 degrees
Rake (γ)	0 – 360 degrees
Moment magnitude (M_0)	-2.7 – 0 Nm

The locations of the event were then sampled uniformly within a $1000m \times 1000m \times 1500m$ box centered on the grid about the receivers as shown in Figure 4-40a.

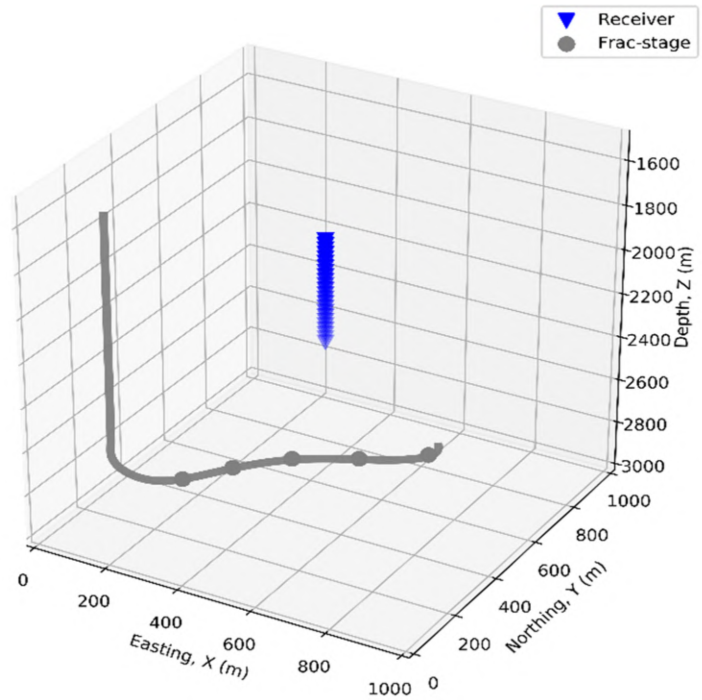

(a) Borehole - Receiver Set-up

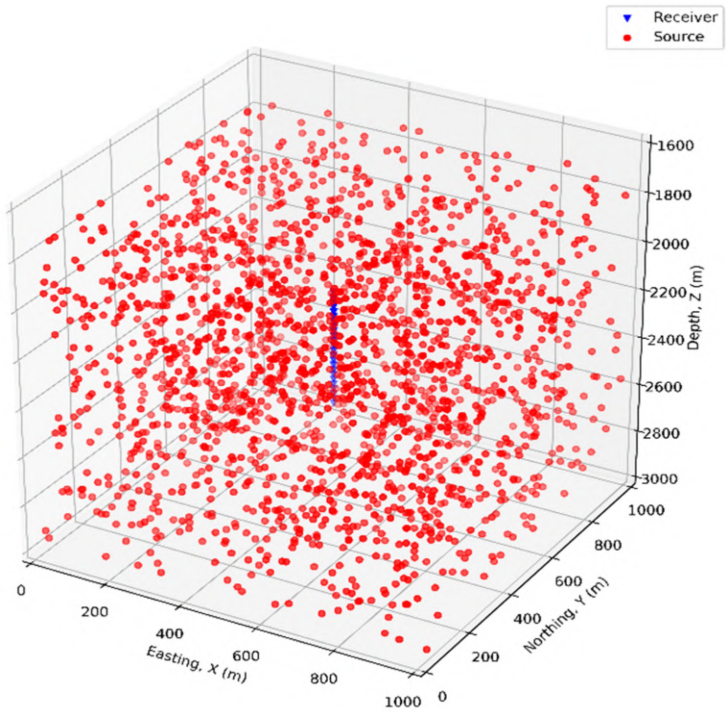

(b) Random Microseismic Events

Figure 4-40: 3-D view of the microseismic acquisition geometry used to generate synthetic data. **(a)** The grey line represents the treatment well while the blue triangles the 3-C receivers in a monitoring well. The frac stages are marked with the round gray dots on the treatment well. **(b)** Microseismic events randomly generated from the five shots during hydraulic fracture treatment. The red dots are events locations while blue triangles are the 3-C receivers. Adopted from [Wamriew et al., 2020].

The source mechanisms for each event is described by a moment tensor, $\mathbf{M}$, decomposed into isotropic (ISO), compensated linear vector dipole (CLVD), and double couple (DC) components (Equation 3.15). The shear part of the source mechanism is also described by strike, dip and rake angles and scalar moment. To encompass all possible source mechanisms, the fraction of each component is sampled uniformly, and the moment tensor is then rotated with a random orthogonal matrix.

4.5.2.2 Ray tracing and synthetic data

Having set up the model and acquisition geometry as described above and demonstrated in Figure 4-39 and Figure 4-40, we performed dynamic raytracing to compute both travel-times and amplitudes of the direct P-, SV- and SH-waves for each event (Equation 4.1).

We performed 20 experiments with this arrangement and generated 40,000 microseismic events. A Ricker wavelet with a 60 Hz dominant frequency was loaded onto each point source, and synthetic seismograms computed for each event. The data was recorded at a millisecond-sampling interval for a duration of up to 0.6 seconds. Figure 4-41a displays sample original waveform traces from a single event recorded on 3-C receivers. The plots in Figure 4-41 show the traces in a window between 50 and 300 milliseconds.

In order to test the stability of the inversion in the presence of noise, and to imitate field data, we contaminated the ray-traced amplitudes with Gaussian noise with SNR ratio of given by Equation 4.3.

The resulting seismograms of the same event in Figure 4-41a are shown in Figure 4-41b. The addition of noise drowns the P-wave arrival making it challenging to identify it (e.g. in Figure 4-41b middle and right plots). This is the usual scenario encountered in microseismic monitoring.

4.5.3 Dealing with overfitting in Deep Learning

In deep learning, the goal is always to approximate the relationship between the input values and the output values. However, deep neural networks more often face the problem of overfitting due to their adaptability in memorizing the peculiar

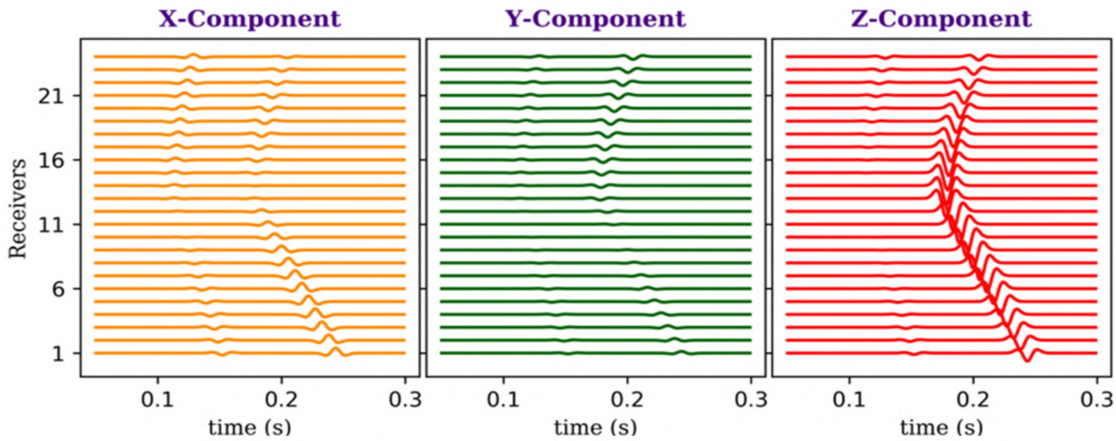

(a) Noise-free seismograms

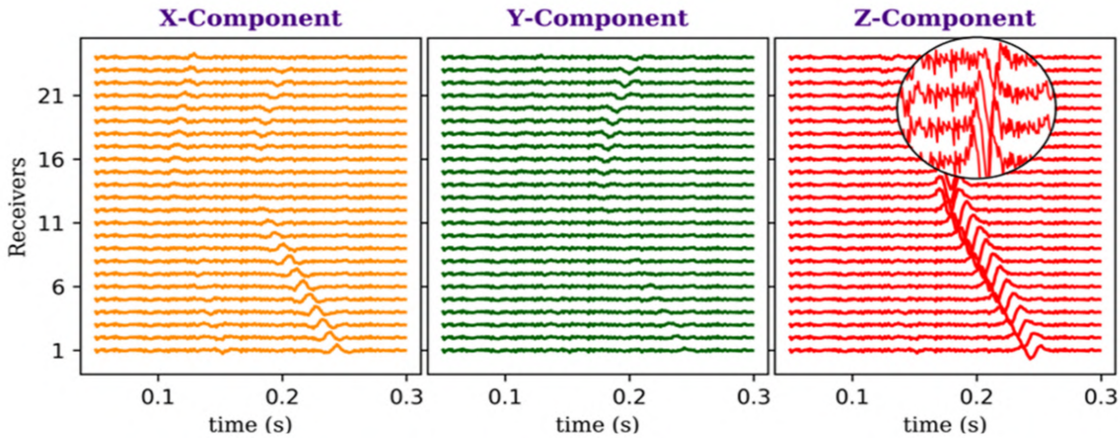

(b) Noise contaminated seismograms

Figure 4-41: **(a)** Sample 3-C synthetic seismograms of an event recorded by the receivers in the borehole. **(b)** Noise contaminated seismogram of the same event. A zoom has been made on the Z-component to give a clear picture of the noise level in the data. The waveforms are sampled at an interval of 1 ms for a duration of 0.6s and are plotted for a window of 0.05 – 0.3 seconds. Source: [Wamriew et al., 2020].

patterns in the training dataset rather than generalizing to unseen data. In order to avoid this pitfall, regularization methods, such as, *L2*-regularization may be used. It is important to note that regularization only reduces the generalization error of the network but not its training error. Since we are dealing with a regression problem, we seek to minimize the mean squared error loss function, which is a function of θ, given by Equation 4.5:

$$L_{train}(\theta) = \frac{1}{N}\sum_{i=1}^{N}(x_i - \bar{x}_i)^2, \tag{4.5}$$

where θ, indicates all the weights in the neural network.

Instead of directly using the loss function L, we add a regularization term to the objective function to obtain:

$$\min L(\theta) = L_{train}(\theta) + \Omega(\theta), \tag{4.6}$$

where $\Omega(\theta)$ is the regularization term and is given by:

$$\Omega(\theta) = \|\theta\|_2^2. \tag{4.7}$$

This addition of constraints to the original loss function ensures that the weights of the neural network do not grow too large, because if it does, it would increase the overall value of the regularized loss function, consequently increasing the training loss of the network. The addition of the regularization term is very important as it prevents the model from driving the training error to zero, and therefore helps deal with overfitting of the data.

Other methods of dealing with overfitting include reducing the complexity (capacity) of the network so that it only focuses on the useful patterns that minimize the loss function. Another approach is to include a dropout layer, which serves to randomly eliminate certain output features of a layer by setting them to null.

In this study, all the aforementioned three approaches were adopted.

4.5.4 Dataset Preparation

One of the advantages of using CNNs is the fact that they do not require extensive data preprocessing, since the filters, through convolution operations, are able to learn even complex features in the given dataset. This is invaluable as it preserves the integrity of the data, since each step in data processing introduces uncertainty. Thus, we performed minimal preprocessing during the data preparation.

Two sets of data were prepared; one set for the location of microseismic events and the other set for moment tensor inversion. The datasets were prepared from the 40,000 seismograms obtained by forward modelling (discussed in subsection 4.5.2).

Each seismogram has a length of 631 sample steps and contains 24 traces, each from a channel of a single receiver. Hence, each seismogram is a tensor of dimensions $631 \times 24 \times 3$. This forms a perfect candidate for convolutional neural networks because the seismograms can be treated as any 2-D RGB images with the third dimension, in this case, the component, corresponding to the depth of the image.

For each seismogram, we performed mean normalization by obtaining the mean amplitude of traces and subtracting it from the individual trace amplitudes and then dividing the difference by the absolute maximum amplitude minus the minimum amplitude. This is necessary to enhance the performance (convergence) of the neural network algorithm. The labels for the location dataset were the three spatial coordinates (x, y, and z) of the hypocenter of the microseismic events, while for moment tensor inversion dataset; the labels were the strike, dip, rake and moment magnitudes of the events.

Having prepared both the features and label datasets for the location of the events and moment tensor inversion, we split the datasets into two parts for training and validation, and testing purposes. In doing so, 90% of the seismograms were set aside for training and validation of the model while the remaining 10% were reserved for testing.

4.5.5 Inversion

In order to accomplish the goals of this study, we used two distinct neural networks for each task. For the task of locating the hypocenter of the microseismic events, we employed a 2-D CNN while a triple-head 1D CNN was used for the moment tensor inversion task. Both the models were built in Keras running on TensorFlow backend. In the following sections, we discuss each network in details.

4.5.5.1 The 2D CNN Model

We used a 2D CNN model to perform the task of locating the hypocenters of microseismic events. The dataset prepared in the section above was used. The seismograms were sorted into three different components (X, Y and Z), according to the components of the receivers and then used as the input to the CNN model. The input volume was a 3D tensor of shape $631 \times 24 \times 3$.

We designed a CNN model with thirty one layers comprising of the input layer, seven convolution layers, seven normalization and non-linear (ReLu) activation layers, seven maximum pooling layers, one fully connected layer and one regression (linear) layer. Figure 4-42 shows the architecture of the CNN model.

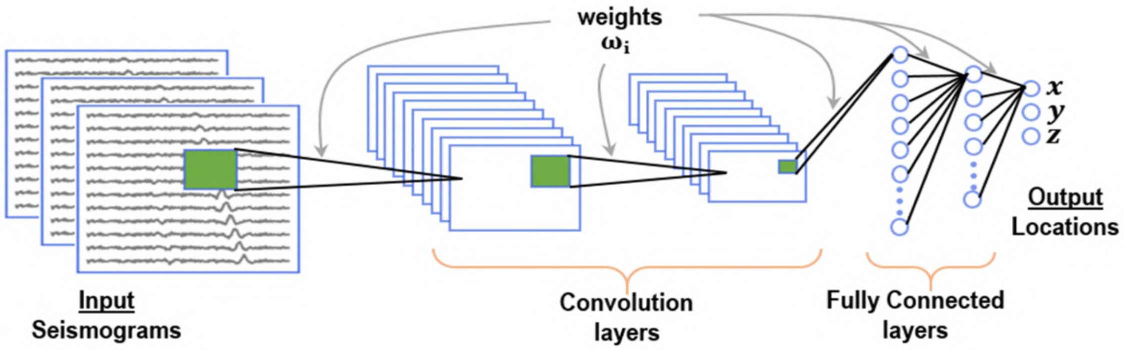

Figure 4-42: Convolutional neural network architecture. The network takes as input seismograms and outputs the locations (x, y,z) of the microseismic events. The network is elaborately discussed in subsubsection 4.5.5.1. Source: [Wamriew et al., 2020].

The input matrix was zero padded before convolution to preserve the original size. Each of the seven 2D convolution layers comprised of 16, 16, 64, 64, 64, 16 and16 kernels (filters), respectively from first to last. Each kernel had spatial dimensions (height and width) of $3{\times}3$ with the depth corresponding to the number of filters in each layer. The convolutional layers were 'fired' using the ReLu non-linear activation function due to its computational efficiency as already discussed above. Every convolutional layer was followed by a two-dimensional maximum pooling layer (MaxPooling2D) with spatial dimensions of 2×1 for the first four layers and 2×2 for the final three layers, and a stride of 2. The purpose of the maximum pooling is to reduce every four (or two – for the case of 2×1) neurons to a single neuron, by taking the highest value between the four (or two). After the last convolution and maximum pooling, the next layer was 'flattened' and added a fully connected layer comprising of 64 nodes and a *ReLu* activation function. This was then followed with the final regression layer comprising of 3 neurons (to match the expected output of the spatial coordinates of locations of the microseismic events) and activated with a linear activation function, which allows the output to take on arbitrary values.

For training of the model, we used the stochastic gradient descent (SGD) learning algorithm, which supports a variety of loss functions and penalties to fit linear regression models. SGD is the best for regression problems with large number of training samples like in our case. We started with an initial learning rate of 0.01 and decreased it with a factor of 10 after every 20 training cycles. To speed up the training, the data was input in minibatches of size 64, after the pilot tests showed that smaller minibatch sizes led to longer training time, with no improvement in model performance, while bigger minibatch sizes compromised the regression accuracy and lowered the performance of the model.

To avoid the risk of overfitting, we implemented three precautionary measures. First, we monitored the performance of the model on the test dataset after each epoch and only saved its weights if there is improvement on its performance on the test dataset. Secondly, we implemented *L2*-regularization (as discussed in subsection 4.5.3), with a regularization factor of 10^{-4}. Finally, we used a validation dataset comprising of 10% randomly sampled data to validate the performance of the network, after every epoch of training. We shuffled both the validation and training data before every epoch. We used the mean squared error (MSE) as the loss function to be minimized. The loss function measures how close the output of the model matches the true values. We trained the model for 700 epochs and achieved the convergence.

4.5.5.2 The triple-head 1-D CNN model

For the resolution of the source mechanisms of the microseismic events, we designed a triple-head 1-D CNN model. The model had three heads, each comprising of 5 convolution layers, each followed with normalization and non-linear (*ReLu*) activation layers, maximum pooling layers and dropout layers. Each of the convolution layers had 16, 64, 128, 64, 16 filters of kernel size 3, respectively from first to last. We applied zero padding to the input matrix before convolution. Like in the previous model, the *ReLu* activation function was used to activate the convolution layers.

A dropout was added after each convolution to reduce the interdependent learning among the neurons, as a first step to deal with overfitting. This was followed with 1-D maximum pooling layers each of 3 strides. The input to each of the three 1-D CNN heads was a matrix of shape 631×24 being a single component of the 3-D seismograms. The outputs from each of the three heads were then concatenated and passed through two fully connected layers with 16 and 8 nodes, respectively. The final layer, the output layer, was a regression layer with 4 nodes to output the inverted strike, dip, rake and moment magnitudes. The rest of the parameters for this model are similar to the 2-D CNN model discussed above.

4.5.6 Results

After training, the performance of each network was evaluated using the independent test dataset consisting of 4000 samples, which the network had not seen before. The evaluation of the event locations is straightforward since the model outputs the source locations in terms of the three spatial coordinates x, y and z. For the resolution of the focal mechanisms, the four crucial source parameters: strike, dip, rake and the moment magnitudes obtained from the neural network are used to compute the full moment tensor. A plot of the predicted parameters obtained from the neural network against the actual parameters (Figure 4-43) reveals a positive correlation for all the seven parameters, illustrating that the neural network is capable of providing full information about the hypocenter as well as the source mechanisms of microseismic events.

In order to get a clear view of the locations of the inverted events with respect to their true locations, we plot three distinct plan view projections of the locations of inverted and the actual events on the local grid (Figure 4-44): East (x) – North (y), East (x) – Depth (z) and North (y) – Depth (z).

From Figure 4-44, it is clear that the locations of the inverted events match almost perfectly the actual events. A comparison of the right and left plots on Figure 4-44 reveals that the deep learning model gives very accurate predictions (inversion) of the depth (z-) coordinate as compared to the lateral (x- and y-) coordinates. Even so, the y-coordinate is better resolved than the x-coordinate. It

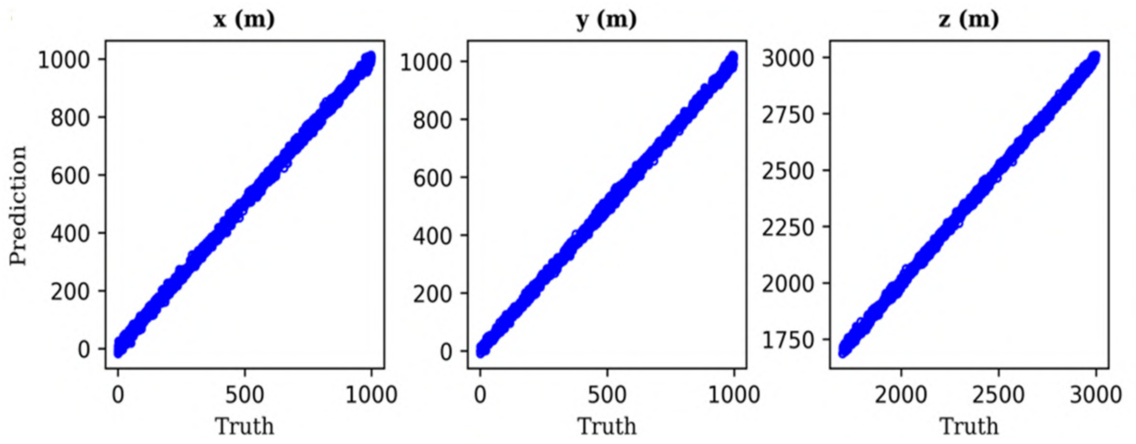

(a)

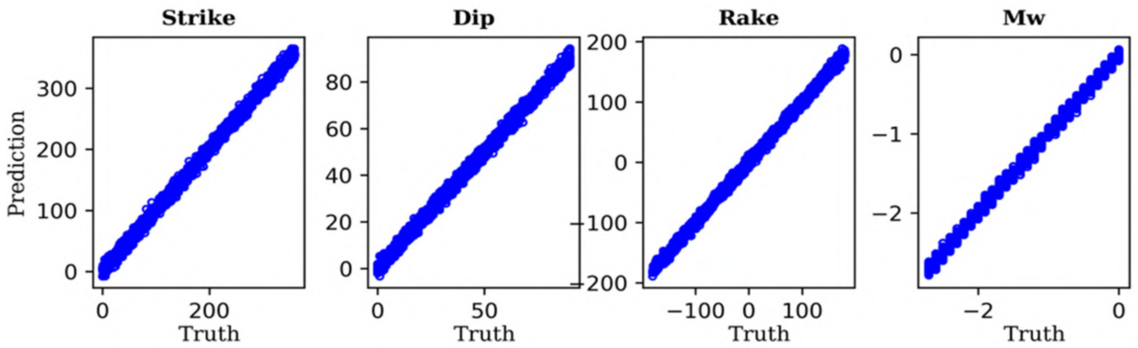

(b)

Figure 4-43: **(a)** Scatter plots of each coordinate location of the microseismic events predicted by the CNN versus its ground-truth value from the test set of synthetic events.**(b)** Scatter plots of the predicted versus the actual source parameters (strike, dip, rake and moment magnitude). A positive correlation between the predicted and true values is evident on each of the seven plots. Source: [Wamriew et al., 2020].

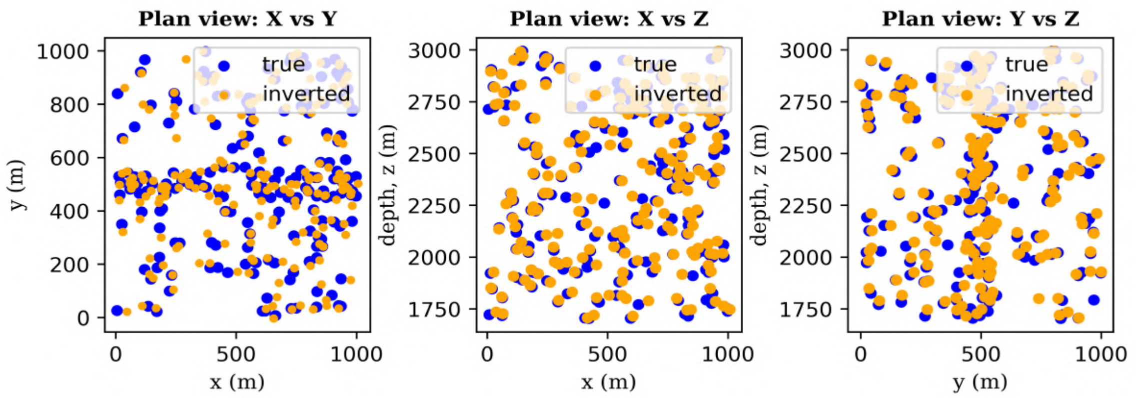

Figure 4-44: 2D plan-view plots showing the locations of the inverted (in orange) versus the ground-truth (in blue) microseismic events. The projections are indicated on the title of each plot. For purposes of clarity, only 200 events are shown on the plots.Source: [Wamriew et al., 2020].

remains a matter of great interest as to why, despite having a uniform grid sampling dimensions, the y-coordinates are better resolved than the x-coordinate.

In order to evaluate the stability of the inverted source mechanisms, we compute the full moment tensors of both the inverted and original microseismic events and plot fault-plane solutions (beach balls) from the moment tensors. These solutions are crucial as they give the orientation of the fault plane that slipped and the slip vector. Figure 4-45 below shows sample beach ball plots computed from both the true (blue) microseismic events and the inverted (orange) events.

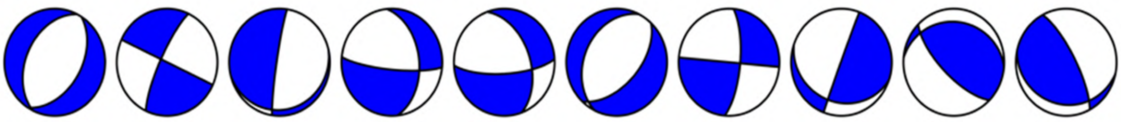

(a) Beachball plots of ground-truth focal mechanisms

(b) Beachball plots of inverted focal mechanisms

Figure 4-45: Sample fault plane solutions of 10 randomly selected events from the test dataset. **(a)** Beachball plots of ground-truth focal mechanisms generated by forward modelling. **(b)** Beachball plots of the inverted focal mechanisms obtained from the neural network. Source: [Wamriew et al., 2020].

As we can see from Figure 4-45, the full moment tensor solution plots match perfectly well, indicating the high precision of the neural network model in performing moment tensor inversion. The events cover the full range of possible faulting associated with microseismicity ranging from normal, strike-slip, to thrust faulting and their possible combinations. A detailed analysis of the fault mechanisms (fault-plane solutions) is beyond the scope of this study, as we only seek to demonstrate that it possible to invert for the focal mechanisms using the CNN approach.

A summary of the complete statistical analysis of the neural network results of all the seven parameters under this study is presented in Figure 4-46. The event location percentage errors for x, y, and z are 1.8%, 1.4% and 0.4% respectively; while the percentage errors for the source parameters are 2.2%, 1.9%, 3.7% and 0.3% for strike, dip, rake and moment magnitudes respectively. With the latter parameters, the computation of the inverted full moment tensor is straightforward. The z-coordinate, dip, and the moment magnitude were the best resolved of the seven parameters, while the x-coordinate and the strike were the least accurate. In general, the overall performances of the neural networks significantly outperforms the human expert using classic routines by a large margin.

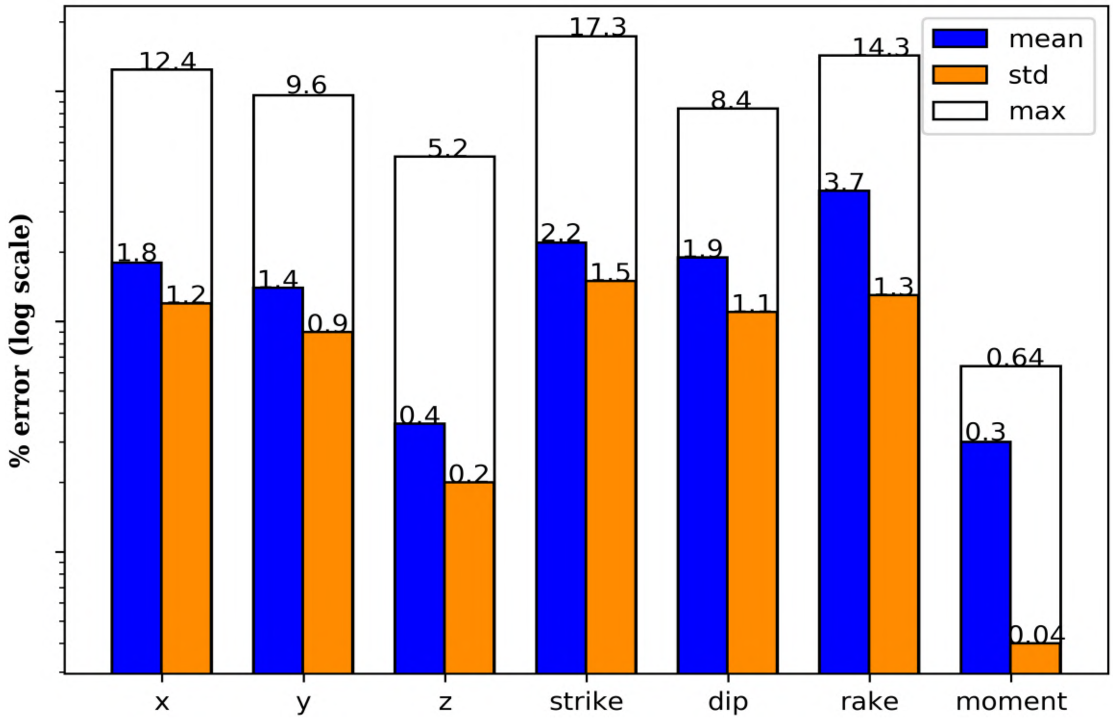

Figure 4-46: Error plot for the seven location and source parameters inverted by deep learning. The vertical scale is logarithmic. Source: [Wamriew et al., 2020].

4.5.7 Conclusion

Two distinct regression CNNs are proposed and their usability validated on the low SNR test dataset similar to field data. The CNN models are capable to learn the relationships between microseismic events (locations and source mechanisms) and the waveform data to a high degree of precision compared to classical methods. The CNN approach has many benefits that make it attractive for real-time monitoring decisions that influence hydraulic fracturing operations. Most importantly, the approach requires minimal preprocessing of data as the model is capable to learn by itself the properties of recorded waveforms to better locate and perform moment tensor inversion of the microseismic events, thereby eliminating uncertainties usually introduced by data handling and processing. Moreover, the performance of the networks can be improved in-real time during training as more training data is obtained. In addition, CNN models are computationally efficient after training; for instance, the entire prediction using the 4000 test samples took only 788 milliseconds on a CPU processor. Future work should assess the effect varying levels of anisotropy on the performance of deep neural networks for location and characterization of the source parameters. Other deep neural network model architectures such as the GoogLeNet, VGGNet and ResNet could be considered. In this study, we adopted the AlexNet model architecture.

"the feeling is less like an ending than just another starting point."

Chuck Palahniuk

Chapter 5

Conclusion

This thesis presents cutting-edge technologies for detecting and locating the hypocenters of induced seismic events, particularly microseismic events, as well as inverting for the source mechanisms and velocity models from microseismic data. The deep learning approach allows for simultaneous detection, location and inversion of the source mechanisms of microseismic events in real-time or semi-real-time, making it attractive for projects such as hydraulic fracture stimulation and CO_2 injection, where it is necessary to make decisions in real-time during operations.

While hypocenter determination is a well-studied topic and continuously improved, by many scholars, velocity errors remain the least understood and the most elusive contributor to the uncertainties in the determined events locations. Throughout this thesis, a unique and robust approach for dealing with the velocity model uncertainties while at the same time, locating and inverting the source mechanisms of microseismic events has been demonstrated. The simultaneous velocity model update during inversion of microseismic data is revolutionary in the sense that it alleviates the uncertainties caused by velocity errors leading to improved accuracy. In section 4.2, the approach is successfully applied to processing downhole microseismic data acquired by 3-C geophone from a single vertical borehole, while section 4.3 demonstrates the same approach applied to field microseismic DAS recordings from FORGE project in Milford, Utah in USA. In both cases, the errors in the inversion results are minimal, as statistically summarized in Figure 4-9 and Figure 4-21, indicating the efficacy of the approach. Further, tests by addition of varying degrees of random noise (subsubsection 4.2.6.1) and perturbation of the anisotropic parameters of the medium (subsubsection 4.2.6.2) confirm stability and robustness of the deep learning inversion approach.

Moment tensor inversion of microseismic data is known to be a daunting task especially because of low SNR nature of microseismic data. In the case of a single vertical borehole, the solid angle subtended by the receivers with respect to the source location is zero, leading to an ill-conditioned inversion. In this study, We have shown that deep learning based moment tensor inversion could provide stable and reliable focal plane solutions. In section 4.5, two regression-based CNNs are used to simultaneously locate hypocenters and invert for source mechanisms of microseismic events from a single borehole straddled with twenty-four 3-C geophones. The neural network output focal plane solutions (i.e strike, dip and rake), from which the moment tensor can be calculated following the procedure in subsection 3.3.1.

Only 3-C geophone data has been considered since it is not possible to perform full moment tensor inversion on single vertical borehole DAS data as it is uni-axial (1-C) in nature. However, due to the present rapid growth in fiber optic DAS technology, there is a high likelihood of development of fiber optic cables capable of recording 3-C microseismic data. There have been proposals of using helical shaped fiber optic cables for this purpose, for example [Kuvshinov, 2015] and [A., 2020], but more research is still needed in that direction.

In a nutshell, deep learning and DAS are both potential emerging technologies in microseismic monitoring and a combination of the two might be game-changing. Because of its high spatial and temporal resolution and physical robustness, DAS has recently become a popular option for acquiring microseismic data. The vast volumes of data generated by DAS sensors, on the other hand, make it extremely difficult to process in real-time or semi-real-time using conventional routines. Deep learning comes into play here as they are data-driven. While there are numerous conventional routines for seismic event detection, location, velocity model and source mechanisms inversion, the deep learning approach is capable of combining and performing all these tasks in real-time and, as a result, is more effective.

Ray tracing was employed to generate the synthetic training datasets used in this thesis due to its speed, numerical accuracy for high frequency waves in smooth media, and computational efficiency, but other methods such as reflectivity or full waveform inversion are also viable.

The technology presented here could help petroleum and mining professionals speed up field decision-making and aid in production optimization. It must, however, be proven through long-term monitoring and testing with data from more complex geological formations.

5.1 Recommendations for future work

The work covered in this thesis and the results obtained are preliminary, and more research into the location and source characterization of induced seismic events using deep learning is required. With each passing day, the rapid increase in computer power – speed and memory – provides new opportunities and capabilities to investigate and implement more complex deep learning algorithms that could further improve the accuracy and stability of inversion of induced seismic data, particularly microseismic data. Microseismic data is rich in information. Thus, more quantitative analysis of the data should be performed in order to extract this information.

Improving the preprocessing and processing workflow appears to be an important step that could improve the quality of microseismic data analysis and interpretation. For this goal, the recently discovered Physics Informed Neural Networks (PINN) and Physics Constrained Neural Networks (PCNN) could be employed. Further, deep learning-based signal processing and noise-attenuation approaches for microseismic applications should be investigated.

Throughout this thesis, the forward models used for the generation of synthetic data have been considered to be vertically transverse isotropic (VTI). In future, other types of anisotropy, e.g, horizontally transverse isotropy (HTI) and tilted transverse isotropy (TTI), should be considered for inversion with deep learning. In addition, the efficacy of the approach should be assessed on more complex geological formations with varying degrees of anisotropy.

Furthermore, the idea of combining well-tested conventional methods with deep learning models should be looked into so that unique neural network models can be made that can handle a wide range of difficult geological formations.

Bibliography

Baird A. Modelling the response of helically wound DAS cables to microseismic arrivals. In *First EAGE Workshop on Fibre Optic Sensing*. European Association of Geoscientists & Engineers, 2020. doi:10.3997/2214-4609.202030019. URL https://doi.org/10.3997%2F2214-4609.202030019.

Sardar Afra and Mohammadali Tarrahi. An efficient EOR screening approach with statistical pattern recognition: Impact of rock/fluid feature selection and extraction. In *Day 4 Thu, May 05, 2016*. OTC, May 2016. doi:10.4043/27272-ms. URL https://doi.org/10.4043/27272-ms.

Babatunde Ajayi, Kirby Walker, John Sink, Kevin Wutherich, and Robert Downie. Using microseismic monitoring as a real time completions diagnostic tool in unconventional reservoirs: Field case studies. In *All Days*. SPE, August 2011. doi:10.2118/148271-ms. URL https://doi.org/10.2118/148271-ms.

Temitope Ajayi, Jorge Salgado Gomes, and Achinta Bera. A review of CO2 storage in geological formations emphasizing modeling, monitoring and capacity estimation approaches. *Petroleum Science*, 16(5):1028–1063, July 2019. doi:10.1007/s12182-019-0340-8. URL https://doi.org/10.1007/s12182-019-0340-8.

K. Aki and P.G. Richards. *Quantitative Seismology*. Geology Seismology. University Science Books, 2002. ISBN 9781891389634.

Keiiti Aki. Generation and propagation of g waves from the niigata earthquake of june 16, 1964. : Part 2. estimation of earthquake moment, released energy, and stress-strain drop from the g wave spectrum. *Bulletin of the Earthquake Research Institute, University of Tokyo*, 44:73–88, July 1966. application/pdf.

Jubran Akram and David W. Eaton. A review and appraisal of arrival-time picking methods for downhole microseismic data. *GEOPHYSICS*, 81(2):KS71–KS91, March 2016. doi:10.1190/geo2014-0500.1. URL https://doi.org/10.1190/geo2014-0500.1.

Jubran Akram, Oleg Ovcharenko, and Daniel Peter. A robust neural network-based approach for microseismic event detection. In *SEG Technical Program Expanded Abstracts 2017*. Society of Exploration Geophysicists, August 2017. doi:10.1190/segam2017-17761195.1. URL https://doi.org/10.1190/segam2017-17761195.1.

Fred Aminzadeh. Reservoir characterization: Fundamental and applications - an overview, December 2021. URL `https://doi.org/10.1002/9781119556237.ch1`.

Colin B. Amos, Pascal Audet, William C. Hammond, Roland Bürgmann, Ingrid A. Johanson, and Geoffrey Blewitt. Uplift and seismicity driven by groundwater depletion in central california. *Nature*, 509(7501):483–486, May 2014. doi:10.1038/nature13275. URL `https://doi.org/10.1038/nature13275`.

Fatai Anifowose, Abdulazeez Abdulraheem, and Abdullatif Al-Shuhail. A parametric study of machine learning techniques in petroleum reservoir permeability prediction by integrating seismic attributes and wireline data. *Journal of Petroleum Science and Engineering*, 176:762–774, May 2019. doi:10.1016/j.petrol.2019.01.110. URL `https://doi.org/10.1016/j.petrol.2019.01.110`.

Adam Baig and Ted Urbancic. Microseismic moment tensors: A path to understanding frac growth. *The Leading Edge*, 29(3):320–324, March 2010. doi:10.1190/1.3353729. URL `https://doi.org/10.1190/2F1.3353729`.

Richard O. Baker, Harvey W. Yarranton, and Jerry L. Jensen. Reservoir characterization methods. In *Practical Reservoir Engineering and Characterization*, pages 349–434. Elsevier, 2015. doi:10.1016/b978-0-12-801811-8.00010-9. URL `https://doi.org/10.1016/b978-0-12-801811-8.00010-9`.

Sudhish Kumar Bakku. *Fracture characterization from seismic measurements in a borehole*. PhD thesis, Massachusetts Institute of Technology, 2015.

S. A. Barrett and G. C. Beroza. An empirical approach to subspace detection. *Seismological Research Letters*, 85(3):594–600, May 2014. doi:10.1785/0220130152. URL `https://doi.org/10.1785/0220130152`.

Maksim Bazulin, Denis Sabitov, and Marwan Charara. Determination of the elastic parameters of a VTI medium from sonic logging data using deep learning. *Computers & Geosciences*, 152:104759, July 2021. doi:10.1016/j.cageo.2021.104759. URL `https://doi.org/10.1016/j.cageo.2021.104759`.

Karianne J Bergen and Gregory C Beroza. Detecting earthquakes over a seismic network using single-station similarity measures. *Geophysical Journal International*, 213(3):1984–1998, March 2018. doi:10.1093/gji/ggy100. URL `https://doi.org/10.1093/gji/ggy100`.

Marton Berta, Frank Dethlefsen, Markus Ebert, Dirk Schäfer, and Andreas Dahmke. Geochemical effects of millimolar hydrogen concentrations in groundwater: An experimental study in the context of subsurface hydrogen storage. *Environmental Science & Technology*, 52(8):4937–4949, March 2018. doi:10.1021/acs.est.7b05467. URL `https://doi.org/10.1021/acs.est.7b05467`.

Piyali Bhanja, Arindam Modak, and Asim Bhaumik. Porous organic polymers for CO 2 storage and conversion reactions. *ChemCatChem*, 11(1):244–257, September 2018. doi:10.1002/cctc.201801046. URL https://doi.org/10.1002/cctc.201801046.

Gary Binder and Ali Tura. Convolutional neural networks for automated microseismic detection in downhole distributed acoustic sensing data and comparison to a surface geophone array. *Geophysical Prospecting*, 68(9):2770–2782, September 2020. doi:10.1111/1365-2478.13027. URL https://doi.org/10.1111/1365-2478.13027.

Thomas Braun, Simone Cesca, Daniela Kühn, Araksi Martirosian-Janssen, and Torsten Dahm. Anthropogenic seismicity in italy and its relation to tectonics: State of the art and perspectives. *Anthropocene*, 21:80–94, March 2018. doi:10.1016/j.ancene.2018.02.001. URL https://doi.org/10.1016/j.ancene.2018.02.001.

Mugdim Bublin. Machine learning for distributed acoustic sensors, classic versus image and deep neural networks approach, 2019. URL https://arxiv.org/abs/1904.11546.

Joseph A Bucaro, Henry D Dardy, and Edward F Carome. Optical fiber acoustic sensor. *Applied optics*, 16(7):1761–1762, 1977.

Enrico Caffagni, David W. Eaton, Joshua P. Jones, and Mirko van der Baan. Detection and analysis of microseismic events using a matched filtering algorithm (MFA). *Geophysical Journal International*, page ggw168, May 2016. doi:10.1093/gji/ggw168. URL https://doi.org/10.1093/gji/ggw168.

Yunpeng Cai, Jihui Ma, Wenfa Yan, Wenyi Zhang, and Yuhang An. Aircraft detection using phase-sensitive optical-fiber otdr. *Sensors*, 21(15):5094, 2021.

P. Calio, M. DE Panfilis, D. DI FILIPPO, L. MARCELLI, and M. C. SPADEA. TERREMOTI DELLA VAL PADANA DEL 15-16 MAGGIO 1951. *Annals of Geophysics*, 9(1), February 2012. doi:10.4401/ag-5594. URL https://doi.org/10.4401/ag-5594.

J. P. Castagna, M. L. Batzle, and R. L. Eastwood. Relationships between compressional-wave and shear-wave velocities in clastic silicate rocks. *GEOPHYSICS*, 50(4):571–581, April 1985. doi:10.1190/1.1441933. URL https://doi.org/10.1190%2F1.1441933.

Vlastislav Červený. *Seismic Ray Theory*. Cambridge University Press Cambridge, 2001.

Vlastislav Červený and Ivan Pšenčík. Seismic, ray theory. In *Encyclopedia of Solid Earth Geophysics*, pages 1244–1258. Springer Netherlands, 2011. doi:10.1007/978-90-481-8702-7_53. URL https://doi.org/10.1007/978-90-481-8702-7_53.

Dian Chen, Qingwen Liu, and Zuyuan He. Phase-detection distributed fiber-optic vibration sensor without fading-noise based on time-gated digital OFDR. *Optics Express*, 25(7):8315, March 2017. doi:10.1364/oe.25.008315. URL https://doi.org/10.1364/oe.25.008315.

Mengmeng Chen, Bo Li, Ali Masoudi, Daniel Bull, and Janice M Barton. Distributed optical fibre sensor for strain measurement of reinforced concrete beams. In *2020 International Conference on Intelligent Transportation, Big Data & Smart City (ICITBS)*, pages 102–107. IEEE, 2020.

Ting Chen and Lianjie Huang. Optimal design of microseismic monitoring network: Synthetic study for the kimberlina CO2 storage demonstration site. *International Journal of Greenhouse Gas Control*, 95:102981, April 2020. doi:10.1016/j.ijggc.2020.102981. URL https://doi.org/10.1016/j.ijggc.2020.102981.

Dennis Cooke, Arcangelo Sena, Greg O'Donnell, Tetang Muryanto, and Vaughn Ball. What is the best seismic attribute for quantitative seismic reservoir characterization? In *SEG Technical Program Expanded Abstracts 1999*. Society of Exploration Geophysicists, January 1999. doi:10.1190/1.1820829. URL https://doi.org/10.1190/1.1820829.

Brian Culshaw and Alan Kersey. Fiber-optic sensing: A historical perspective. *Journal of Lightwave Technology*, 26(9):1064–1078, May 2008. doi:10.1109/jlt.0082.921915. URL https://doi.org/10.1109/jlt.0082.921915.

George E. Dahl, Tara N. Sainath, and Geoffrey E. Hinton. Improving deep neural networks for LVCSR using rectified linear units and dropout. In *2013 IEEE International Conference on Acoustics, Speech and Signal Processing*. IEEE, May 2013. doi:10.1109/icassp.2013.6639346. URL https://doi.org/10.1109/icassp.2013.6639346.

Thomas M. Daley, Barry M. Freifeld, Jonathan Ajo-Franklin, Shan Dou, Roman Pevzner, Valeriya Shulakova, Sudhendu Kashikar, Douglas E. Miller, Julia Goetz, Jan Henninges, and Stefan Lueth. Field testing of fiber-optic distributed acoustic sensing (DAS) for subsurface seismic monitoring. *The Leading Edge*, 32(6):699–706, June 2013. doi:10.1190/tle32060699.1. URL https://doi.org/10.1190%2Ftle32060699.1.

James H Diaz. The influence of global warming on natural disasters and their public health outcomes. *American journal of disaster medicine*, 2(1):33–42, 2007.

David E. Diller and Stephen P. Gardner. Comparison of simultaneous downhole and surface microseismic monitoring in the williston basin. In *SEG Technical Program Expanded Abstracts 2011*. Society of Exploration Geophysicists, January 2011. doi:10.1190/1.3627487. URL https://doi.org/10.1190/1.3627487.

Douglas S. Dreger, Sean R. Ford, and William R. Walter. Source analysis of the crandall canyon, utah, mine collapse. *Science*, 321(5886):217–217, July 2008. doi:10.1126/science.1157392. URL https://doi.org/10.1126/science.1157392.

Jing Du, Ulrich Zimmer, and Norm Warpinski. Fault-plane solutions from moment tensor inversion for microseismic events using single-well and multi-well data. *CSEG Recorder*, 36(08):22–29, October 2011. URL https://csegrecorder.com/articles/view/fault-plane-solutions-from-moment-tensor-inversion-for-microseismic-events.

G. Duncan and G. Beresford. Median filter behaviour with seismic data1. *Geophysical Prospecting*, 43(3):329–345, April 1995. doi:10.1111/j.1365-2478.1995.tb00256.x. URL https://doi.org/10.1111/j.1365-2478.1995.tb00256.x.

Paul S. Earle and Peter M. Shearer. Characterization of global seismograms using an automatic-picking algorithm. *Bulletin of the Seismological Society of America*, 84(2):366–376, April 1994. doi:10.1785/bssa0840020366. URL https://doi.org/10.1785/bssa0840020366.

David W. Eaton. *Passive Seismic Monitoring of Induced Seismicity*. Cambridge University Press, April 2018. doi:10.1017/9781316535547. URL https://doi.org/10.1017/9781316535547.

David W. Eaton, Mirko van der Baan, Brad Birkelo, and Jean-Baptiste Tary. Scaling relations and spectral characteristics of tensile microseisms: evidence for opening/closing cracks during hydraulic fracturing. *Geophysical Journal International*, 196(3):1844–1857, January 2014. doi:10.1093/gji/ggt498. URL https://doi.org/10.1093/2Fgji/2Fggt498.

Jo Eidsvik, Per Avseth, Henning Omre, Tapan Mukerji, and Gary Mavko. Stochastic reservoir characterization using prestack seismic data. *GEOPHYSICS*, 69(4):978–993, July 2004. doi:10.1190/1.1778241. URL https://doi.org/10.1190/1.1778241.

Leo Eisner, B. J. Hulsey, Peter Duncan, Dana Jurick, Heigl Werner, and William Keller. Comparison of surface and borehole locations of induced seismicity. *Geophysical Prospecting*, 58(5):809–820, August 2010. doi:10.1111/j.1365-2478.2010.00867.x. URL https://doi.org/10.1111/j.1365-2478.2010.00867.x.

Leo Eisner, Michael Thornton, and Jessica Griffin. Challenges for microseismic monitoring. In *SEG Technical Program Expanded Abstracts 2011*. Society of Exploration Geophysicists, January 2011. doi:10.1190/1.3627491. URL https://doi.org/10.1190/1.3627491.

William L. Ellsworth. Injection-induced earthquakes. *Science*, 341(6142), July 2013. doi:10.1126/science.1225942. URL https://doi.org/10.1126/science.1225942.

A. F. Emanov, A. A. Emanov, A. V. Fateev, E. V. Leskova, E. V. Shevkunova, and V. G. Podkorytova. Mining-induced seismicity at open pit mines in kuzbass (bachatsky earthquake on june 18, 2013). *Journal of Mining Science*, 50(2):224–228, March 2014. doi:10.1134/s1062739114020033. URL `https://doi.org/10.1134/s1062739114020033`.

Energy and Geoscience Institute at the University of Utah. Utah forge: High-resolution das microseismic data from well 78-32 [data set], 2019. URL `https://gdr.openei.org/submissions/1185`. Accessed: 2022-05-01.

Jiang Fengqing, Zhu Cheng, Mu Guijin, Hu Ruji, and Meng Qingxia. Magnification of flood disasters and its relation to regional precipitation and local human activities since the 1980s in xinjiang, northwestern china. *Natural Hazards*, 36(3): 307–330, 2005.

Mulugeta C. Fenta, David K. Potter, and János Szanyi. Fibre optic methods of prospecting: A comprehensive and modern branch of geophysics. *Surveys in Geophysics*, 42(3):551–584, March 2021. doi:10.1007/s10712-021-09634-8. URL `https://doi.org/10.1007%2Fs10712-021-09634-8`.

María R. Fernández-Ruiz, Marcelo A. Soto, Ethan F. Williams, Sonia Martin-Lopez, Zhongwen Zhan, Miguel Gonzalez-Herraez, and Hugo F. Martins. Distributed acoustic sensing for seismic activity monitoring. *APL Photonics*, 5(3):030901, March 2020a. doi:10.1063/1.5139602. URL `https://doi.org/10.1063%2F1.5139602`.

María R. Fernández-Ruiz, Marcelo A. Soto, Ethan F. Williams, Sonia Martin-Lopez, Zhongwen Zhan, Miguel Gonzalez-Herraez, and Hugo F. Martins. Distributed acoustic sensing for seismic activity monitoring. *APL Photonics*, 5(3): 030901, March 2020b. doi:10.1063/1.5139602. URL `https://doi.org/10.1063/1.5139602`.

María R. Fernández-Ruiz, Miguel Soriano-Amat, Hugo F. Martins, Vicente Durán, Sonia Martin-Lopez, and Miguel Gonzalez-Herraez. High resolution distributed optical fiber sensing using time-expanded phase-sensitive reflectometry. *Frontiers in Sensors*, 2, January 2022. doi:10.3389/fsens.2021.804556. URL `https://doi.org/10.3389/fsens.2021.804556`.

D. C. Finfer, V.. Mahue, S. V. Shatalin, T. R. Parker, and M.. Farhadiroushan. Borehole flow monitoring using a non-intrusive passive distributed acoustic sensing (DAS). In *All Days*. SPE, October 2014. doi:10.2118/170844-ms. URL `https://doi.org/10.2118/170844-ms`.

Gillian R. Foulger, Miles P. Wilson, Jon G. Gluyas, Bruce R. Julian, and Richard J. Davies. Global review of human-induced earthquakes. *Earth-Science Reviews*, 178:438–514, March 2018. doi:10.1016/j.earscirev.2017.07.008. URL `https://doi.org/10.1016/j.earscirev.2017.07.008`.

Raphaël Garcia, Philippe Lognonné, and Xavier Bonnin. Detecting atmospheric perturbations produced by venus quakes. *Geophysical Research Letters*, 32(16), 2005.

Sergio Roberto Mata García, Javier Carrasco Hernández, and José L. Ortiz López. Seismic characterisation using artificial intelligence algorithms for rock property distribution in static modeling. In *Day 3 Thu, September 19, 2019*. SPE, September 2019. doi:10.2118/196647-ms. URL https://doi.org/10.2118/196647-ms.

G. H. F. Gardner, L. W. Gardner, and A. R. Gregory. FORMATION VELOCITY AND DENSITY—THE DIAGNOSTIC BASICS FOR STRATIGRAPHIC TRAPS. *GEOPHYSICS*, 39(6):770–780, December 1974. doi:10.1190/1.1440465. URL https://doi.org/10.1190%2F1.1440465.

David Gee, Andrew Sowter, Alessandro Novellino, Stuart Marsh, and Jon Gluyas. Monitoring land motion due to natural gas extraction: Validation of the intermittent SBAS (ISBAS) DInSAR algorithm over gas fields of north holland, the netherlands. *Marine and Petroleum Geology*, 77:1338–1354, November 2016. doi:10.1016/j.marpetgeo.2016.08.014. URL https://doi.org/10.1016/j.marpetgeo.2016.08.014.

Steven J. Gibbons and Frode Ringdal. The detection of low magnitude seismic events using array-based waveform correlation. *Geophysical Journal International*, 165(1):149–166, April 2006. doi:10.1111/j.1365-246x.2006.02865.x. URL https://doi.org/10.1111/j.1365-246x.2006.02865.x.

Pablo J. González, Kristy F. Tiampo, Mimmo Palano, Flavio Cannavó, and José Fernández. The 2011 lorca earthquake slip distribution controlled by groundwater crustal unloading. *Nature Geoscience*, 5(11):821–825, October 2012. doi:10.1038/ngeo1610. URL https://doi.org/10.1038/ngeo1610.

Vladimir Grechka and Werner M. Heigl. *Microseismic Monitoring*. Society of Exploration Geophysicists, January 2017. doi:10.1190/1.9781560803485. URL https://doi.org/10.1190/1.9781560803485.

Vladimir Grechka, Zhao Li, and Bo Howell. Relative location of microseismic events with multiple masters. *GEOPHYSICS*, 81(4):KS149–KS158, July 2016. doi:10.1190/geo2015-0445.1. URL https://doi.org/10.1190/geo2015-0445.1.

Harsh K Gupta. A review of recent studies of triggered earthquakes by artificial water reservoirs with special emphasis on earthquakes in koyna, india. *Earth-Science Reviews*, 58(3-4):279–310, October 2002. doi:10.1016/s0012-8252(02)00063-6. URL https://doi.org/10.1016/s0012-8252(02)00063-6.

Mostafa Hadavand, Paul Carmichael, Ali Dalir, Maximo Rodriguez, Diogo F. Silva, and Clayton V. Deutsch. Integration of 4d seismic in steam-assisted-gravity-drainage reservoir characterization. *SPE Reservoir Evaluation & Engineering*, 22(01):203–218, September 2018. doi:10.2118/191359-pa. URL https://doi.org/10.2118/191359-pa.

Helge H Haldorsen and Eivind Damsleth. Challenges in reservoir characterization: Geohorizons. *AAPG bulletin*, 77(4):541–551, 1993.

William Harbert, Angela Goodman, Richard Spaulding, Igor Haljasmaa, Dustin Crandall, Sean Sanguinito, Barbara Kutchko, Mary Tkach, Samantha Fuchs, Charles J. Werth, Theodore Tsotsis, Laura Dalton, Kristian Jessen, Zhuofan Shi, and Scott Frailey. CO2 induced changes in mount simon sandstone: Understanding links to post CO2 injection monitoring, seismicity, and reservoir integrity. *International Journal of Greenhouse Gas Control*, 100:103109, September 2020. doi:10.1016/j.ijggc.2020.103109. URL `https://doi.org/10.1016/j.ijggc.2020.103109`.

D Harris. Subspace detectors: Theory. Technical report, Lawrence Livermore National Lab.(LLNL), Livermore, CA (United States), July 2006. URL `https://doi.org/10.2172/900081`.

Arthur Hartog, Bernard Frignet, Duncan Mackie, and Mike Clark. Vertical seismic optical profiling on wireline logging cable. *Geophysical Prospecting*, 62(4):693–701, May 2004. doi:10.1111/1365-2478.12141. URL `https://doi.org/10.1111%2F1365-2478.12141`.

Arthur H. Hartog. *An Introduction to Distributed Optical Fibre Sensors*. CRC Press, May 2017. doi:10.1201/9781315119014. URL `https://doi.org/10.1201%2F9781315119014`.

Kaiming He, Xiangyu Zhang, Shaoqing Ren, and Jian Sun. Deep residual learning for image recognition. In *2016 IEEE Conference on Computer Vision and Pattern Recognition (CVPR)*. IEEE, June 2016. doi:10.1109/cvpr.2016.90. URL `https://doi.org/10.1109/cvpr.2016.90`.

Zuyuan He and Qingwen Liu. Optical fiber distributed acoustic sensors: A review. *Journal of Lightwave Technology*, 39(12):3671–3686, June 2021. doi:10.1109/jlt.2021.3059771. URL `https://doi.org/10.1109/jlt.2021.3059771`.

Niklas Heinemann, Mark Wilkinson, R. Stuart Haszeldine, Anthony E. Fallick, and Gillian E. Pickup. CO2 sequestration in a UK north sea analogue for geological carbon storage. *Geology*, 41(4):411–414, April 2013. doi:10.1130/g33835.1. URL `https://doi.org/10.1130/g33835.1`.

Pablo D. Hernandez, Jaime A. Ramirez, and Marcelo A. Soto. Deep-learning-based earthquake detection for fiber-optic distributed acoustic sensing. *Journal of Lightwave Technology*, 40(8):2639–2650, April 2022. doi:10.1109/jlt.2021.3138724. URL `https://doi.org/10.1109/jlt.2021.3138724`.

Pablo D. Hernández, Jaime A. Ramírez, and Marcelo A. Soto. Deep-learning-based earthquake detection for fiber-optic distributed acoustic sensing. *J. Lightwave Technol.*, 40(8):2639–2650, Apr 2022. URL `http://opg.optica.org/jlt/abstract.cfm?URI=jlt-40-8-2639`.

R. B. Herrmann. A student's guide to the use of p and s wave data for focal mechanism determination. *Seismological Research Letters*, 46(4):29–39, October 1975. doi:10.1785/gssrl.46.4.29. URL `https://doi.org/10.1785/2Fgssrl.46.4.29`.

Xuri Huang, Laurent Meister, and Rick Workman. Reservoir characterization by integration of time-lapse seismic and production data. In *All Days*. SPE, October 1997. doi:10.2118/38695-ms. URL `https://doi.org/10.2118/38695-ms`.

Peter G. Hubbard, James Xu, Shenghan Zhang, Matthew Dejong, Linqing Luo, Kenichi Soga, Carlo Papa, Christian Zulberti, Demetrio Malara, Fabio Fugazzotto, Francisco Garcia Lopez, and Chris Minto. Dynamic structural health monitoring of a model wind turbine tower using distributed acoustic sensing (DAS). *Journal of Civil Structural Health Monitoring*, 11(3):833–849, May 2021. doi:10.1007/s13349-021-00483-y. URL `https://doi.org/10.1007/s13349-021-00483-y`.

T. S. Hudson, A. F. Baird, J. M. Kendall, S. K. Kufner, A. M. Brisbourne, A. M. Smith, A. Butcher, A. Chalari, and A. Clarke. Distributed acoustic sensing (DAS) for natural microseismicity studies: A case study from antarctica. *Journal of Geophysical Research: Solid Earth*, 126(7), July 2021. doi:10.1029/2020jb021493. URL `https://doi.org/10.1029/2020jb021493`.

Robert Hull, Robert Meek, Hector Bello, and Douglas Miller. Exploration of case histories of DAS fiber-based microseismic and strain data, monitoring horizontal hydraulic stimulations using various tools to highlight physical deformation processes (part a). In *Proceedings of the 5th Unconventional Resources Technology Conference*. American Association of Petroleum Geologists, 2017. doi:10.15530/urtec-2017-2695282. URL `https://doi.org/10.15530/2Furtec-2017-2695282`.

Fantine Huot and Biondo Biondi. "machine learning algorithms for automated seismic ambient noise processing applied to DASacquisition". In *SEG Technical Program Expanded Abstracts 2018*. Society of Exploration Geophysicists, August 2018. doi:10.1190/segam2018-w20-03.1. URL `https://doi.org/10.1190/segam2018-w20-03.1`.

Fantine Huot, Robert G. Clapp, and Biondo L. Biondi. Detecting local earthquakes via fiber-optic cables in telecommunication conduits under stanford university campus using deep learning, 2022a. URL `https://arxiv.org/abs/2203.05932`.

Fantine Huot, Ariel Lellouch, Paige Given, Bin Luo, Robert G. Clapp, Tamas Nemeth, Kurt T. Nihei, and Biondo L. Biondi. Detection and characterization of microseismic events from fiber-optic das data using deep learning, 2022b. URL `https://arxiv.org/abs/2203.07217`.

Stephan Husen, Edi Kissling, and Angela von Deschwanden. Induced seismicity during the construction of the gotthard base tunnel, switzerland: hypocenter locations and source dimensions. *Journal of Seismology*, 16(2):195–213, December 2011. doi:10.1007/s10950-011-9261-8. URL `https://doi.org/10.1007/s10950-011-9261-8`.

Maria-Teresa Hussels, Sebastian Chruscicki, Detlef Arndt, Swen Scheider, Jens Prager, Tobias Homann, and Abdel Karim Habib. Localization of transient events threatening pipeline integrity by fiber-optic distributed acoustic sensing. *Sensors*, 19(15):3322, July 2019. doi:10.3390/s19153322. URL https://doi.org/10.3390/s19153322.

B. Huttner, J. Reecht, N. Gisin, R. Passy, and J.P. Von der Weid. Local birefringence measurements in single-mode fibers with coherent optical frequency-domain reflectometry. *IEEE Photonics Technology Letters*, 10(10):1458–1460, October 1998. doi:10.1109/68.720293. URL https://doi.org/10.1109/68.720293.

M. Ichikawa, M. Kato, S. Uchida, K. Tamura, A. Kato, Y. Ito, and M.D. Groot. Low frequency das data study with integrated data analysis for monitoring hydraulic fracture. In *82nd EAGE Annual Conference & Exhibition*. European Association of Geoscientists & Engineers, 2021. doi:10.3997/2214-4609.202011176. URL https://doi.org/10.3997/2214-4609.202011176.

IEA. Direct Air Captures, 2021. URL https://www.iea.org/reports/direct-air-capture.

Roman Isaenkov, Roman Pevzner, Stanislav Glubokovskikh, Sinem Yavuz, Alexey Yurikov, Konstantin Tertyshnikov, Boris Gurevich, Julia Correa, Todd Wood, Barry Freifeld, Michael Mondanos, Stoyan Nikolov, and Paul Barraclough. An automated system for continuous monitoring of CO2 geosequestration using multi-well offset VSP with permanent seismic sources and receivers: Stage 3 of the CO2crc otway project. *International Journal of Greenhouse Gas Control*, 108:103317, June 2021. doi:10.1016/j.ijggc.2021.103317. URL https://doi.org/10.1016/j.ijggc.2021.103317.

Ailin Jia and Lihua Cheng. The technique of digital detailed reservoir characterization. *Petroleum Exploration and Development*, 37(6):709–715, December 2010. doi:10.1016/s1876-3804(11)60005-0. URL https://doi.org/10.1016/s1876-3804(11)60005-0.

Ailin Jia, Dongbo He, and Chengye Ji. Advances and challenges of reservoir characterization: A review of the current state-of-the-art. In *Earth Sciences*. InTech, February 2012. doi:10.5772/26404. URL https://doi.org/10.5772/26404.

Ge Jin, Kevin Mendoza, Baishali Roy, and Darryl G. Buswell. Machine learning-based fracture-hit detection algorithm using LFDAS signal. *The Leading Edge*, 38 (7):520–524, July 2019. doi:10.1190/tle38070520.1. URL https://doi.org/10.1190/tle38070520.1.

M. L. Jost and R. B. Herrmann. A student's guide to and review of moment tensors. *Seismological Research Letters*, 60(2):37–57, April 1989. doi:10.1785/gssrl.60.2.37. URL https://doi.org/10.1785/2Fgssrl.60.2.37.

B. I. Justusson. Median filtering: Statistical properties. In *Topics in Applied Physics*, pages 161–196. Springer-Verlag, 1981. doi:10.1007/bfb0057597. URL https://doi.org/10.1007/bfb0057597.

Hiroo Kanamori and John J. Cipar. Focal process of the great chilean earthquake may 22, 1960. *Physics of the Earth and Planetary Interiors*, 9(2):128–136, January 1974. doi:10.1016/0031-9201(74)90029-6. URL https://doi.org/10.1016/2F0031-9201/2874/2990029-6.

Martin Karrenbach, Dan Kahn, Steve Cole, Andrew Ridge, Kevin Boone, Jamie Rich, Ken Silver, and David Langton. Hydraulic-fracturing-induced strain and microseismic using in situ distributed fiber-optic sensing. *The Leading Edge*, 36 (10):837–844, October 2017. doi:10.1190/tle36100837.1. URL https://doi.org/10.1190/tle36100837.1.

Martin Karrenbach, Steve Cole, Andrew Ridge, Kevin Boone, Dan Kahn, Jamie Rich, Ken Silver, and David Langton. Fiber-optic distributed acoustic sensing of microseismicity, strain and temperature during hydraulic fracturing. *GEOPHYSICS*, 84(1):D11–D23, January 2019. doi:10.1190/geo2017-0396.1. URL https://doi.org/10.1190/2Fgeo2017-0396.1.

Peter Kelemen, Sally M. Benson, Hélène Pilorgé, Peter Psarras, and Jennifer Wilcox. An overview of the status and challenges of CO2 storage in minerals and geological formations. *Frontiers in Climate*, 1, November 2019. doi:10.3389/fclim.2019.00009. URL https://doi.org/10.3389/fclim.2019.00009.

Masayuki Kikuchi and Hiroo Kanamori. Inversion of complex body waves—III. *Bulletin of the Seismological Society of America*, 81(6):2335–2350, December 1991. doi:10.1785/bssa0810062335. URL https://doi.org/10.1785/2Fbssa0810062335.

Jeremiah Kimbell. *History and analysis of distributed acoustic sensing (DAS) for oilfield applications*. PhD thesis, Texas A&M University, 2013. URL https://hdl.handle.net/1969.1/150995.

Diederik P Kingma and Jimmy Ba. Adam: A method for stochastic optimization. *arXiv preprint arXiv:1412.6980*, 2014. doi:10.48550/arXiv.1412.6980. URL https://doi.org/10.48550/arXiv.1412.6980.

Kinzo Kishida, Artur Guzik, Ken'ichi Nishiguchi, Che-Hsien Li, Daiji Azuma, Qingwen Liu, and Zuyuan He. Development of real-time time gated digital (TGD) OFDR method and its performance verification. *Sensors*, 21(14):4865, July 2021. doi:10.3390/s21144865. URL https://doi.org/10.3390/s21144865.

Christian D. Klose. Geomechanical modeling of the nucleation process of australia's 1989 m5.6 newcastle earthquake. *Earth and Planetary Science Letters*, 256(3-4): 547–553, April 2007. doi:10.1016/j.epsl.2007.02.009. URL https://doi.org/10.1016/j.epsl.2007.02.009.

Christian D. Klose. Mechanical and statistical evidence of the causality of human-made mass shifts on the earth's upper crust and the occurrence of earthquakes. *Journal of Seismology*, 17(1):109–135, September 2012. doi:10.1007/s10950-012-9321-8. URL https://doi.org/10.1007/s10950-012-9321-8.

Stefan Kowarik, Maria-Teresa Hussels, Sebastian Chruscicki, Sven Münzenberger, Andy Lämmerhirt, Patrick Pohl, and Max Schubert. Fiber optic train monitoring with distributed acoustic sensing: Conventional and neural network data analysis. *Sensors*, 20(2):450, January 2020. doi:10.3390/s20020450. URL https://doi.org/10.3390/s20020450.

Alex Krizhevsky, Ilya Sutskever, and Geoffrey E. Hinton. Imagenet classification with deep convolutional neural networks. *Commun. ACM*, 60(6):84–90, may 2017. ISSN 0001-0782. doi:10.1145/3065386. URL https://doi.org/10.1145/3065386.

B.N. Kuvshinov. Interaction of helically wound fibre-optic cables with plane seismic waves. *Geophysical Prospecting*, 64(3):671–688, September 2015. doi:10.1111/1365-2478.12303. URL https://doi.org/10.1111%2F1365-2478.12303.

H. Serdar Kuyuk and Ohno Susumu. Real-time classification of earthquake using deep learning. *Procedia Computer Science*, 140:298–305, 2018. doi:10.1016/j.procs.2018.10.316. URL https://doi.org/10.1016/j.procs.2018.10.316.

O.L. Kuznetsov, E.M. Simkin, G.V. Chilingar, M.V. Gorfunkel, and J.O. Robertson Jr. Seismic techniques of enhanced oil recovery: Experimental and field results. *Energy Sources*, 24(9):877–889, September 2002. doi:10.1080/00908310290086761. URL https://doi.org/10.1080/00908310290086761.

Thorne Lay and Terry C Wallace. *Modern global seismology*. Elsevier, 1995.

Yann LeCun, Yoshua Bengio, and Geoffrey Hinton. Deep learning. *Nature*, 521(7553):436–444, May 2015. doi:10.1038/nature14539. URL https://doi.org/10.1038/nature14539.

Edward CW Lee, Johannes F de Boer, Mircea Mujat, Hyungsik Lim, and Seok H Yun. In vivo optical frequency domain imaging of human retina and choroid. *Optics Express*, 14(10):4403–4411, 2006.

Ariel Lellouch, Nathaniel J. Lindsey, William L. Ellsworth, and Biondo L. Biondi. Comparison between distributed acoustic sensing and geophones: Downhole microseismic monitoring of the FORGE geothermal experiment. *Seismological Research Letters*, 91(6):3256–3268, August 2020. doi:10.1785/0220200149. URL https://doi.org/10.1785/2F0220200149.

Ariel Lellouch, Bin Luo, Fantine Huot, Robert G. Clapp, Paige Given, Ettore Biondi, Tamas Nemeth, Kurt T. Nihei, and Biondo L. Biondi. Microseismic analysis over a single horizontal distributed acoustic sensing fiber using guided waves. *GEOPHYSICS*, 87(3):KS83–KS95, March 2022. doi:10.1190/geo2021-0418.1. URL https://doi.org/10.1190/geo2021-0418.1.

Alexander Lemieux, Alexi Shkarupin, and Karen Sharp. Geologic feasibility of underground hydrogen storage in canada. *International Journal of Hydrogen Energy*, 45(56):32243–32259, November 2020. doi:10.1016/j.ijhydene.2020.08.244. URL https://doi.org/10.1016/j.ijhydene.2020.08.244.

Lei Li, Jingqiang Tan, Yuyang Tan, Xinpeng Pan, and Zhengguang Zhao. Microseismic analysis to aid gas reservoir characterization. In *Sustainable Geoscience for Natural Gas Subsurface Systems*, pages 219–242. Elsevier, 2022a. doi:10.1016/b978-0-323-85465-8.00005-4. URL https://doi.org/10.1016/b978-0-323-85465-8.00005-4.

QI LI. Microseismic based reservoir characterization (sbrc): Stimulated reservoir volume, diffusivity, geomechanics and probabilistic modeling, 2018. URL https://prism.ucalgary.ca/handle/1880/106596.

T. Li, M.F. Cai, and M. Cai. A review of mining-induced seismicity in china. *International Journal of Rock Mechanics and Mining Sciences*, 44(8):1149–1171, December 2007. doi:10.1016/j.ijrmms.2007.06.002. URL https://doi.org/10.1016/j.ijrmms.2007.06.002.

Yingping Li, Martin Karrenbach, and Jonathan Ajo-Franklin. *Distributed acoustic sensing in geophysics: Methods and applications*, volume 268. John Wiley & Sons, 2022b.

Zhenhua Li and Mirko van der Baan. Microseismic event localization by acoustic time reversal extrapolation. *GEOPHYSICS*, 81(3):KS123–KS134, May 2016. doi:10.1190/geo2015-0300.1. URL https://doi.org/10.1190/geo2015-0300.1.

Sascha Liehr, Sven Münzenberger, and Katerina Krebber. Wavelength-scanning distributed acoustic sensing for structural monitoring and seismic applications. In *7th International Symposium on Sensor Science*. MDPI, July 2019. doi:10.3390/proceedings2019015030. URL https://doi.org/10.3390/proceedings2019015030.

Sophak Lim, Marie-Pierre Ledru, Francisco Valdez, Benoît Devillers, Alfred Houngnon, Charly Favier, and Laurent Bremond. Ecological effects of natural hazards and human activities on the ecuadorian pacific coast during the late holocene. *Palaeogeography, Palaeoclimatology, Palaeoecology*, 415:197–209, 2014.

Johanna Lippmann-Pipke, Jörg Erzinger, Martin Zimmer, Christian Kujawa, Margaret Boettcher, Esta Van Heerden, Armand Bester, Hannes Moller, Nicole A. Stroncik, and Zeev Reches. Geogas transport in fractured hard rock – correlations with mining seismicity at 3.54km depth, TauTona gold mine, south africa. *Applied Geochemistry*, 26(12):2134–2146, December 2011. doi:10.1016/j.apgeochem.2011.07.011. URL https://doi.org/10.1016/j.apgeochem.2011.07.011.

Qingwen Liu, Xinyu Fan, and Zuyuan He. Time-gated digital optical frequency domain reflectometry with 16-m spatial resolution over entire 110-km range. *Optics Express*, 23(20):25988, September 2015. doi:10.1364/oe.23.025988. URL `https://doi.org/10.1364/oe.23.025988`.

Yongzan Liu, Kan Wu, Ge Jin, George Moridis, Erich Kerr, Reid Scofield, and Andrew Johnson. Fracture-hit detection using LF-DAS signals measured during multifracture propagation in unconventional reservoirs. *SPE Reservoir Evaluation & Engineering*, 24(03):523–535, December 2020. doi:10.2118/204457-pa. URL `https://doi.org/10.2118/204457-pa`.

Zhu Liu, Zhu Deng, Gang He, Hailin Wang, Xian Zhang, Jiang Lin, Ye Qi, and Xi Liang. Challenges and opportunities for carbon neutrality in china. *Nature Reviews Earth & Environment*, 3(2):141–155, December 2021. doi:10.1038/s43017-021-00244-x. URL `https://doi.org/10.1038/s43017-021-00244-x`.

Gonzalo M. Cerón López. Modelamiento geoestadístico aplicado a la caracterización de yacimientos: modelo basado en celdas de alta resolución. *Enfoque UTE*, 8(4): 41–52, September 2017. doi:10.29019/enfoqueute.v8n4.174. URL `https://doi.org/10.29019/enfoqueute.v8n4.174`.

F. Jerry Lucia, Charles Kerans, and James W. Jennings. Carbonate reservoir characterization. *Journal of Petroleum Technology*, 55(06):70–72, June 2003. doi:10.2118/82071-jpt. URL `https://doi.org/10.2118/82071-jpt`.

Y. Z. Ma. Petrophysical data analytics for reservoir characterization. In *Quantitative Geosciences: Data Analytics, Geostatistics, Reservoir Characterization and Modeling*, pages 201–230. Springer International Publishing, 2019. doi:10.1007/978-3-030-17860-4_9. URL `https://doi.org/10.1007/978-3-030-17860-4_9`.

Taylor Martin and Greg Nash. Utah forge: High-resolution das microseismic data from well 78-32. Technical report, USDOE Geothermal Data Repository (United States); Energy and Geoscience Institute at the university of Utah, 2019.

Albena Mateeva, Jorge Lopez, Jeff Mestayer, Peter Wills, Barbara Cox, Denis Kiyashchenko, Zhaohui Yang, Wilfred Berlang, Rocky Detomo, and Samantha Grandi. Distributed acoustic sensing for reservoir monitoring with VSP. *The Leading Edge*, 32(10):1278–1283, October 2013. doi:10.1190/tle32101278.1. URL `https://doi.org/10.1190%2Ftle32101278.1`.

Albena Mateeva, Jorge Lopez, Hans Potters, Jeff Mestayer, Barbara Cox, Denis Kiyashchenko, Peter Wills, Samantha Grandi, Kees Hornman, Boris Kuvshinov, Wilfred Berlang, Zhaohui Yang, and Rocco Detomo. Distributed acoustic sensing for reservoir monitoring with vertical seismic profiling. *Geophysical Prospecting*, 62(4):679–692, May 2014. doi:10.1111/1365-2478.12116. URL `https://doi.org/10.1111/1365-2478.12116`.

S. C. Maxwell, J. Du, J. Shemeta, U. Zimmer, N. Boroumand, and L. G. Griffin. Monitoring SAGD steam injection using microseismicity and tiltmeters. *SPE Reservoir Evaluation & Engineering*, 12(02):311–317, April 2009. doi:10.2118/110634-pa. URL `https://doi.org/10.2118/110634-pa`.

S. C. Maxwell, J. Rutledge, R. Jones, and M. Fehler. Petroleum reservoir characterization using downhole microseismic monitoring. *GEOPHYSICS*, 75(5):75A129–75A137, September 2010. doi:10.1190/1.3477966. URL `https://doi.org/10.1190/1.3477966`.

Shawn Maxwell. *Microseismic Imaging of Hydraulic Fracturing*. Society of Exploration Geophysicists, January 2014. doi:10.1190/1.9781560803164. URL `https://doi.org/10.1190/1.9781560803164`.

Shawn C. Maxwell and Theodore I. Urbancic. The role of passive microseismic monitoring in the instrumented oil field. *The Leading Edge*, 20(6):636–639, June 2001. doi:10.1190/1.1439012. URL `https://doi.org/10.1190/1.1439012`.

A. McGarr. Maximum magnitude earthquakes induced by fluid injection. *Journal of Geophysical Research: Solid Earth*, 119(2):1008–1019, February 2014. doi:10.1002/2013jb010597. URL `https://doi.org/10.1002/2013jb010597`.

J. Mestayer, B. Cox, P. Wills, D. Kiyashchenko, J. Lopez, M. Costello, S. Bourne, G. Ugueto, R. Lupton, G. Solano, D. Hill, and A. Lewis. Field trials of distributed acoustic sensing for geophysical monitoring. In *SEG Technical Program Expanded Abstracts 2011*. Society of Exploration Geophysicists, January 2011. doi:10.1190/1.3628095. URL `https://doi.org/10.1190/1.3628095`.

A. Midilli, M. Ay, I. Dincer, and M.A. Rosen. On hydrogen and hydrogen energy strategies. *Renewable and Sustainable Energy Reviews*, 9(3):255–271, June 2005. doi:10.1016/j.rser.2004.05.003. URL `https://doi.org/10.1016/j.rser.2004.05.003`.

M.M.. M. Molenaar, D.J.. J. Hill, P.. Webster, E.. Fidan, and B.. Birch. First downhole application of distributed acoustic sensing for hydraulic-fracturing monitoring and diagnostics. *SPE Drilling & Completion*, 27(01):32–38, February 2012. doi:10.2118/140561-pa. URL `https://doi.org/10.2118/140561-pa`.

Daniele Molteni, Michael John Williams, and Colin Wilson. Detecting microseismicity using distributed vibration. *First Break*, 35(4), April 2017. doi:10.3997/1365-2397.35.4.87841. URL `https://doi.org/10.3997/1365-2397.35.4.87841`.

Michael Mondanos and Thomas Coleman. Application of distributed fibre-optic sensing to geothermal reservoir characterization and monitoring. *First Break*, 37 (7):51–56, July 2019. doi:10.3997/1365-2397.n0040. URL `https://doi.org/10.3997/2F1365-2397.n0040`.

Joseph Moore, Stuart Simmons, John McLennan, Clay Jones, Gosia Skowron, Phil Wannamaker, Greg Nash, Christian Hardwick, Will Hurlbut, Rick Allis, et al.

Utah forge: Phase 2c topical report. Technical report, DOE Geothermal Data Repository; Energy and Geoscience Institute at the university of Utah, 2019.

S. Mostafa Mousavi, William L. Ellsworth, Weiqiang Zhu, Lindsay Y. Chuang, and Gregory C. Beroza. Earthquake transformer—an attentive deep-learning model for simultaneous earthquake detection and phase picking. *Nature Communications*, 11(1), August 2020. doi:10.1038/s41467-020-17591-w. URL https://doi.org/10.1038/s41467-020-17591-w.

Nasiru Salahu Muhammed, Bashirul Haq, Dhafer Al Shehri, Amir Al-Ahmed, Mohammed Mizanur Rahman, and Ehsan Zaman. A review on underground hydrogen storage: Insight into geological sites, influencing factors and future outlook. *Energy Reports*, 8:461–499, November 2022. doi:10.1016/j.egyr.2021.12.002. URL https://doi.org/10.1016/j.egyr.2021.12.002.

G. Naldrett, , C. Cerrahoglu, and V. Mahue. Production monitoring using next-generation distributed sensing systems. *Petrophysics – The SPWLA Journal of Formation Evaluation and Reservoir Description*, 59(4):496–510, August 2018. doi:10.30632/pjv59v4-2018a5. URL https://doi.org/10.30632/pjv59v4-2018a5.

Craig Nicholson and Robert L. Wesson. Triggered earthquakes and deep well activities. *Pure and Applied Geophysics PAGEOPH*, 139(3-4):561–578, 1992. doi:10.1007/bf00879951. URL https://doi.org/10.1007/bf00879951.

Ahmed I. Osman, Neha Mehta, Ahmed M. Elgarahy, Mahmoud Hefny, Amer Al-Hinai, Ala'a H. Al-Muhtaseb, and David W. Rooney. Hydrogen production, storage, utilisation and environmental impacts: a review. *Environmental Chemistry Letters*, 20(1):153–188, October 2021. doi:10.1007/s10311-021-01322-8. URL https://doi.org/10.1007/s10311-021-01322-8.

Volker Oye and Michael Roth. Automated seismic event location for hydrocarbon reservoirs. *Computers & Geosciences*, 29(7):851–863, August 2003. doi:10.1016/s0098-3004(03)00088-8. URL https://doi.org/10.1016/s0098-3004(03)00088-8.

Volker Oye, Eyvind Aker, Thomas M. Daley, Daniela Kühn, Bahman Bohloli, and Valeri Korneev. Microseismic monitoring and interpretation of injection data from the in salah CO2 storage site (krechba), algeria. *Energy Procedia*, 37:4191–4198, 2013. doi:10.1016/j.egypro.2013.06.321. URL https://doi.org/10.1016/j.egypro.2013.06.321.

Ahmet Ozarslan. Large-scale hydrogen energy storage in salt caverns. *International Journal of Hydrogen Energy*, 37(19):14265–14277, October 2012. doi:10.1016/j.ijhydene.2012.07.111. URL https://doi.org/10.1016/j.ijhydene.2012.07.111.

Yi Pan, Dong Hui, Pingya Luo, Yan Zhang, Lei Sun, and Ke Wang. Experimental investigation of the geochemical interactions between supercritical CO2 and shale:

Implications for CO2 storage in gas-bearing shale formations. *Energy & Fuels*, 32 (2):1963–1978, January 2018. doi:10.1021/acs.energyfuels.7b03074. URL https://doi.org/10.1021/acs.energyfuels.7b03074.

Kristine Pankow, Maria Mesimeri, John McLennan, Phil Wannamaker, and Joe Moore. Seismic monitoring at the utah frontier observatory for research in geothermal energy. In *Proceedings of the 45th Workshop on Geothermal Reservoir Engineering*, 2020.

Tom Parker, Sergey Shatalin, and Mahmoud Farhadiroushan. Distributed acoustic sensing – a new tool for seismic applications. *First Break*, 32(2), February 2014. doi:10.3997/1365-2397.2013034. URL https://doi.org/10.3997%2F1365-2397.2013034.

Julie K. Pearce, Syed S. Raza, Kim A. Baublys, Phil J. Hayes, Mahshid Firouzi, and Victor Rudolph. Unconventional CO_2 storage. In *Proceedings of the 2021 Asia Pacific Unconventional Resources Technology Conference*. Unconventional Resources Technology Conference, 2021. doi:10.15530/ap-urtec-2021-208295. URL https://doi.org/10.15530/ap-urtec-2021-208295.

Zhaoqiang Peng, Jianan Jian, Mohan Wang, Qirui Wang, Thomas Boyer, Hongqiao Wen, Hu Liu, Zhi-Hong Mao, and Kevin P. Chen. Big data analytics on fiber-optical distributed acoustic sensing with rayleigh enhancements. In *2019 IEEE Photonics Conference (IPC)*. IEEE, September 2019a. doi:10.1109/ipcon.2019.8908496. URL https://doi.org/10.1109/ipcon.2019.8908496.

Zhaoqiang Peng, Jianan Jian, HongQiao Wen, Mohan Wang, Hu Liu, Desheng Jiang, Zhihong Mao, and Kevin P Chen. Fiber-optical distributed acoustic sensing signal enhancements using ultrafast laser and artificial intelligence for human movement detection and pipeline monitoring. In *Optical Data Science II*, volume 10937, page 109370J. International Society for Optics and Photonics, 2019b.

Shan Qu, Zhe Guan, Eric Verschuur, and Yangkang Chen. Automatic high-resolution microseismic event detection via supervised machine learning. *Geophysical Journal International*, 222(3):1881–1895, June 2020. doi:10.1093/gji/ggaa193. URL https://doi.org/10.1093/gji/ggaa193.

J. W. B. Rae, A. Burke, L. F. Robinson, J. F. Adkins, T. Chen, C. Cole, R. Greenop, T. Li, E. F. M. Littley, D. C. Nita, J. A. Stewart, and B. J. Taylor. CO2 storage and release in the deep southern ocean on millennial to centennial timescales. *Nature*, 562(7728):569–573, October 2018. doi:10.1038/s41586-018-0614-0. URL https://doi.org/10.1038/s41586-018-0614-0.

Mohammed Wahab Raheem et al. Prediction by reservoir porosity using microseismic attribute analysis by machine learning algorithms in an iraqi oil field. *Turkish Journal of Computer and Mathematics Education (TURCOMAT)*, 12(14): 3324–3332, 2021.

Thomas Reinsch, Jan Henninges, Julia Götz, Philippe Jousset, David Bruhn, and Stefan Lüth. Distributed acoustic sensing technology for seismic exploration in magmatic geothermal areas. In *World Geothermal Congress 2015*, 2015.

Ali Rezaei, Fred Aminzadeh, and Eric VonLunen. Applications of machine learning for estimating the stimulated reservoir volume (SRV). In *Proceedings of the 9th Unconventional Resources Technology Conference*. American Association of Petroleum Geologists, 2021. doi:10.15530/urtec-2021-5537. URL https://doi.org/10.15530/urtec-2021-5537.

Ryan H Ricker and Klauder Ormsby. Butterworth–a choice of wavelets. *CSEG Recorder*, 19(7):8–9, 1994.

P. S. Ringrose and T. A. Meckel. Maturing global CO2 storage resources on offshore continental margins to achieve 2ds emissions reductions. *Scientific Reports*, 9(1), November 2019. doi:10.1038/s41598-019-54363-z. URL https://doi.org/10.1038/s41598-019-54363-z.

Arcangelo Sena, Gabino Castillo, Kevin Chesser, Simon Voisey, Jorge Estrada, Juan Carcuz, Emilio Carmona, and Peggy Hodgkins. Seismic reservoir characterization in resource shale plays: Stress analysis and sweet spot discrimination. *The Leading Edge*, 30(7):758–764, July 2011. doi:10.1190/1.3609090. URL https://doi.org/10.1190/1.3609090.

Ahmed Shaheen, Umair bin Waheed, Michael Fehler, Lubos Sokol, and Sherif Hanafy. GroningenNet: Deep learning for low-magnitude earthquake detection on a multi-level sensor network. *Sensors*, 21(23):8080, December 2021. doi:10.3390/s21238080. URL https://doi.org/10.3390/s21238080.

Essam F. Sharaf and Hussain Sheikha. Reservoir characterization and production history matching of lower cretaceous, muddy formation in ranch creek area, bell creek oil field, southeastern montana, USA. *Marine and Petroleum Geology*, 127:104996, May 2021. doi:10.1016/j.marpetgeo.2021.104996. URL https://doi.org/10.1016/j.marpetgeo.2021.104996.

Rohit Shaw and Soumyajit Mukherjee. The development of carbon capture and storage (CCS) in india: A critical review. *Carbon Capture Science & Technology*, 2:100036, March 2022. doi:10.1016/j.ccst.2022.100036. URL https://doi.org/10.1016/j.ccst.2022.100036.

Anton Shchipanov, Lars Kollbotn, Mauro Encinas, Ingebret Fjelde, and Roman Berenblyum. Periodic CO2 injection for improved storage capacity and pressure management under intermittent CO2 supply. *Energies*, 15(2):566, January 2022. doi:10.3390/en15020566. URL https://doi.org/10.3390/en15020566.

Lihi Shiloh, Avishay Eyal, and Raja Giryes. Efficient processing of distributed acoustic sensing data using a deep learning approach. *Journal of Lightwave Technology*, 37(18):4755–4762, 2019.

Masanao Shinohara, Tomoaki Yamada, Takeshi Akuhara, Kimihiro Mochizuki, and Shin'ichi Sakai. Performance of seismic observation by distributed acoustic sensing technology using a seafloor cable off sanriku, japan. *Frontiers in Marine Science*, 9, April 2022. doi:10.3389/fmars.2022.844506. URL `https://doi.org/10.3389/fmars.2022.844506`.

Parisa Shokouhi, Vikas Kumar, Sumedha Prathipati, Seyyed A. Hosseini, Clyde Lee Giles, and Daniel Kifer. Physics-informed deep learning for prediction of CO2 storage site response. *Journal of Contaminant Hydrology*, 241:103835, August 2021. doi:10.1016/j.jconhyd.2021.103835. URL `https://doi.org/10.1016/j.jconhyd.2021.103835`.

Valeriya Shulakova, Konstantin Tertyshnikov, Roman Pevzner, Yevhen Kovalyshen, and Boris Gurevich. Ambient seismic noise in an urban environment: case study using downhole distributed acoustic sensors at the curtin university campus in perth, western australia. *Exploration Geophysics*, pages 1–14, January 2022. doi:10.1080/08123985.2021.2021802. URL `https://doi.org/10.1080%2F08123985.2021.2021802`.

Ma Shutian and David W. Eaton. Anatomy of a small earthquake swarm in southern ontario, canada. *Seismological Research Letters*, 80(2):214–223, March 2009. doi:10.1785/gssrl.80.2.214. URL `https://doi.org/10.1785/2Fgssrl.80.2.214`.

Trine Simmenes, Olav R. Hansen, Ola Eiken, Gunn Mari Grimsmo Teige, Christian Hermanrud, Stian Johansen, Hege Marit Nordgaard Bolaas, and Hilde Hansen. Importance of pressure management in CO2 storage. In *All Days*. OTC, May 2013. doi:10.4043/23961-ms. URL `https://doi.org/10.4043/23961-ms`.

J. Simon, A.M. Ferriz, and L.C. Correas. HyUnder – hydrogen underground storage at large scale: Case study spain. *Energy Procedia*, 73:136–144, June 2015. doi:10.1016/j.egypro.2015.07.661. URL `https://doi.org/10.1016/j.egypro.2015.07.661`.

David W Simpson and William Leith. The 1976 and 1984 gazli, ussr, earthquakes—were they induced? *Bulletin of the Seismological Society of America*, 75(5):1465–1468, 1985.

Harpreet Singh. Hydrogen storage in inactive horizontal shale gas wells: Techno-economic analysis for haynesville shale. *Applied Energy*, 313:118862, May 2022. doi:10.1016/j.apenergy.2022.118862. URL `https://doi.org/10.1016/j.apenergy.2022.118862`.

Michael Berry Smith and Carl Montgomery. *Hydraulic fracturing*. Crc Press, 2015.

Pavol Stajanca, Sebastian Chruscicki, Tobias Homann, Stefan Seifert, Dirk Schmidt, and Abdelkarim Habib. Detection of leak-induced pipeline vibrations using fiber—optic distributed acoustic sensing. *Sensors*, 18(9):2841, August 2018. doi:10.3390/s18092841. URL `https://doi.org/10.3390/s18092841`.

Seth Stein and Michael Wysession. *An introduction to seismology, earthquakes, and earth structure*. John Wiley & Sons, 2009.

Jenny Suckale. Induced seismicity in hydrocarbon fields. In *Advances in Geophysics*, pages 55–106. Elsevier, 2009. doi:10.1016/s0065-2687(09)05107-3. URL https://doi.org/10.1016/s0065-2687(09)05107-3.

Yixiang Sun, Hao Li, Cunzheng Fan, Baoqiang Yan, Junfeng Chen, Zhijun Yan, and Qizhen Sun. Review of a specialty fiber for distributed acoustic sensing technology. *Photonics*, 9(5):277, April 2022. doi:10.3390/photonics9050277. URL https://doi.org/10.3390/photonics9050277.

Christian Szegedy, Sergey Ioffe, Vincent Vanhoucke, and Alex Alemi. Inception-v4, inception-resnet and the impact of residual connections on learning, 2016. URL https://arxiv.org/abs/1602.07261.

J. J. Taber, F. D. Martin, and R. S. Seright. EOR screening criteria revisited—part 1: Introduction to screening criteria and enhanced recovery field projects. *SPE Reservoir Engineering*, 12(03):189–198, August 1997. doi:10.2118/35385-pa. URL https://doi.org/10.2118/35385-pa.

Rui Tanaka, Makoto Naoi, Youqing Chen, Kazune Yamamoto, Keiichi Imakita, Naofumi Tsutsumi, Akihiro Shimoda, Daiki Hiramatsu, Hironori Kawakata, Tsuyoshi Ishida, Eiichi Fukuyama, Hiroyuki Tanaka, Yutaro Arima, Shigehiro Kitamura, and Daisuke Hyodo. Preparatory acoustic emission activity of hydraulic fracture in granite with various viscous fluids revealed by deep learning technique. *Geophysical Journal International*, 226(1):493–510, March 2021. doi:10.1093/gji/ggab096. URL https://doi.org/10.1093/gji/ggab096.

Radoslaw Tarkowski. Underground hydrogen storage: Characteristics and prospects. *Renewable and Sustainable Energy Reviews*, 105:86–94, May 2019. doi:10.1016/j.rser.2019.01.051. URL https://doi.org/10.1016/j.rser.2019.01.051.

Javier Tejedor, Javier Macias-Guarasa, Hugo Martins, Juan Pastor-Graells, Pedro Corredera, and Sonia Martin-Lopez. Machine learning methods for pipeline surveillance systems based on distributed acoustic sensing: A review. *Applied Sciences*, 7(8):841, August 2017. doi:10.3390/app7080841. URL https://doi.org/10.3390/app7080841.

Javier Tejedor, Javier Macias-Guarasa, Hugo F. Martins, Sonia Martin-Lopez, and Miguel Gonzalez-Herraez. A multi-position approach in a smart fiber-optic surveillance system for pipeline integrity threat detection. *Electronics*, 10(6):712, March 2021. doi:10.3390/electronics10060712. URL https://doi.org/10.3390/electronics10060712.

Leon Thomsen. Weak elastic anisotropy. *GEOPHYSICS*, 51(10):1954–1966, October 1986. doi:10.1190/1.1442051. URL https://doi.org/10.1190/1.1442051.

Rainer Tonn. Neural network seismic reservoir characterization in a heavy oil reservoir. *The Leading Edge*, 21(3):309–312, March 2002. doi:10.1190/1.1463783. URL https://doi.org/10.1190/1.1463783.

Ilya Tsvankin. Anisotropic parameters and p-wave velocity for orthorhombic media. *GEOPHYSICS*, 62(4):1292–1309, July 1997. doi:10.1190/1.1444231. URL https://doi.org/10.1190/1.1444231.

J. Ullo. Recent developments in seismic exploration and reservoir characterization. In *1997 IEEE Ultrasonics Symposium Proceedings. An International Symposium (Cat. No.97CH36118)*. IEEE, 1997. doi:10.1109/ultsym.1997.663133. URL https://doi.org/10.1109/ultsym.1997.663133.

Juun van der Horst, Hans den Boer, Peter in 't Panhuis, Roel Kusters, Dayeeta Roy, Andrew Ridge, and Alastair Godfrey. Fibre optic sensing for improved wellbore surveillance. In *All Days*. IPTC, March 2013. doi:10.2523/iptc-16873-ms. URL https://doi.org/10.2523/iptc-16873-ms.

Václav Vavryčuk. Focal mechanisms in anisotropic media. *Geophysical Journal International*, 161(2):334–346, May 2005. doi:10.1111/j.1365-246x.2005.02585.x. URL https://doi.org/10.1111/2Fj.1365-246x.2005.02585.x.

James P. Verdon, Steve A. Horne, Andrew Clarke, Anna L. Stork, Alan F. Baird, and J-Michael Kendall. Microseismic monitoring using a fibre-optic distributed acoustic sensor (DAS) array. *GEOPHYSICS*, pages 1–48, March 2020. doi:10.1190/geo2019-0752.1. URL https://doi.org/10.1190/geo2019-0752.1.

JP Von der Weid, R Passy, AO Forno, B Huttner, and N Gisin. Return loss measurements of wdm filters with tunable coherent optical frequency-domain reflectometry. *IEEE Photonics Technology Letters*, 9(11):1508–1510, 1997.

F. Walter, D. Gräff, F. Lindner, P. Paitz, M. Köpfli, M. Chmiel, and A. Fichtner. Distributed acoustic sensing of microseismic sources and wave propagation in glaciated terrain. *Nature Communications*, 11(1), May 2020. doi:10.1038/s41467-020-15824-6. URL https://doi.org/10.1038/s41467-020-15824-6.

Daniel Wamriew, Marwan Charara, and Evgenii Maltsev. Deep neural network for real-time location and moment tensor inversion of borehole microseismic events induced by hydraulic fracturing. In *Day 3 Wed, October 28, 2020*. SPE, October 2020. doi:10.2118/201925-ms. URL https://doi.org/10.2118/201925-ms.

Daniel Wamriew, Evgenii Maltsev, Roman Pevzner, and Dimitri Pissarenko. Deep neural networks for inversion of borehole microseismic data recorded by DAS. In *Sixth EAGE Borehole Geophysics Workshop*. European Association of Geoscientists & Engineers, 2021a. doi:10.3997/2214-4609.2021613016. URL https://doi.org/10.3997/2214-4609.2021613016.

Daniel Wamriew, Roman Pevzner, Evgenii Maltsev, and Dimitri Pissarenko. Deep neural networks for detection and location of microseismic events and velocity model inversion from microseismic data acquired by distributed acoustic sensing array. *Sensors*, 21(19):6627, October 2021b. doi:10.3390/s21196627. URL https://doi.org/10.3390/s21196627.

Daniel Wamriew, Marwan Charara, and Dimitri Pissarenko. Joint event location and velocity model update in real-time for downhole microseismic monitoring: A deep learning approach. *Computers & Geosciences*, 158:104965, January 2022a. doi:10.1016/j.cageo.2021.104965. URL https://doi.org/10.1016/j.cageo.2021.104965.

Daniel Wamriew, Desmond Batsa Dorhjie, Daniil Bogoedov, Roman Pevzner, Evgenii Maltsev, Marwan Charara, Dimitri Pissarenko, and Dmitry Koroteev. Microseismic monitoring and analysis using cutting-edge technology: A key enabler for reservoir characterization. *Remote Sensing*, 14(14):3417, July 2022b. doi:10.3390/rs14143417. URL https://doi.org/10.3390/2Frs14143417.

Shuai Wang, Xinyu Fan, Qingwen Liu, and Zuyuan He. Distributed fiber-optic vibration sensing based on phase extraction from time-gated digital OFDR. *Optics Express*, 23(26):33301, December 2015. doi:10.1364/oe.23.033301. URL https://doi.org/10.1364/oe.23.033301.

Yi Wang, Xueyi Shang, and Kang Peng. Locating mine microseismic events in a 3d velocity model through the gaussian beam reverse-time migration technique. *Sensors*, 20(9):2676, May 2020. doi:10.3390/s20092676. URL https://doi.org/10.3390/s20092676.

Yuan Wang, Pedro Tovar, Liang Chen, and Xiaoyi Bao. Generation of high performance optical chirped pulse for distributed strain sensing application with high strain accuracy and larger measurement range. *Optics Express*, 30(11):18518, May 2022. doi:10.1364/oe.454913. URL https://doi.org/10.1364/oe.454913.

Paul Webster, Mathieu Molenaar, and Colin Perkins. Das microseismic fiber-optic locating das microseismic events and errors. *CSEG Recorder*, 41(06):38–39, June 2016. URL https://csegrecorder.com/articles/view/das-microseismic/20.

Mark Wegmuller, Philippe Oberson, Jean-Pierre von der Weid, Olivier Guinnard, Laurent Guinnard, Claudio Vinegoni, Matthieu Legre, and Nicolas Gisin. Overview of coherent reflectometry techniques: Characterization of components and small systems. In *Tech. Digest Symposium on Optical Fiber Measurements SOFM 2000, NIST Publication*, volume 953, pages 155–160, 2000.

David Were, Frank Kansiime, Tadesse Fetahi, Ashley Cooper, and Charles Jjuuko. Carbon sequestration by wetlands: A critical review of enhancement measures for climate change mitigation. *Earth Systems and Environment*, 3(2):327–340, April 2019. doi:10.1007/s41748-019-00094-0. URL https://doi.org/10.1007/s41748-019-00094-0.

A. Williams, J. M. Kendall, A. Clarke, and J. Verdon. Challenges in locating microseismic events using distributed acoustic sensors. In *AGU Fall Meeting Abstracts*, volume 2017, pages S33B–0873, December 2017. URL https://ui.adsabs.harvard.edu/abs/2017AGUFM.S33B0873W.

Sherilyn Williams-Stroud, Robert Bauer, Hannes Leetaru, Volker Oye, Frantisek Stanek, Sallie Greenberg, and Nadege Langet. Analysis of microseismicity and reactivated fault size to assess the potential for felt events by CO_2 injection in the illinois basin. *Bulletin of the Seismological Society of America*, 110(5):2188–2204, August 2020. doi:10.1785/0120200112. URL https://doi.org/10.1785/0120200112.

Huijuan Wu, Chaoqun Wang, Xinyu Liu, DengKe Gan, Yimeng Liu, Yunjiang Rao, and Abdulafeez Olawale Olaribigbe. Intelligent target recognition for distributed acoustic sensors by using both manual and deep features. *Applied Optics*, 60(23): 6878, August 2021. doi:10.1364/ao.431791. URL https://doi.org/10.1364/ao.431791.

Tingting Yang, Yanbo Xiao, Zengling Ran, Xiu He, Tianqi Shao, Wenyu Wang, Kai Li, Dong Sun, Xiaojuan Qin, Zhengxi He, Yachao Zhang, and Dongsheng Ye. Design of a weak fiber bragg grating acoustic sensing system for pipeline leakage monitoring in a nuclear environment. *IEEE Sensors Journal*, 21(20):22703–22711, October 2021. doi:10.1109/jsen.2021.3098313. URL https://doi.org/10.1109/jsen.2021.3098313.

Sergey Yaskevich, Anton A. Duchkov, and Yuriy Ivanov. Approximate traveltime inversion in downhole microseismic monitoring. *Geophysical Prospecting*, 68(3): 918–925, December 2019. doi:10.1111/1365-2478.12906. URL https://doi.org/10.1111/1365-2478.12906.

V.A. Yatseev, A.M. Zotov, and O.V. Butov. Combined frequency and phase domain time-gated reflectometry based on a fiber with reflection points for absolute measurements. *Results in Physics*, 19:103485, December 2020. doi:10.1016/j.rinp.2020.103485. URL https://doi.org/10.1016/j.rinp.2020.103485.

Clara E. Yoon, Ossian O'Reilly, Karianne J. Bergen, and Gregory C. Beroza. Earthquake detection through computationally efficient similarity search. *Science Advances*, 1(11), December 2015. doi:10.1126/sciadv.1501057. URL https://doi.org/10.1126/sciadv.1501057.

Xinghe Yu, Y. Zee Ma, Ernest Gomez, David Psaila, Paul La Pointe, and Shengli Li. Reservoir characterization and modeling: A look back to see the way forward. In *Uncertainty Analysis and Reservoir Modeling: Developing and Managing Assets in an Uncertain World*. American Association of Petroleum Geologists, jan 2011. ISBN 9781629810102. doi:10.1306/13301421M963458. URL https://doi.org/10.1306/13301421M963458.

Hao Zhang and Kristine L. Pankow. High-resolution bayesian spatial autocorrelation (SPAC) quasi-3-d model of utah FORGE site with a dense geophone array. *Geophysical Journal International*, 225(3):1605–1615, February 2021. doi:10.1093/gji/ggab049. URL `https://doi.org/10.1093/2Fgji/2Fggab049`.

Yuxing Zhao, Yue Li, and Ning Wu. Distributed acoustic sensing vertical seismic profile data denoiser based on convolutional neural network. *IEEE Transactions on Geoscience and Remote Sensing*, pages 1–11, 2021. doi:10.1109/tgrs.2020.3042202. URL `https://doi.org/10.1109/tgrs.2020.3042202`.

Mark D. Zoback and Steven M. Gorelick. To prevent earthquake triggering, pressure changes due to CO_2 injection need to be limited. *Proceedings of the National Academy of Sciences*, 112(33), August 2015. doi:10.1073/pnas.1508533112. URL `https://doi.org/10.1073/pnas.1508533112`.

Eryk ŚSwiech and Paweł Wandycz. Differences between downhole and surface micro-seismic monitoring. *Mining Science; ISSN 2300-9586*, 2015. doi:10.5277/MSC152206. URL `http://www.miningscience.pwr.edu.pl/Differences-between-downhole-and-surface-micro-seismic-monitoring,60952,0,2.html`.